

Review

N-Doped Graphene (N-G)/MOF(ZIF-8)-Based/Derived Materials for Electrochemical Energy Applications: Synthesis, Characteristics, and Functionality

Niladri Talukder ¹, Yudong Wang ¹, Bharath Babu Nunna ^{2,3,4} and Eon Soo Lee ^{1,*}

¹ Advanced Energy Systems and Microdevices Laboratory, Department of Mechanical and Industrial Engineering, New Jersey Institute of Technology, Newark, NJ 07102, USA; nt22@njit.edu (N.T.); yw35@njit.edu (Y.W.)

² Department of Mechanical Engineering, Weber State University, Ogden, UT 84408, USA; bnunna@weber.edu

³ Division of Engineering in Medicine, Department of Medicine, Brigham and Women's Hospital, Harvard Medical School, Harvard University, Cambridge, MA 02139, USA

⁴ Harvard Graduate School of Education, Harvard University, Cambridge, MA 02138, USA

* Correspondence: eonsoo.lee@njit.edu; Tel.: +1-973-596-3318

Abstract: In recent years, graphene-type materials originating from metal–organic frameworks (MOFs) or integrated with MOFs have exhibited notable performances across various applications. However, a comprehensive understanding of these complex materials and their functionalities remains obscure. While some studies have reviewed graphene/MOF composites from different perspectives, due to their structural–functional intricacies, it is crucial to conduct more in-depth reviews focusing on specific sets of graphene/MOF composites designed for particular applications. In this review, we thoroughly investigate the syntheses, characteristics, and performances of N-G/MOF(ZIF-8)-based/derived materials employed in electrochemical energy conversion and storage systems. Special attention is given to realizing their fundamental functionalities. The discussions are divided into three segments based on the application of N-G/ZIF-8-based/derived materials as electrode materials for batteries, electrodes for electrochemical capacitors, and electrocatalysts. As electrodes for batteries, N-G/MOF(ZIF-8) materials can mitigate issues like an electrode volume expansion for Li-ion batteries and the ‘shuttle effect’ for Li-S batteries. As electrodes for electrochemical capacitors, these materials can considerably improve the ion transfer rate and electronic conductivity, thereby enhancing the specific capacitance while maintaining the structural stability. Also, it was observed that these materials could occasionally outperform standard platinum-based catalysts for the electrochemical oxygen reduction reaction (ORR). The reported electrochemical performances and structural parameters of these materials were carefully tabulated in uniform units and scales. Through a critical analysis of the present synthesis trends, characteristics, and functionalities of these materials, specific aspects were identified that required further exploration to fully utilize their inherent capabilities.

Keywords: N-doped graphene; zeolitic imidazolate framework-8 (ZIF-8); battery electrode; electrochemical capacitor electrode; electrochemical catalysts



Citation: Talukder, N.; Wang, Y.; Nunna, B.B.; Lee, E.S. N-Doped Graphene (N-G)/MOF(ZIF-8)-Based/Derived Materials for Electrochemical Energy Applications: Synthesis, Characteristics, and Functionality. *Batteries* **2024**, *10*, 47. <https://doi.org/10.3390/batteries10020047>

Academic Editors: A. Robert Armstrong and Yong-Joon Park

Received: 18 December 2023

Revised: 12 January 2024

Accepted: 24 January 2024

Published: 27 January 2024



Copyright: © 2024 by the authors. Licensee MDPI, Basel, Switzerland. This article is an open access article distributed under the terms and conditions of the Creative Commons Attribution (CC BY) license (<https://creativecommons.org/licenses/by/4.0/>).

1. Introduction

In recent years, there has been noteworthy research focusing on the exploration of low-dimensional carbon-based materials, driven by their potential applications in various industrial fields [1–10]. Specifically, graphene and its derivatives have attracted considerable interest for their applications in a range of electrochemical energy systems, including battery electrode materials, electrochemical capacitors, and fuel cell catalysts [11–17]. Among these materials, nitrogen-doped graphene (N-G) has been extensively studied for its promising functionality. In the research field of graphene functionalization by adatom

doping, although metallic dopants can promote greater electrochemical activities, they have the considerable drawbacks of facile degradation during operations. To subvert this issue, different non-metallic adatoms, such as boron (B), sulfur (S) and nitrogen (N) are often chosen for graphene functionalization [18]. Nonetheless, unlike B and S adatoms, the doped N atoms in graphene play the unique role of generating both p-type and n-type effects in different parts of the graphene at the same time by forming different types of bonds with the carbon atoms in the graphene's structure (e.g., pyridinic-N, graphitic-N, pyrrolic-N, and pyridinic-N-oxides, etc.), which renders N-doped graphene (N-G) as arguably one of the best options for developing graphene-based electrochemical materials. Moreover, through experimental, theoretical, and computational investigations, it has been demonstrated that the introduction of nitrogen atoms into the graphene structure generates electronically active sites, enabling the material to facilitate electrochemical activities [18–24]. Although the primary objective of N-G-based materials is to replace precious metal-based materials, like platinum group metals (PGMs), in electrochemical applications, significant improvements in various electrochemical parameters are still required at their current developmental stage to effectively utilize N-G materials in electrochemical energy systems.

In the effort to advance N-G-based materials, there has been an increasing focus on N-G composites derived from or integrated with metal–organic frameworks (MOFs) [25–30]. Within the large MOF-material family, the subclass of zeolitic imidazolate frameworks (ZIFs) has the most well-defined geometric chemical and crystal structures, which are crucial for the materials' functionality and operational stability [31,32]. Among different members of the ZIF subclass, ZIF-8 has been extensively studied over the past decade for its prominent structural features, including high porosity (pore volume ~ 1.088 mL/g), large surface area (1500–2500 m²/g), well-defined rhombic dodecahedron crystal unit, and sodalite crystal structure [30,33–35]. From the perspective of the properties of electrochemically active materials, with the above-mentioned features, ZIF-8 facilitates a higher rate of reactant transport for the electrochemical processes, hosts a significantly higher number of electrochemically active sites, and helps maintain the structural stability of its composites throughout the electrochemical operations. All these aspects attracted an interest in ZIF-8 as one of the high-potential materials for electrochemical applications.

The integration of N-G materials with porous three-dimensional carbon structures derived from ZIF-8 serves to improve the transport of reactants and products in electrochemical environments. Simultaneously, this integration exposes a greater number of active sites while preserving the structural robustness. Notably, in the existing literature, materials based on or derived from N-G/ZIF-8 have demonstrated an outstanding performance, frequently surpassing conventional catalyst and electrode materials in a variety of electrochemical energy systems [36–39].

Despite the considerable advancements in developing efficient battery systems for electrochemical energy storage, certain theoretically high-potential batteries still face unresolved challenges. These issues include electrode volume expansion during charging and discharging, sluggish reaction kinetics, the formation of solid electrolyte interfaces (SEIs), and the dissolution of active ions in the electrolytes [40–47]. To overcome these challenges, several research groups have explored the potential of N-G/ZIF-8-based/derived materials, which combine the electronically active nature of N-G materials with the structurally advantageous properties of ZIF-8 [48–52]. Through various synthesis techniques, these materials demonstrate the ability to facilitate fast reactant transport, improve electrochemical interactions, and maintain a reasonable structural integrity. These promising characteristics show viable ways to address critical concerns and advance the practical application of high-potential batteries.

Electrochemical capacitors, fundamentally similar to batteries, are highly regarded as convenient and efficient energy storage devices. They utilize two distinct mechanisms for charge storage [53–56]: (1) electrical double-layer capacitors (EDLCs) or supercapacitors, where active ions are electrostatically adsorbed on the electrode's active sites, allowing for rapid charging and discharging with remarkable power density; on the other hand,

(2) pseudocapacitors, where active ions undergo reversible electrochemical reactions with the electrode's active elements, allow for the storage of a large amounts of charge and result in high energy density.

Focusing on these promising mechanisms, numerous research groups have explored the synergistic potential of combining electrochemically active N-G materials, which can facilitate reversible faradic activity, with the structural advantages of ZIF-8, which can host a larger number of exposed active sites, enhancing the electrostatic adsorption of ions [57–63]. Moreover, N-G/ZIF-8-based/derived materials possess the unique capability to support and protect other functional elements within their structures, further enriching their versatility and potential applications. Through extensive studies, these advanced materials have demonstrated impressive supercapacitive and pseudocapacitive activities. As a result, N-G/ZIF-8-based composites emerge as promising candidates for the development of cutting-edge electrochemical capacitors that can effectively address the challenges posed by conventional systems.

In fuel cells, catalysts are essential to enhance slow electrochemical reactions occurring on the electrode's surface. Traditionally, expensive catalysts based on platinum group metals (PGMs) are used to promote the oxygen reduction reaction (ORR), particularly on the cathode's surface [64–66]. Numerous research groups have focused on improving the electrocatalytic activities of N-G-based materials to match the performance of PGM-based catalysts [67–76]. A number of these studies have explored various synthesis methods, characteristics, and electrochemical performances of N-G/ZIF-8-based/derived materials. Most of these investigations rely on experiments and compare the electrocatalytic performances of these materials with their precursors and standard catalysts, like Pt/C and RuO₂ [36–39,77–82]. The reported studies consistently demonstrated significantly enhanced electrocatalytic performances of N-G/ZIF-8-based/derived materials. Also, the researchers offered explanations for how the synthesis process could fine-tune the material's activities and discussed the observed improvements in the catalytic performance from different perspectives.

In addition to their applications in energy systems, graphene/MOF-based materials have garnered significant interest for a wide range of uses, including chemical sensors [83–90], biosensors [91–93], water purification [94–97], gas separation and storage [98–103], and medical therapy [104,105], among others. With their impressive performances in various applications, researchers are increasingly keen to comprehensively understand the synthesis, characteristics, and functionalities of these materials. While a few reviews exist in the literature attempting to address these aspects, the term 'graphene/MOF' encompasses a vast array of composites comprising all the feasible combinations of the materials from graphene and MOF families, making it challenging to navigate through specific applications or functionality-oriented sets of graphene/MOF combinations [25,26,28–30]. Therefore, there is a pressing need to develop a series of reviews that specifically target distinct sets of graphene/MOF composites designed for particular functionalities or applications. This strategic initiative will enable researchers to delve deeply into the unique characteristics and functionalities of these specific graphene/MOF composite sets tailored for their intended uses. By focusing on particular applications, these specialized reviews can unlock valuable insights, driving further advancements in these materials and their potential for widespread development and implementation.

In this comprehensive review, we conducted a thorough examination of materials based on or derived from N-G/ZIF-8 that have been advanced for applications in electrochemical energy over the past decade. Our investigation delves into the synthesis processes' trends and characteristic features while placing particular emphasis on understanding the performance and fundamental functionalities of these N-G/ZIF-8 materials, as documented in the literature. To provide a structured analysis, the discussions are categorized into three major electrochemical applications: electrode materials for batteries, electrochemical capacitors, and electrocatalysts. By critically evaluating the existing research, our aim is twofold: firstly, to shed light on the progress made in the development of N-G/ZIF-8-

based/derived materials for energy applications; and secondly, to identify and highlight any existing research gaps in this domain. These findings are imperative for guiding future research initiatives, thereby promoting more efficacious advancements in the conceptualization and utilization of N-G/ZIF-8-based/derived materials within diverse electrochemical energy systems.

2. N-G/ZIF-8-Based/Derived Materials as Battery Electrodes

Currently, batteries are widely recognized as the most convenient electrochemical energy storage systems, and considerable efforts have been dedicated to their development and enhancement. Despite these endeavors, various challenges persist, including sluggish reaction rates, irreversible electrochemical reactions, the formation of a solid electrolyte interface (SEI), and electrode volume expansion [106]. To address these issues, several research groups have explored the use of composite materials based on N-doped graphene and MOF(ZIF-8) as battery electrodes [48–52]. The literature reveals that N-G/ZIF-8-based/derived composite materials not only offer improved structural stability for the electrodes, but also enhance the electrochemical kinetics by providing a host of different active sites. This section provides a concise overview of the synthesis processes, material characteristics, and functionalities of a series of N-G/ZIF-8-based/derived composite materials, developed in the past decade, and their potential as promising solutions to the challenges faced by conventional battery electrodes.

2.1. Synthesis Trends and Characteristics of N-G/ZIF-8-Based/Derived Battery Electrodes

One of the first attempts at preparing anodes for lithium-ion storage from ZIF-8-derived N-doped graphene materials was reported by Zheng et al. in 2014 [107]. Aiming to achieve a higher nitrogen doping level compared to the contemporary attempts (~10 wt% of N doping), they opted to leverage the ZIF-8's elemental composition's ($C_3H_{10}N_4Zn$) aspect of having a high nitrogen content of around 30 at% (excluding the hydrogen content) to form an N-doped graphene material. They first synthesized ZIF-8 through a room-temperature chemical process. Then, the ZIF-8 was subjected to thermal annealing in a nitrogen atmosphere at different elevated temperatures (500 to 900 °C) for 8 h applying a 5 °C/min heating rate. The final product maintained the framework structure and contained 17.72 wt% of nitrogen. Through characterizations by XRD and Raman spectroscopy, the presence of a zeolitic structure and graphitic characteristics was confirmed for the material. As an anode, this material generated a high reversible specific capacity of 2037 mAh·g⁻¹ with a coulombic efficiency of around 58.4%. The high specific capacity of the materials was attributed to the high nitrogen content.

Martín-Jimeno et al. introduced a novel approach called 'nanopore lithography' to achieve the uniform porosity of ZIF-8, with the intention of using it as an electrode material in energy storage systems [48]. They emphasized that the lack of a considerable proportion of mesopores hindered the performance of such materials in electrochemical applications. To address this, they devised a chemical process to coat the ZIF-8 with GO (graphene oxide) sheets. This ZIF-8/GO hybrid was then subjected to pyrolysis in an inert environment at various temperatures ranging from 700 to 1000 °C. Subsequently, the material underwent activation using a specific KOH solution. Figure 1 illustrates the schematic of the 'nanopore lithography' process.

During the carbonization process, incipient pores were generated on the GO cover through the thermal etching of the highly oxidized regions of the GO, while the inner ZIF-8 core remained unaffected. The activation process using KOH resulted in the formation of uniform micropores in the composite, following the incipient pores on the GO sheet. Consequently, the composite sample exhibited a more uniform microporosity compared to the precursors. The material's nitrogen doping content was confirmed, and four nitrogen functional groups were identified: pyridinic-N, pyrrolic-N, graphitic-N, and pyridinic-N-oxide.

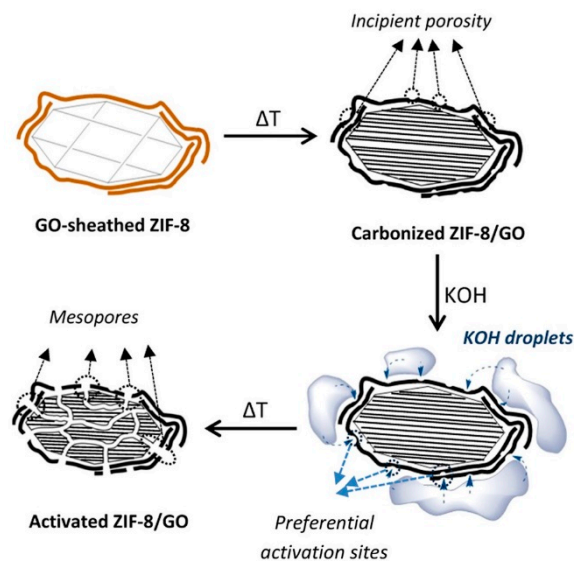


Figure 1. Schematic of the generating mesopores in GO-covered ZIF-8 by the ‘nanopore lithography’ process by Martín-Jimeno et al. [48] (images used with permission from the American Chemical Society).

As a sulfur host material in Li-S batteries, Ding et al. developed a 3D porous carbon framework (referred to as PCF) with a unique structure comprising polyhedral-shaped hollow carbon coated with reduced graphene oxide (rGO) [49]. The main goal for creating this material was to address the challenge of the spontaneous dissolution and diffusion of soluble lithium polysulfide intermediates in Li-S batteries, a phenomenon known as the shuttle effect, which negatively impacts a battery’s performance. To achieve this, they initially mixed ZIF-8 and GO suspensions in a specific ratio (2:15 mass ratio) through stirring. The charge differences between the ZIF-8 and GO (expressed as zeta potentials) led to the formation of a ZIF-8/GO composite through an electrostatic self-assembly process. This composite was then subjected to pyrolysis at 900 °C in a nitrogen atmosphere, transforming it into the desired structure of rGO-covered hetero-structured porous carbon with polyhedral-shaped hollow carbon. The resulting composite exhibited the expected morphological structure, as anticipated by the researchers. XPS analyses confirmed nitrogen doping in the material, with the dominant nitrogen contents identified as pyridinic-N and graphitic-N functional groups. These functional groups were considered as the potential active sites in the material. Figure 2 illustrates the schematic of their synthesis process and an STEM image showcasing the synthesized PCF material.

Considering the advantageous presence of nitrogen and carbon atoms in the ZIF-8, Tai et al. produced N-doped ZIF-8-derived carbon by calcinating the material at different temperatures in the range of 600–900 °C [108]. The process involved synthesizing the ZIF-8 by a solvothermal method first, then calcinating dried ZIF-8 powder at different elevated temperatures in a nitrogen atmosphere for 2 h at a heating rate of 5 °C/min. Depending on the calcination temperatures, the samples were denoted as NC-600, NC-700, NC-800, and NC-900. An acid (diluted HCl) wash and subsequent drying were carried out for the NC-800 sample. The schematic of the synthesis process and the SEM and TEM images of the final materials are shown in Figure 3.

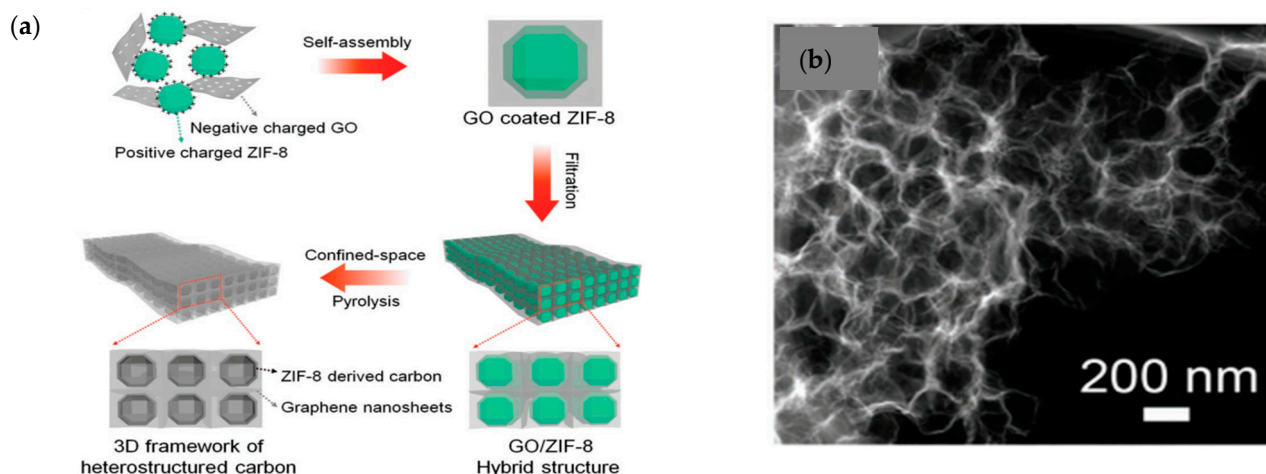


Figure 2. (a) Synthesis process schematic of PCF derived from GO and ZIF-8 and (b) STEM image of the PCF composite by Ding et al. [49] (Images used with permission from John Wiley and Sons).

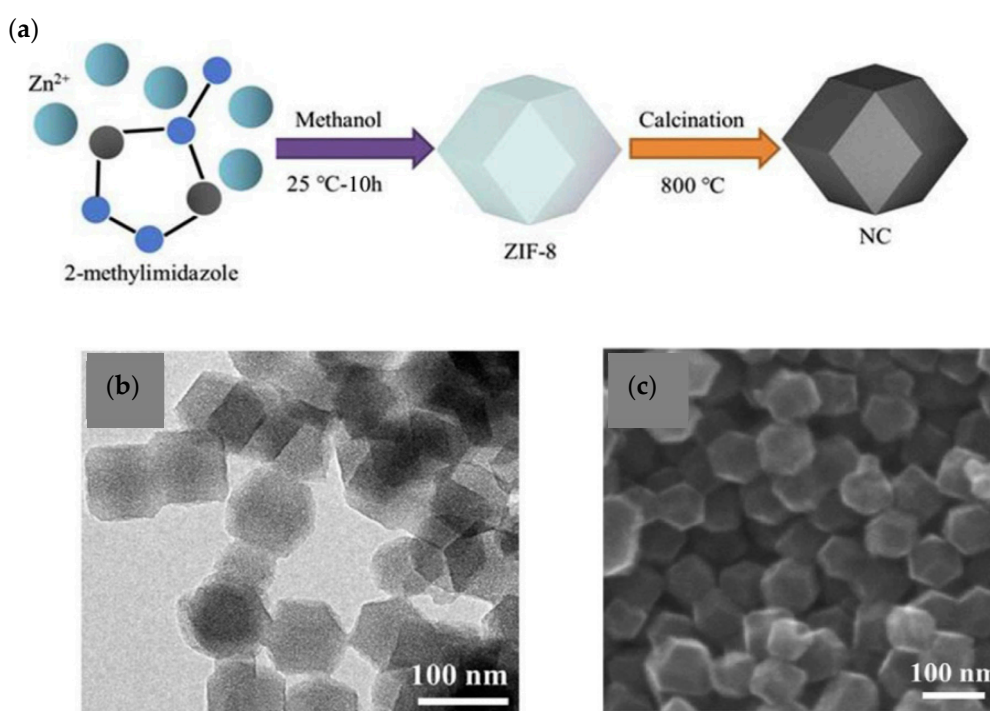


Figure 3. (a) Schematic of the ZIF-8-derived N-doped carbon synthesis process by Tai et al. [108]. (b) TEM and (c) SEM images of the NC-800 sample (images used with permission from Elsevier).

The Raman spectroscopy analysis of the samples showed that the I_D/I_G ratios were in the range of 0.92–1.33, indicating the graphitization of the material with a considerable presence of defects. Through the BET surface area analysis, it was shown that the specific surface area of the materials increased proportionally with the calcination temperature. The continuous removal of the zinc atoms at higher temperatures was justified by such an observation. This zinc removal process was also claimed to produce a higher porosity in this 3D framework structure. The elemental-level analysis of the samples by XPS suggested the presence of different C-N bonds, such as pyridinic-N and pyrrolic-N, in the material.

Wang et al. addressed the challenge of addressing weak interactions between ZIF-8 and rGO when preparing composites for use as sulfur hosts in Li-S batteries to prevent the ‘shuttle effect’ [50]. They observed that a simple mixture of ZIF-8 and rGO resulted in a low capacity and limited coulombic efficiency, as the ZIF-8 particles tended to detach from the

rGO surface due to weak bonding. Additionally, the ZIF-8 particles tended to agglomerate because of the surface tension of rGO. To overcome these issues, the researchers adopted a different approach by creating a ZIF-8@rGO composite through the facile hydrothermal conversion process of a $\text{Zn}_5(\text{OH})_6(\text{CO}_3)_2$ @rGO precursor with 2-methylimidazole. They avoided using high-temperature carbonization. Finally, they prepared a ZIF-8@rGO/S composite to evaluate its performance in preventing the 'shuttle effect' during Li-S battery operations. By deconvoluting the XPS S 2p narrow-scan spectra of the material, the researchers confirmed the existence of the Zn-S bond in the ZIF-8@rGO/S composite, demonstrating that ZIF-8 could effectively interact with the sulfur atoms of polysulfides, immobilizing them at the Zn sites.

Zhang et al. investigated the challenges faced by conventional anodes in potassium-ion batteries (PIBs) due to the large radius of potassium ions (K^+), leading to significant volume changes and slow reaction kinetics [51]. Such an issue ultimately leads to an inferior structural stability and weak electrochemical activity for the PIB anodes. To address these issues and enhance the performance of PIB anodes, they introduced a novel zinc-cobalt bimetallic selenide material ($\text{ZnSe}/\text{Co}_{0.85}\text{Se}@\text{NC}@\text{C}@\text{rGO}$) and evaluated its synthesis, characterization, and performance in PIBs. They employed a multilevel space confinement process to create this material, involving the carbonization and subsequent salinization of a 2D graphene-encapsulated and resorcinol-formaldehyde (RF)-coated ZIF-8/ZIF-67 composite. It was presented that this ZIF-8/ZIF-67-derived highly porous carbon could provide a certain space margin to accommodate the volume stress arising from the repeated insertion and extraction of K^+ ions. The material's porosity offered ample channels for efficient ion and electron transfers, facilitating electrolyte transport, and exposing active sites to reactant species. The material was found to contain elements such as N, O, Zn, Co, and Se embedded in a carbon matrix. The presence of pyridinic-N, pyrrolic-N, and graphitic-N functional groups was confirmed, suggesting their potential roles in facilitating ion transport and enhancing the electron-donating capabilities of the material.

Although silicon has the potential to be a high-capacity anode material in lithium-ion batteries (LiBs) due to its ultra-high theoretical capacitance, its practical application is hindered by challenges, such as lower conductivity, volume expansion during electrochemical processes, and the formation of a solid electrolyte interface (SEI). To address these issues, metal silicate-based materials have shown promise as electrode materials for LiBs. In this context, Guo et al. synthesized a composite material consisting of cobalt silicate (CSO) integrated with rGO and ZIF-8, denoted as CSO/rGO/ZIFC [52]. The synthesis involved a series of solvothermal processes to create a $\text{Co}_2\text{SiO}_4/\text{GO}/\text{ZIF}$ composite, followed by calcination at 800 °C to obtain the final product. The resulting material exhibited a 3D porous morphology with a carbon network structure. A ZIF-8 layer was formed over the CSO/rGO/ZIFC surface, and upon calcination, the evaporation of Zn created a highly porous morphology. The synthesis process and the morphology of the CSO/rGO/ZIFC material are illustrated in Figure 4, as shown in the SEM and TEM images. The material contained Co, Si, C, N, O, and Zn elements. Pyridinic-N, pyrrolic-N, and graphitic-N functional groups were identified in the material, and it was suggested that these groups contributed to the anodic performance of the material in lithium-ion batteries (LiBs) by improving electron conductivity.

Chen et al. prepared an N-doped nanoporous carbon matrix by carbonizing ZIF-8 and then integrated it with sulfur producing a cZIF-8/S composite to apply as a cathode material for sodium-sulfur (Na-S) batteries [109]. Their synthesis process involved the chemical synthesis of ZIF-8 and carbonizing it to 800 °C for 2 h with a 2 °C/min heating rate. Then, the carbonized ZIF-8 or carbon matrix was impregnated with sulfur to produce the cZIF-8 composite. Through XRD and XPS analyses, the formation of a disordered graphene structure (ID/IG ratio of 1.11) and the presence of different nitrogen functional groups (pyridinic-N, pyrrolic-N, and quaternary/graphitic-N) were confirmed. The cZIF-8 exhibited a BET surface area of approximately 627 m^2/g .

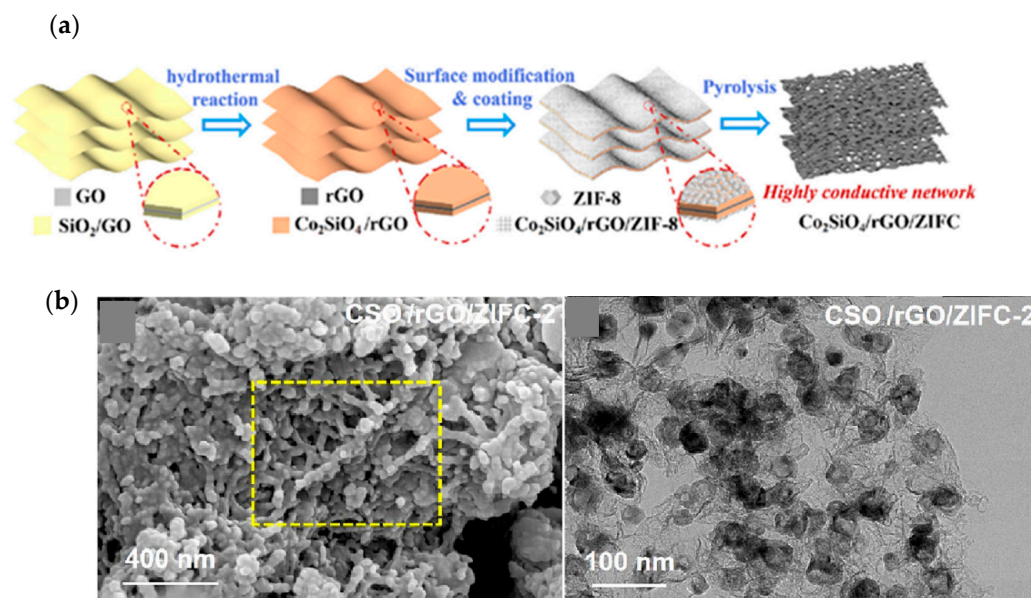


Figure 4. (a) Synthesis process schematic of CSO/rGO/ZIFC by Guo et al. and (b) SEM and TEM images of the CSO/rGO/ZIFC [52] (images used with permission from Elsevier).

For anode materials of LiBs, employing a pyrolysis process, Liu et al. synthesized N-doped porous carbon-coated graphene (rGO) sheets (NPCGSs) with an in situ-grown ZIF-8 on a GO precursor [110]. The ZIF-8 particles were grown on GO sheets through a chemical process. Then, they were heated to 800 °C for 5 h at a 3 °C/min heating rate. A final acid (33 wt% HCl) wash was provided to the material to remove excess Zn and other impurities. The materials exhibited both graphene-like and ZIF-8-like morphological features. The presence of different nitrogen functional groups, such as pyridinic N, pyrrolic N, and graphitic N, was confirmed in the materials by the XPS study. The material had a BET-specific surface area of 781.3 m²/g and the pore sizes were concentrated around 0.55 and 1.5 nm.

Upon reviewing these N-G/ZIF-8-based/derived materials developed as electrode materials for different battery systems, mostly for metal-ion batteries, it was generally understood that the synthesis processes followed a common trend. Mostly, we started with the chemical synthesis of ZIF-8 following somewhat similar processes. Then, they proceeded to prepare an N-G and ZIF-8 mixture. Then, we followed a common carbonization step for this mixture at elevated temperatures in the range of 600 to 1000 °C for a period ranging from 2 to 5 h at a heating rate range of 2 to 5 °C/min. This carbonization process introduced graphene-like chemical structural features with a variety of defects in the materials. The materials tended to have a combination of micropores and mesopores with considerably extended surface areas. Most of the analysis showed the presence of nitrogen functional groups, such as pyridinic-N, pyrrolic-N, and quaternary/graphitic-N, which were the presumed active centers of these materials.

2.2. Performance and Functionalities of N-G/ZIF-8-Based/Derived Battery Electrodes

This subsection is dedicated to thoroughly reviewing the electrochemical performance of the above-discussed N-G/ZIF-8-based/derived composites as electrodes of different battery systems. Also, a careful observation was performed to understand how the materials' electrochemical functionalities were justified conforming to their structural and chemical properties. In general, these materials were observed to aid in managing different concurrent battery-electrode-related issues, such as volume expansion and irreversible ion dissolution. The key discussions in this section begin at this point.

According to the electrochemical performance data presented by Martín-Jimeno et al., the sample that underwent carbonization at 800 °C followed by activation with a specific

amount of KOH (KOH/precursor weight ratio of 1) showed the highest capacitive storage and well-defined redox activity [48]. This particular sample was labeled as ZIF-8/GO (1|800). As shown in Figure 5, the curves of the front and reverse pulses in square wave voltammetry (SWV) indicate that this sample allows almost fully reversible redox reactions compared to their other samples, which is a crucial characteristic for energy storage system electrodes.

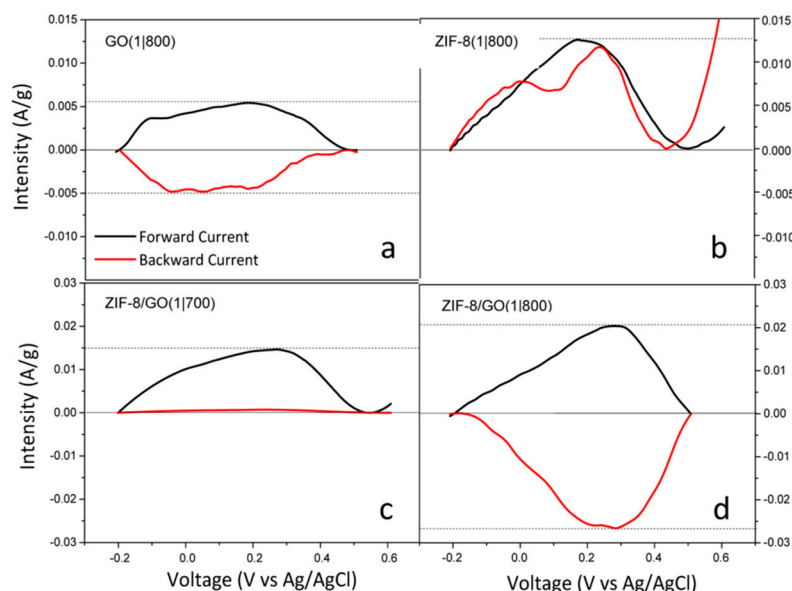


Figure 5. Front (black line) and reverse (red line) pulses of SWV curves in the anodic sweep of Martín-Jimeno et al.'s material samples: (a) GO(1|800); (b) ZIF-8(1|800); (c) ZIF-8/GO(1|700); and (d) ZIF-8/GO(1|800) [48] (the figures are presented with permission from the American Chemical Society).

The authors analyzed the SWV data to attribute the voltage-specific current flows observed for the sample electrodes to various probable faradic phenomena (provided in the Supporting Information of Martín-Jimeno et al. [48]). Nonetheless, in this study, the comparison of electrode performance was limited to different composite samples prepared with varied carbonization temperatures and individual precursors (GO and ZIF-8). Nevertheless, the study showcased a well-defined technique that could be employed to optimize the pore structures of graphene/ZIF-8-based materials and achieve improved electrode properties.

The applicability of Ding et al.'s PCF composite as a sulfur host material for Li-S batteries was assessed by creating a PCF/sulfur composite electrode through a slurry coating process [49]. This composite electrode was then subjected to CV measurements in an electrochemical environment simulating the conditions of an Li-S battery (Figure 6a). The CV curves exhibited well-defined peaks during both the cathodic and anodic processes, indicating a two-step reduction of elemental sulfur to $\text{Li}_2\text{S}_n/\text{Li}_2\text{S}_2/\text{Li}_2\text{S}$ and the subsequent oxidation of Li_2S_n back to elemental sulfur, respectively. The CV curves maintained a consistent shape over four cycles, leading to the conclusion that the PCF composite effectively mitigated the shuttle effect, which is a desirable property for Li-S batteries. The data also indicate promising charging and discharging capacities for the PCF composite; an initial capacity of 1339 mAh/g at 0.1 C was generated, as seen in Figure 6b. Also, the material retained a capacity of 1046 mAh/g (starting from 1335 mAh/g) at 0.5 C after 500 cycles, which was a capacitance retention of 79.7%. As shown in the XPS N 1s spectra, in Figure 6c, the PFC composite contains a higher ratio of pyridinic-N and graphitic-N, which are ascribed as the key active sites for the material.

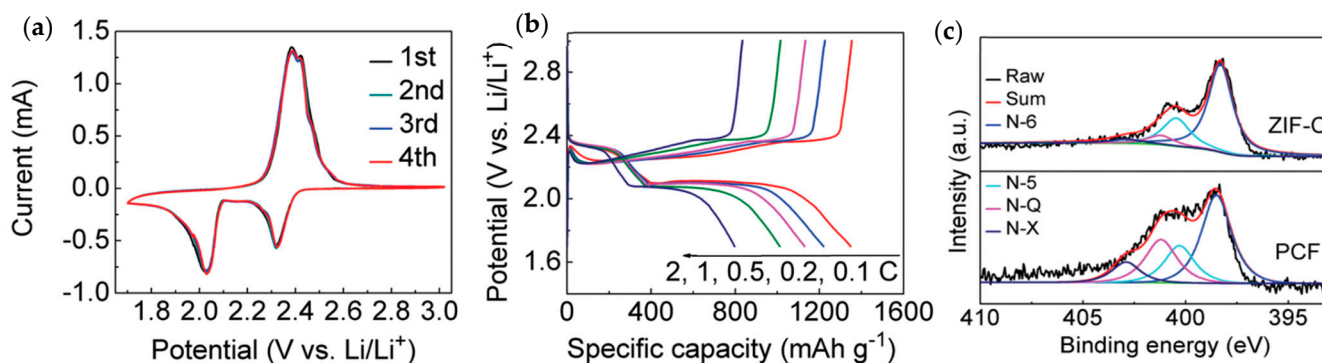


Figure 6. (a) CV plots for PCF/S electrode for the first four cycles; prepared by Ding et al. [49]. (b) Specific capacitance measurements of the PCF/S electrode at different current rates (indicated by different colors); (c) XPS N 1s spectra analyses of ZIF-C and PFC (N-6 → pyridinic-N, N-5 → pyrrolic-N, N-Q → graphitic-N, and N-X → oxidized-N) (image used with permission from John Wiley and Sons).

However, the study did not explicitly explain the underlying mechanisms that contributed to the functionality of the composite, apart from identifying the presence of two critical nitrogen functional groups. Further research is needed to achieve a greater understanding of how the material's chemical and structural features contribute to its ability to manage the shuttle effect effectively. Investigating these aspects will shed more light on the rationale behind the composite's electrochemical performance in Li-S batteries.

The electrochemical performance of Tai et al.'s NC-800 samples (depicted as the best-performing one) was first evaluated by cyclic voltammetry (CV) tests within 0.01 to 3 V at a 0.1 mV/s scan rate [108]. As seen in Figure 7a, although a strong redox peak can be observed at 0.41 V in the first cycle indicating the formation of a solid electrolyte interface (SEI) layer, this peak is absent from the subsequent cycles, indicating fair reversibility in the charge–discharge process. The anode prepared for LIBs with this sample was tested by galvanostatic charge–discharge cycles in a voltage range of 0.01–3.0 V. Conforming to the CV results in the first cycle, a higher specific discharge capacity of 815.15 mAh/g was observed, as seen in Figure 6b. In the two subsequent cycles, the capacities were 464.96 and 453.29 mAh·g^{−1}, respectively. It can be assumed that the redox interaction contributes to a considerable portion of pseudocapacitance in the first cycle. The cyclic performance of the LIB anode with the samples was measured at 100 mA/g over 100 cycles, presented in Figure 6c. The NC-800 sample retained 94.7% of the initial capacity after 100 cycles and the coulombic efficiency was 56%.

Wang et al. reported that CV curves for the initial five cycles with the ZIF-8@rGO/S electrode showed that the electrochemical reaction in the Li-S battery was fairly reversible in the electrode, and the ZIF-8@rGO host effectively curbed the dissolution of polysulfides [50]. As shown in Figure 8, the cyclic performance of the ZIF-8@rGO/S sample as a cathode surpassed that of the precursor ZIF-8/S material by elevating the initial discharge capacity by about 338 mA·h/g (from 1206 to 1544 mA·h/g) measured at 0.2 A/g. After 200 cycles, the ZIF-8@rGO/S composite also retained a higher capacity than the ZIF-8/S composite. The coulombic efficiency during this test was measured at 98.6% with the ZIF-8@rGO/S cathode. Additionally, a persistent improvement in the cyclic performance of ZIF-8@rGO/S was observed for 300 charging and discharging cycles measured at 0.1 A/g. This study articulated that the presence of rGO in the ZIF-8@rGO/S cathode improved the electrical conductivity and helped suppress the volume change in sulfur during cycling, thereby enhancing the coulombic efficiency.

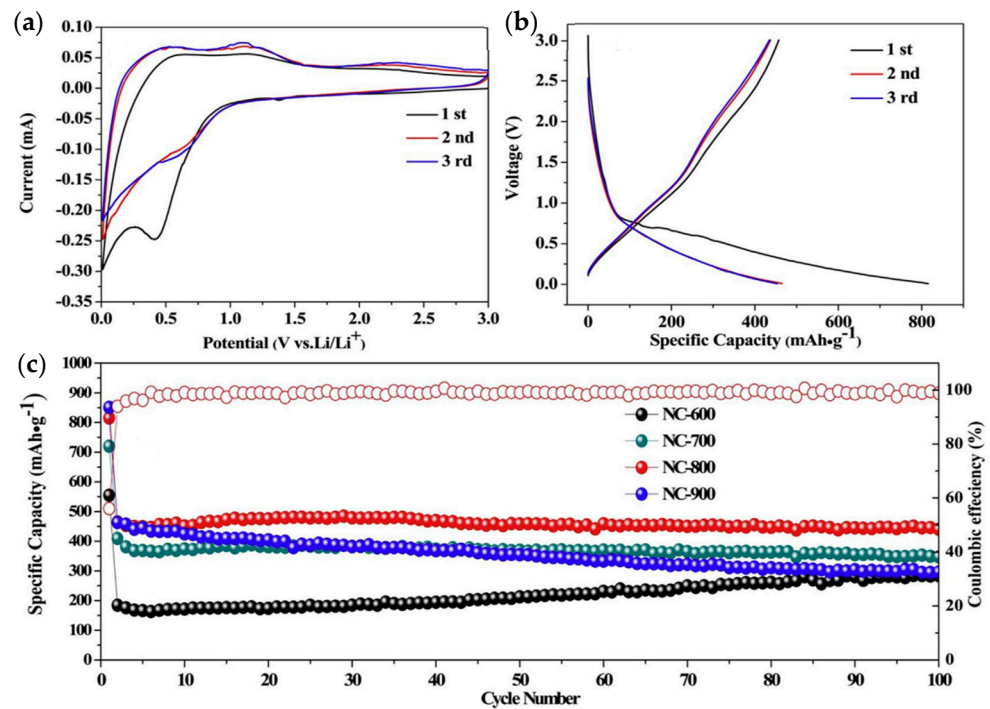


Figure 7. Reported by Tai et al. [108] (a) CV plots with NC-800 for three cycles at a 0.1 mV·s⁻¹ scan rate. (b) The charge–discharge curves of the NC-800-made LIB anode at 100 mA·g⁻¹. (c) The cycling performance plots of the NC-600, NC-700, NC-800, and NC-900 LIB anodes at 100 mA·g⁻¹, coulombic efficiencies of the NC-800 sample are presented by red hollow circles for 100 cycles (image used with permission from Elsevier).

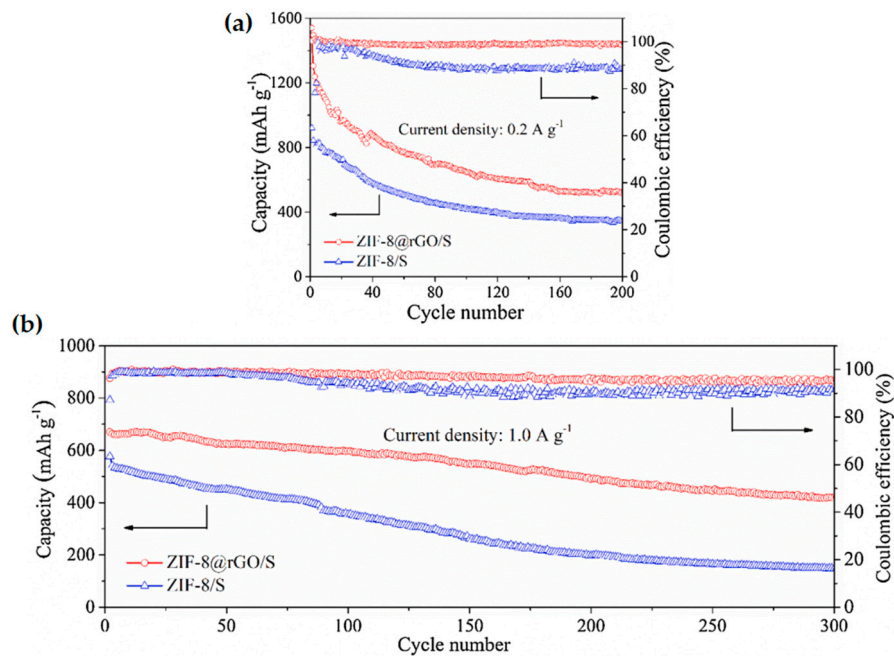


Figure 8. Measurements of cycling capacities with ZIF-8@rGO/S and ZIF-8/S and cathodes by Wang et al. at (a) 0.2 A/g for 200 cycles and (b) at 1.0 A/g for 300 cycles [50] (image used with permission from Elsevier).

Zhang et al.'s zinc–cobalt bimetallic selenide material (ZnSe/Co_{0.85}Se@NC@C@rGO) exhibited an excellent capacitive behavior, attributed to its large surface area and abundance of active sites [51]. The low-charge-transfer resistance indicated the efficient transfer of

K^+ ions within the material. Through the ex situ XRD and XPS analyses conducted at different charging and discharging stages, the mechanisms of K^+ ion storage and release in the material were proposed. According to their findings, the storage of K^+ ions in the material involved conversion-alloy reactions. During the discharging process, ZnSe converts into Zn and K_2Se , and Zn also forms KZn_{13} , while $Co_{0.85}Se$ transforms into Co and K_2Se . Conversely, during the charging process, K^+ ions are released from the K_2Se components. These insertion and de-insertion reactions of K^+ ions were observed to be highly reversible, indicating the material's potential for stable and efficient cycling in PIBs. In a recent study, Deng et al. synthesized hierarchically porous nitrogen-doped carbon (HPNC) as a host for an Se cathode, aiming to enhance the performance of Li–Se batteries. The Se/HPNC cathode could attain a discharge capacity of 582 mAh/g at 0.2 C with a 90.5% capacity retention rate [111].

The best-performing sample of CSO/rGO/ZIFC produced by Guo et al. exhibited a specific capacity of 1295 mA h/g at 0.2 A/g, as presented in Figure 9a. The coulombic efficiency of this sample remained at 100% even after 250 cycles, as observed in Figure 9b [52]. Based on the electrochemical characterization data, the material also demonstrated a high Li-ion diffusion coefficient and a lower circuit resistance. The authors attributed the improved performance of the composite to several factors. The 2D rGO acted as a lamellar template and supporting substrate, enhancing the electrical conductivity of the material. The porous structure derived from ZIF-8 facilitated the diffusion of Li-ions, and it also helped in mitigating the volume expansion during the operation and promoted favorable electrochemical interface reactions.

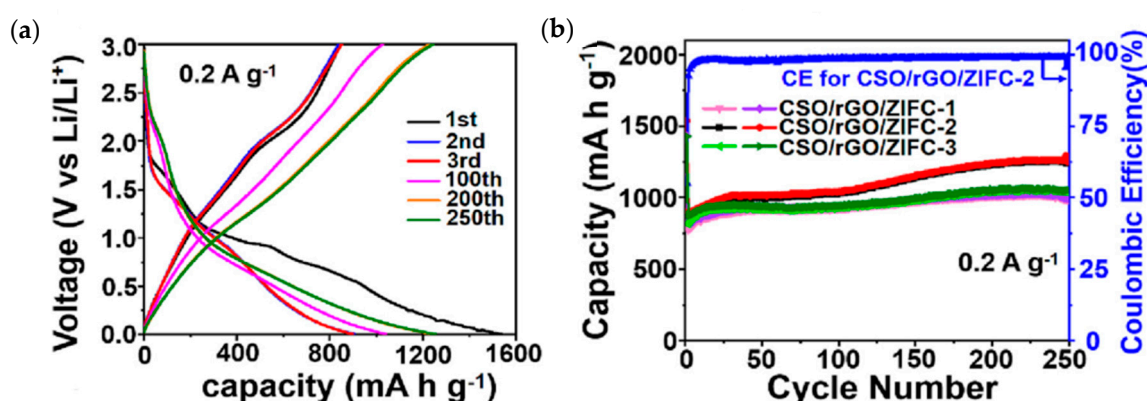


Figure 9. (a) Charge–discharge voltage plots of the CSO/rGO/ZIFC-2 sample at 0.2 A/g from 1 to 250 cycles. (b) Cycling performance curves of the CSO/rGO/ZIFC samples', and the coulombic efficiency curve of the CSO/rGO/ZIFC-2 sample up to 250 cycles. The results obtained by Guo et al. [52] (images used with permission from Elsevier).

The cZIF-8/S composite synthesized by Chen et al., as an Na-S battery cathode, generated specific capacities of 1000, 850, 650, 480, 220, and 850 mAh/g at the current densities of 0.1 C, 0.2 C, 0.5 C, 1.0 C, 2.0 C, and 0.1 C, respectively. The capacity retention was 60% when, for the first 5 cycles, the current density was kept at 0.1 C and then at 0.2 C for 250 cycles [109].

As an anode material of a LiB test system, Lui et al.'s NPCGS composite generated initial charge and discharge capacities of 873 and 1391 mAh/g, respectively, at 0.5 A/g current densities [110]. The initial coulombic efficiency (CE) was approximately 62.7%. This low initial value of CE indicated a possible formation of solid–electrolyte interphase (SEI) film. Nonetheless, the data show that the coulombic efficiency reaches 100% after 200 cycles. In the rate performance tests, the NPCGSs produced capacities of 936, 854, 806, 728, 652, 606, 546, and 459 mAh/g at current densities of 0.1 to 0.2, 0.4, 0.6, 0.8, 1, 2, and 4 A/g, respectively. When the current density returned to 0.1 A/g, the capacity returned to 930 mAh/g.

The capacitive performances of the above-discussed N-G/ZIF-8-based/derived materials developed as different battery electrodes are summarized in Table 1.

Table 1. Discharge capacitive performances of the N-G/ZIF-8-based/derived materials for different battery/energy storage systems.

Material	Discharge Capacitive Performance (of the Best Sample)
N-doped graphene analogousp articles (Anode materials for LIBs) (Zheng et al.—2014 [107])	<ul style="list-style-type: none"> • Specific discharge capacity: 2037 mA·h/g at 100 mA/g. • Capacity retention: 99.2% after 50 cycles at 100 mA/g. • Coulombic efficiency: ~53.4% over 200 cycles at 500 mA/g.
Activated ZIF-8/GO (General energy storage materials) (Martín-Jimeno et al.—2017 [48])	<ul style="list-style-type: none"> • Specific capacitance: 241 F/g calculated from CV measurement in 1 M of H₂SO₄ at a 2 mV/s scan rate. • Capacitance retention: not specified.
Three-dimensional porous carbon framework (PCF) (Host material for Li–S batteries) (Ding et al.—2019 [49])	<ul style="list-style-type: none"> • Specific capacitance: 1339 mAh/g at 0.1 C or a 167.5 mA/g current rate (1 C = 1675 mA/g). • Capacitance retention: 79.7% after 500 cycles at 0.5 C. • Coulombic efficiency: 100% over 650 cycles at 1 C.
N-doped ZIF-8-derived carbon (NC-ZIF) (Anode materials for LIBs) (Tai et al.—2019 [108])	<ul style="list-style-type: none"> • Reversible specific capacity: ~453–465 mAh/g at 100 mA/g. • Capacitance retention: ~94.7% after 100 cycles at 100 mA/g. • Coulombic efficiency: ~56% over 100 cycles at 100 mA/g.
ZIF-8 nanocrystals attached to reduced graphene oxide/sulfur (ZIF-8@rGO/S) (Cathode material for Li-S batteries) (Wang et al.—2021 [50])	<ul style="list-style-type: none"> • Specific capacitance: 1297 mAh/g at 100 mA/g. • Capacitance retention: ~33.87% after 200 cycles at 200 mA/g. • Coulombic efficiency: 98.6% over 100 cycles at 200 mA/g.
Zinc–cobalt bimetallic selenide (ZnSe/Co _{0.85} Se@NC@C@rGO) (Anode material for PIBs) (Zhang et al.—2023 [51])	<ul style="list-style-type: none"> • Specific capacity: 422.2 mAh/g at 100 mA/g. • Capacitance retention: ~83.2% after 2000 cycles at 2000 mA/g. • Coulombic efficiency: 100% over 2000 cycles at 2000 mA/g.
Three-dimensional porous Co ₂ SiO ₄ /rGO/ZIFC conductive network (Anode materials for LIBs) (Guo et al.—2023 [52])	<ul style="list-style-type: none"> • Specific capacitance: 1060 mAh/g at a 200 mA/g current density. • Capacitance retention: not specified. • Coulombic efficiency: 100% over 250 cycles.
N-doped nanoporous carbon matrix with sulfur (cZIF-8/S). (Cathode materials for Na-S batteries) (Chen et al.—2016 [109])	<ul style="list-style-type: none"> • Specific capacitance: 1000 mAh/g at 0.1 C or ~167.5 mA/g current density. • Capacitance retention: 60% after 250 cycles at 0.1 C for 5 cycles and then 0.2 C for 250 cycles.
N-doped porous carbon-coated graphene (rGO) sheets (NPCGSs). (Anode materials for LIBs) (Liu et al.—2016 [110])	<ul style="list-style-type: none"> • Specific capacitance: 936 mAh/g at a 100 mA/g current density. • Coulombic efficiency: 100% over 200 cycles.

In the electrochemical battery systems, as the energy is stored and released by means of different ion transfer processes to and from the electrodes and electrolytes, to study the electrode materials, the aspects of porosity are of significant interest. To this end, the porosity-related parameters of the N-G/ZIF-8-based/derived materials are meticulously compiled in Table 2. As the electrochemically assessable surface area is another crucial

parameter that is also related to the pore structure of the materials, the BET surface areas of these materials are also carefully noted here.

Table 2. Collected data of the porosity parameters of the N-G/ZIF-8-based/derived materials for application in battery systems.

Material	Pore Diameter (nm)	Pore Volume (cm ³ /g)	BET Surface Area (m ² /g)
N-doped graphene analogous particles (Zheng et al. [107])	2.02	0.32	634.6
Activated ZIF-8/GO (Martín-Jimeno et al. [48])	<1 to 4	1.219	1304
Three-dimensional porous carbon framework (PCF) (Ding et al. [49])	~0.6	0.35	643
N-doped ZIF-8-derived carbon (NC-ZIF) (Tai et al. [108])	~1.8 to 2.0<	~0.3	815.8
ZIF-8 nanocrystals attached to reduced graphene oxide/sulfur (ZIF-8@rGO/S) (Wang et al. [50])	3.4 to 15.5	0.329	905.6
Zinc-cobalt bimetallic selenide (ZnSe/Co _{0.85} Se@NC@C@rGO) (Zhang et al. [51])	~4.0	~0.12	232.51
Three-dimensional porous Co ₂ SiO ₄ /rGO/ZIFC conductive network (Guo et al. [52])	Not specified	0.50	210
N-doped nanoporous carbon matrix with sulfur (cZIF-8/S) (Chen et al. [109])	~0.5	Not specified	627
N-doped porous carbon-coated graphene (rGO) sheets (NPCGSs) (Liu et al. [110])	0.55, 1.5	Not specified	781.3

It is generally understood that mesopores (2 to 50 nm diameters) in carbon-based materials are advantageous for electrochemical activities [112–114]. Mesopores allow the facile penetration of the ions of the electrolyte in the material, hence increasing the effective mass transport for the electrochemical reactions. Nonetheless, micropores (less than a 2 nm diameter) also hold some significance in maintaining the structural integrity of the materials. Most of the N-G/ZIF-8-based/derived materials were observed to have a combination of micropores and mesopores in various degrees, which apparently turned out to be advantageous for electrochemical activities.

3. N-G/ZIF-8-Based/Derived Materials for Electrochemical Capacitors

Electrochemical capacitors have garnered significant attention due to their energy efficiency and operational convenience. Researchers have extensively explored the use of carbon-based materials in electrochemical capacitors. In particular, graphene-based materials have been studied to enhance their electrochemical capacitive properties. To achieve this, several research groups have attempted to create N-doped graphene (N-G)-type materials from MOFs, specifically ZIF-8, or integrate the structural advantages of ZIF-8 with graphene [57–63]. In this section, as series of such research initiatives are

reviewed, focusing on the ideas, synthesis processes, material structures, and reported capacitive performances.

3.1. Synthesis Trends and Characteristics of N-G/ZIF-8-Based/Derived Electrode Materials for Electrochemical Capacitors

In an early study, Chaikittisilp et al. investigated the direct carbonization of ZIF-8 as a standalone carbon precursor at various temperatures ranging from 600 to 1000 °C under a nitrogen gas flow [57]. The purpose was to create nanoporous carbon for the potential use as a supercapacitor electrode. After carbonization, the ZIF-8-derived carbon underwent an acid-washing process using a hydrogen fluoride (HF) solution to remove residual inorganic components, such as Zn particles/atoms. In the SEM images, the material samples retained the sodalite crystal structure of ZIF-8, with the crystal structures shrinking at a carbonization temperature of 1000 °C. The carbonization and acid-washing processes increased the material's roughness. The researchers found that a carbonization temperature higher than 800 °C was necessary to produce a porous carbon framework from ZIF-8. At lower temperatures, although the organic linkers started to thermally decompose, the carbon networks did not evolve adequately to form the desired framework structure.

The Raman spectra analysis revealed that, regardless of the carbonization temperature, the materials exhibited a combination of graphitic and disordered carbon arrangements in their local structures. The presence of nanopores in the materials was confirmed through nitrogen adsorption measurements, with the BET surface area increasing with higher carbonization temperatures.

In an attempt to enhance the capacitive properties of graphene for electrochemical storage systems, Li et al. developed a composite material consisting of 3D graphene decorated with ZIF-8 [58]. The synthesis process involved several steps: first, they prepared a 3D graphene monolith from a GO aqueous dispersion using a hydrothermal reduction method. Next, ZIF-8 crystals were grown and deposited on the 3D graphene through a solvothermal process, resulting in a composite called G-ZIF-8. Finally, the G-ZIF-8 composite was subjected to carbonization at 800 °C for 4 h to obtain the final product, referred to as C-GZ. The SEM and TEM images of C-GZ revealed its mesoporous structure and disordered graphene layers with micropores. The synthesis process is illustrated and a TEM image of G-ZIF-8 is provided in Figure 10. The composite material possessed a surface area of approximately 280.4 m²/g. During carbonization, Zn atoms in the ZIF-8 were significantly reduced, as evidenced by XPS and energy-dispersive X-ray spectroscopy (EDS) analyses. The material's elemental composition mainly consisted of C, O, and N, with the XPS N 1s spectra analysis indicating the presence of pyridinic-N, pyrrolic-N, and graphitic-N functional groups in the material.

To exploit the synergistic advantages of integrating N-G and ZIF-8, where N-G prevents ZIF-8 particle agglomeration and ZIF-8 alleviates graphene sheet restacking during carbonization, Wang et al. successfully synthesized N-doped carbon decorated graphene sheets, referred to as NCGs [59]. The synthesis process involved preparing a sandwich-like structure by decorating a graphene oxide (GO) sheet with ZIF-8 nanoparticles through a solvothermal method. The negative charge on the GO sheet, attributed to oxygen functional groups, like carbonyl and carboxyl, facilitated electrostatic interactions with positively charged ZIF-8 nuclei, leading to the anchoring of ZIF-8 nanoparticles onto the GO surface. Subsequently, the ZIF-8/GO composite was subjected to carbonization at temperatures ranging from 600 to 800 °C under a nitrogen atmosphere to produce the NCGs.

TEM images revealed ZIF-8-like crystal-embedded porous structures combined with graphitic morphological features, as shown in Figure 11. The XPS survey scan spectra showed C, O, and N as the main elements of the material's composition. It was claimed that the Zn atoms vaporized during the carbonization process. A further analysis of the XPS N 1s spectra revealed that the dominant nitrogen functional groups in the material were pyridinic-N and pyrrolic-N, with the presence of graphitic-N also observed. The authors mentioned that both pyridinic-N and pyrrolic-N contributed to the capacitance

characteristic of the material. However, the specific influence of these nitrogen functional groups on the capacitive behaviors of the material remains to be fully understood and requires further investigation.

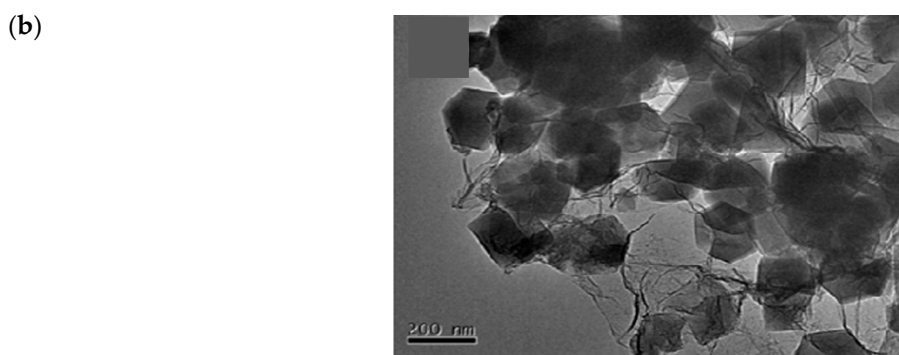
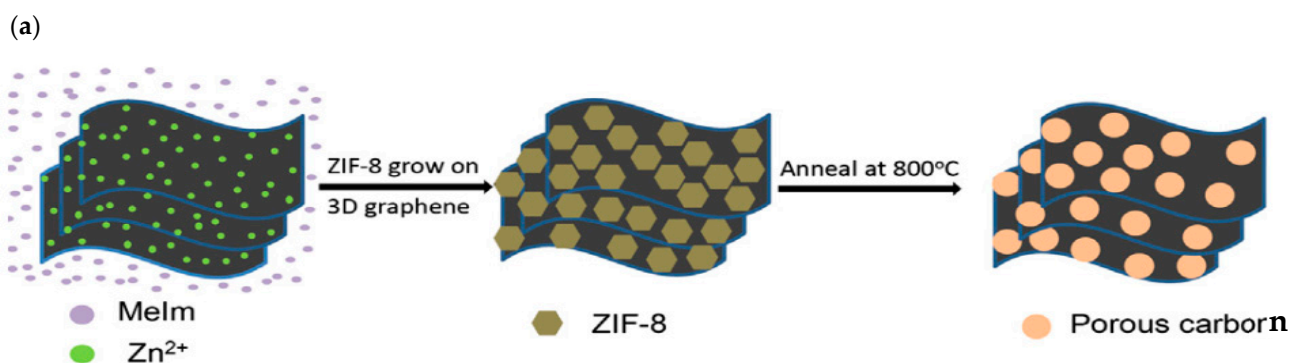


Figure 10. (a) Illustration of the synthesis process of G-ZIF-8 by Li et al. [58] and (b) TEM image of the G-ZIF-8 material (image used with permission from Elsevier).

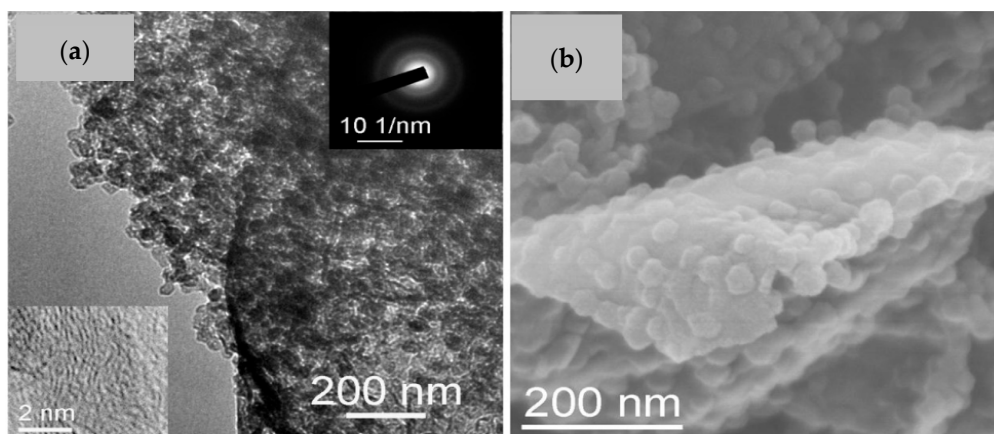


Figure 11. (a) TEM and (b) SEM images of the N-doped carbon-decorated graphene sheets (sample NCGs-800) by Wang et al. [59] (image used with permission from Elsevier).

Khakpour and colleagues aimed to create a supercapacitor composite by combining ZIF-8 and sulfur-doped graphene oxide (referred to as SGZ) [60]. They utilized a solvothermal process to initially produce S-doped-GO from graphene oxide and Na₂S. Subsequently, ZIF-8 was grown on the S-doped GO. The resulting material exhibited a surface area of 1030 m²/g and demonstrated mesoporous N₂ adsorption–desorption characteristics.

Xiao et al. aimed to develop a novel electrode material with the combined properties of physical ion adsorption/desorption for high power densities and an ultralong lifespan,

and reversible electrochemical redox reactions for high specific capacitance and high energy densities [61]. The goal was to employ this material in alkaline battery–supercapacitor hybrid devices. They achieved this by preparing a 3D composite using Zn–Co MOF and a graphene hydrogel through a multi-step solvothermal process, followed by a final annealing step at 400 °C (referred to as 3D ZnCo₂O₄/GA) for use as the cathode material. As for the anode, they prepared a composite using ZIF-8 and the graphene hydrogel (referred to as 3D N-AC/GA) through a solvent process, followed by heat treatment at 800 °C in an Ar gas atmosphere, and finally activated the composite with a KOH aqueous solution. The schematic of the materials synthesis process is shown in Figure 12.

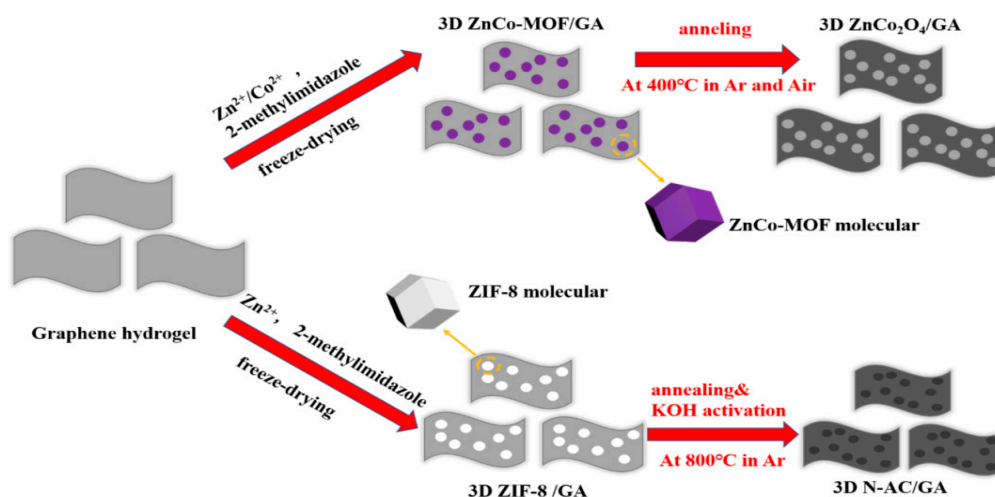


Figure 12. Synthesis process schematic of 3D ZnCo₂O₄/GA and 3D N-AC/GA materials by Xiao et al. [61] (image used with permission from Elsevier).

Cui et al. developed a ‘bimetallic cobalt–zinc sulfide nanostructure integrated with an rGO’ porous composite for a supercapacitor application, referred to as rGO/Zn_{0.773}Co_{0.227}S, using a GO/ZIF-8 template [62]. The synthesis process involved several steps. Initially, GO/ZIF-8 was created through a solvent process. Subsequently, a bimetallic composite was formed by chemically reacting GO/ZIF-8 with cobalt nitrate salt. This composite was then subjected to a calcination process at 400 °C for 2 h, followed by vulcanization (heat treatment with sulfur) by adding an NaS₂ solution and maintaining it at 150 °C for 8 h. The resulting product exhibited granular particles integrated into the rGO sheet, as illustrated in Figure 13a,b.

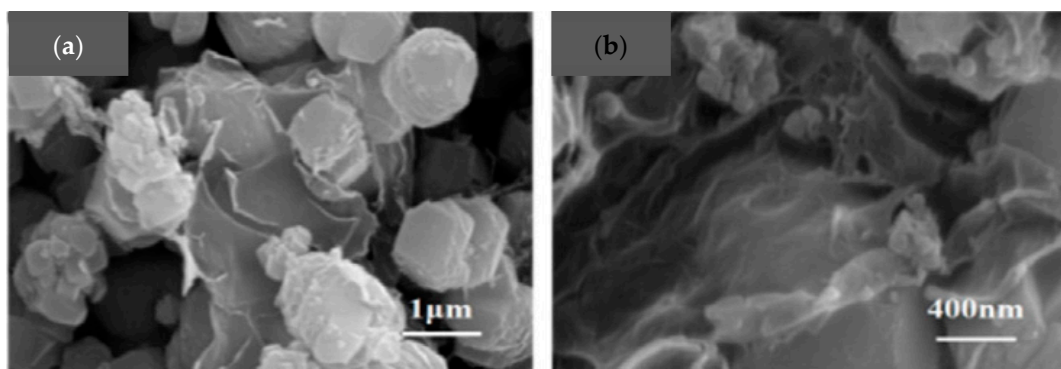


Figure 13. SEM image of the rGO/Zn_{0.773}Co_{0.227}S composite synthesized by Cui et al. at different magnifications: (a) with 1 μm scale bar, and (b) with 400 nm scale bar [62] (images used with permission from Elsevier).

The XPS survey scan revealed the presence of Zn, Co, S, O, and C elements, but nitrogen's presence was not explicitly mentioned, although a small peak in the range of 390–400 eV was observed. A detailed analysis of the Co 2p, Zn 2p, and S 2p narrow scan spectra indicated the different valence states of these elements. The authors suggested that the various valence states of these elements could have contributed to the capacitive performance of the rGO/Zn_{0.773}Co_{0.227}S composite.

In a recent investigation, Liu et al. synthesized a composite material by employing a solvent-based method to combine ZIF-8, CNT, and rGO, followed by a carbonization step at 950 °C [63]. The resulting composite exhibited a porous 3D structure, benefiting from the unique characteristics of ZIF-8, CNT, and rGO. The main elements identified in the material were carbon, nitrogen, and oxygen. The N 1S XPS spectrum analysis revealed the presence of various nitrogen configurations, namely pyridinic-N, pyrrolic-N, graphitic-N, and oxidized-N. The composite was technically hydrophilic as the static water contact angle was 83°.

The above-reviewed N-G/ZIF-8-based/derived materials for attaining higher capacitance values share the same fundamental principle of a pseudocapacitance as the electrode materials for electrochemical battery systems discussed in the previous section. Nonetheless, it was generally realized that the elaborated objectives of developing the same kind of composites for two different applications differed in some points. On the one hand, the primary goal of developing N-G/ZIF-8-based/derived materials for capacitors was to attain a higher rate of reversible electrochemical reactions to store energy quickly and in a higher quantity (related to higher power and energy densities). For this reason, these materials are often co-doped with other elements to promote electrochemical activities. On the other hand, when N-G/ZIF-8-based/derived materials are developed as electrodes for batteries, in addition to promoting more electrochemical reactions, delicate care is given to their structural aspects, such as the materials' ability to sustain the mechanical stress generated by volume expansion, chemical structural integrity, and stability over a long period of operation.

3.2. Performance and Functionalities of N-G/ZIF-8-Based/Derived Electrode Materials for Electrochemical Capacitors

This subsection mainly focuses on reviewing the capacitance performances of the N-G/ZIF-8-based/derived materials discussed above. For the electrochemical evaluation, virtually in all the studies, a common set of experiments were conducted. Generally, this started with CV measurements to understand the materials' basic capacitive characteristics. Different peaks in the CV plot in both the cathodic and anodic sweeps indicated reversible electrochemical reactions. The area under the CV plot also provided a measure of the capacitance. Then, the specific capacitance of the samples was measured at different voltages and current densities to understand the performances at different operational conditions. The measurements also included a cyclic stability test by recoding the capacitance of the materials for a number of cycles at a specific current density; this also provided an estimation of the materials' capacitance retention capabilities. Later in this subsection, the key findings on the capacitance performances of the N-G/ZIF-8-based/derived materials are discussed.

Chaikittisilp et al. evaluated the capacitance values of their nanoporous carbon materials; CV tests were conducted on a 0.5 M H₂SO₄ aqueous electrolyte [57]. The rectangular CV curve indicated the material's behavior as a supercapacitor, and redox peaks were also observed, indicating the extent of pseudocapacitive properties. Notably, the sample carbonized at 900 °C (denoted as Z-900) exhibited a gravimetric capacitance of 214 F/g at a 5 mV/s scan rate.

The high-temperature carbonization of ZIF-8 will likely follow a similar process to the pyrolysis of heavy hydrocarbons, like polymers. This involves breaking bonds, re-arranging molecules, polymerization, aromatic condensation, and removing different elements [115–117]. Since ZIF-8 contains a significant amount of nitrogen, direct carbonization is likely to create a material with properties resembling both N-doped graphene (in

structure and function) and zeolites (in morphology and crystallinity). The embedded nitrogen groups can serve as active sites to generate capacitive properties. Further research can analyze the capacitive properties of this carbonized ZIF-8 material and relate them to the different nitrogen functional groups present.

As shown by Li et al., in comparison to separately carbonized 3D graphene and ZIF-8 samples, the composite material obtained by carbonizing ZIF-8 embedded within 3D graphene (C-GZ) exhibited superior capacitive behavior [58]. The C-GZ sample showed higher charge storage results and better reversibility during the discharge process. The specific capacitances at different current densities were also improved for C-GZ compared to the other samples, as shown in Figure 14a. This material also demonstrated a good capacity retention (84%) with current densities ranging from 0.1 to 50 A/g and a coulombic efficiency of 90.3% after 3000 cycles, as shown in Figure 14b. Additionally, the researchers found that increasing the ZIF-8 content in the 3D graphene further enhanced the capacitive properties of the material. The improved supercapacitance of the carbonized ZIF-8/3D graphene composite was attributed to the combination of its larger surface area and increased mesoporous networks.

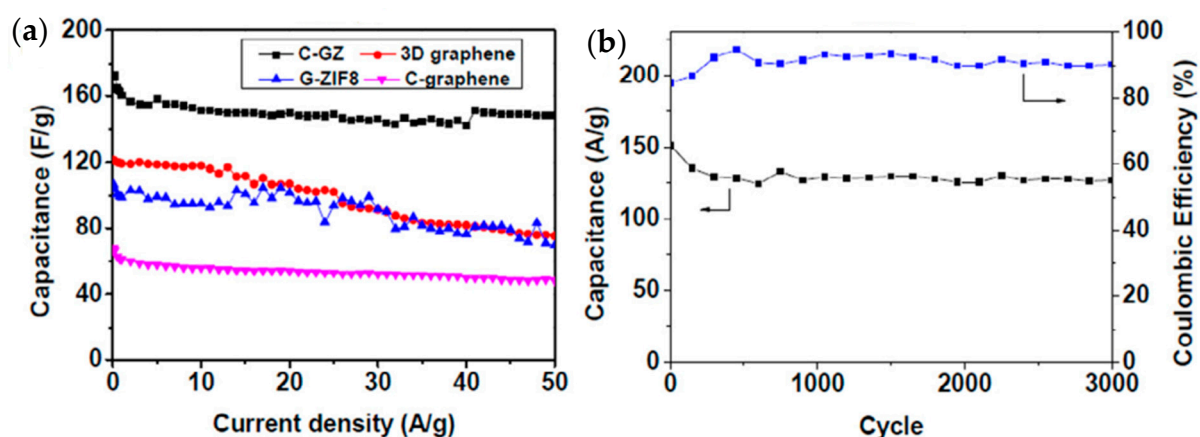


Figure 14. (a) Plots of specific capacitances of 3D graphene, C-graphene, G-ZIF8, and C-GZ samples measured at different current densities. (b) Cyclic performance stability and coulombic efficiency measurements of C-GZ sample over 3000 cycles at 5 A/g. Data obtained by Li et al. [58] (image used with permission from Elsevier).

In general, it was perceived that sub-nanometer pores facilitated enhanced ion electro-sorption and desorption processes, consequently elevating the capacitance per surface unit. This effect was particularly pronounced when the pore dimensions aligned with the ion sizes, promoting efficient surface area accessibility. This, in turn, augmented the electrochemically active surface area dedicated to charge storage [118–120]. From this perspective, it can be understood that, within the synthesis process of the G-ZIF-8 composite, the incorporation of additional ZIF-8 followed by carbonization introduces a greater number of pores with dimensions that align with the ions in the electrolyte. As a result, this contributes to an improved capacitance. It should be noted here that the crystal unit dimensions of ZIF-8 range between 11.6 to 16.99 Å, which are interconnected by narrow apertures measuring approximately 3.4 Å [33,121]. Due to the amalgamation of these structural characteristics, the material's capacity for capacitive performance could have been enhanced. Nonetheless, there is the potential for future research to delve into the precise function of the nitrogen sites embedded into this material and their impacts on the composite material's capacitive characteristics.

Wang et al.'s NCG sample synthesized at 800 °C (NCGs-800) exhibited the most significant area increment in the cyclic voltammetry (CV) curve compared to their other samples, as shown in Figure 15a. The specific capacitance was measured as 225 F/g at a current density of 0.5 A/g [59]. The galvanostatic charge/discharge curves showed almost

isosceles triangle-like shapes, indicating the favorable electrical charge storage properties of the sample. Remarkably, NCGs-800 demonstrated high electrochemical stability, retaining a coulomb efficiency of 96.8% even after 10,000 cycles, as presented in Figure 15b. In the electrochemical impedance spectroscopy (EIS) measurements, the NCGs-800 sample displayed a small real-axis intercept in the high-frequency region, indicating improved electrical conductivity compared to the carbonized ZIF-8 sample. The authors attributed the enhanced capacitive performance of NCGs-800 to the synergistic effect of the porous sandwich-like structure formed by integrating ZIF-8 and GO, along with the beneficial influence of nitrogen doping in the material. It is worth mentioning that electrode materials for electrochemical capacitors frequently adopt sandwich-like composites of various components. This configuration not only enhances the ionic and electronic conductivity properties, but also ensures structural integrity [122–126].

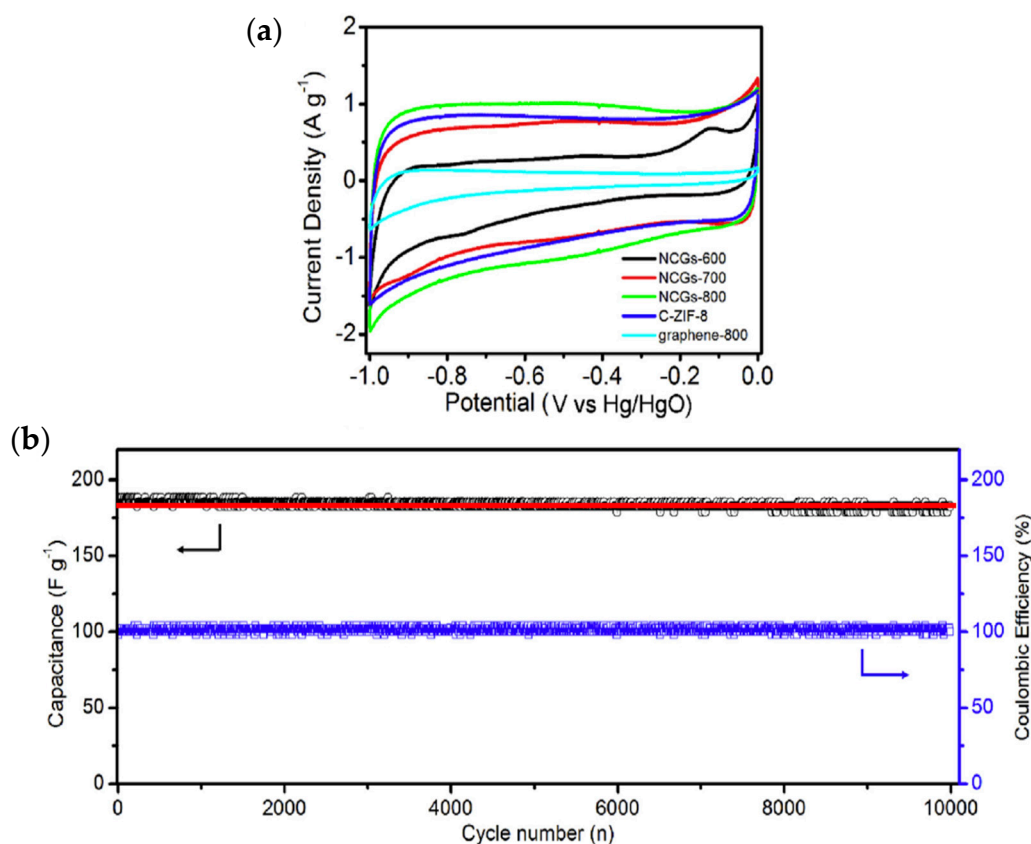


Figure 15. (a) CV curves of Wang et al.'s NCGs-600, NCGs-700, NCGs-800, C-ZIF-8, and graphene-800 samples obtained at a scan rate of 5 m/V [59]. (b) Cyclic performance and coulombic efficiency of NCGs-800 sample over 10,000 cycles measured at 4 A/g (images used with permission from Elsevier).

The sulfur-doped graphene oxide (SGZ) material of Khakpour et al. exhibited superior capacitive behavior in the 6M KOH electrolyte upon being analyzed by the cyclic voltammetry (CV), but its performance was less favorable in the 0.5 M H₂SO₄ electrolyte [60]. The specific capacitance of the SGZ composite was calculated to be 261 F/g at a current density of 1 A/g. To further understand the composite's properties, future investigations should be conducted to study the functionality of different chemical moieties present in the material.

Figure 16a shows the CV plots with the 3D ZnCo₂O₄/GA cathode, synthesized by Xiao et al., indicating the significant contribution of electrochemical redox reactions, resulting in high current densities [61]. The material exhibited a specific capacity of 241.1 mAh/g at 0.5 A/g, and the capacity retention was approximately 64.7% till 20 A/g, as shown in Figure 16b. The data show that the material possesses characteristics of both supercapacitors and batteries (pseudocapacitors). On the other hand, the 3D N-AC/GA composite

displayed near-rectangular CV curves as anodes, indicating typical supercapacitor behavior, presented in Figure 16c. This anode generated a capacity of 408.5 F/g at 0.5 A/g, and the capacity retention was about 56% at 20 A/g, as seen in Figure 16d.

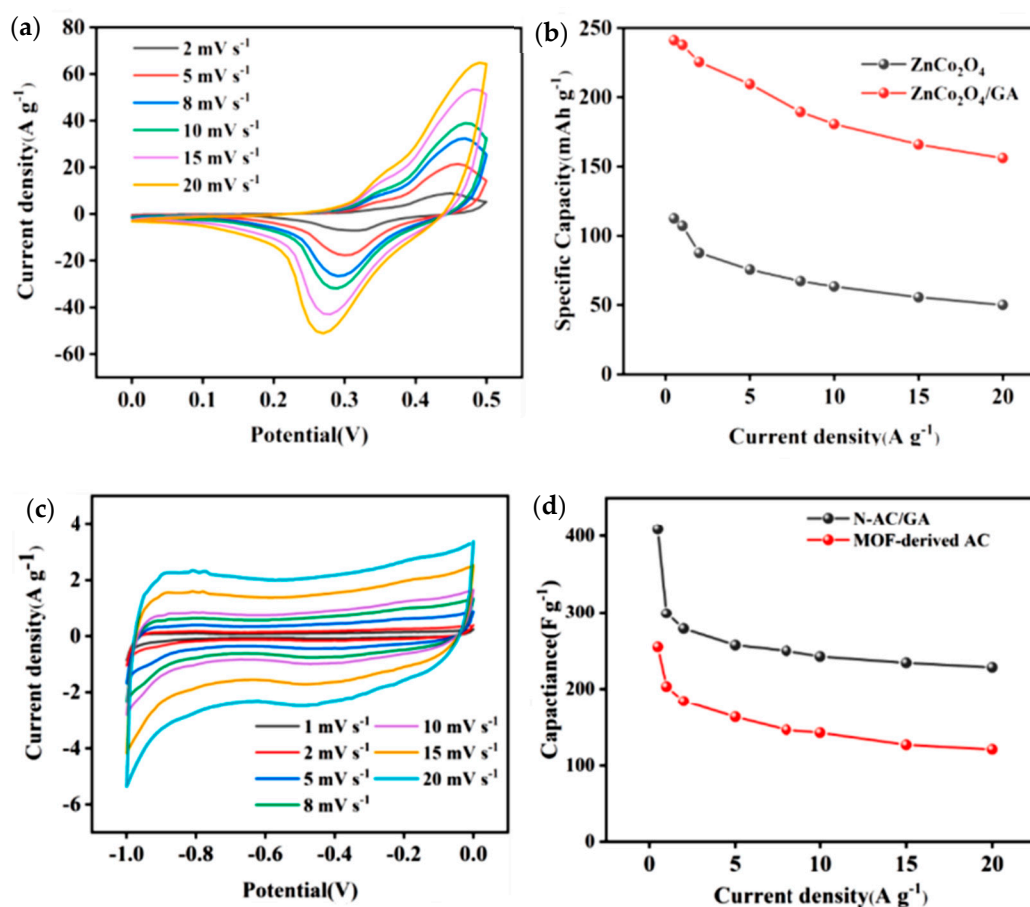


Figure 16. (a) CV curves measured with 3D $\text{ZnCo}_2\text{O}_4/\text{GA}$ cathode at different scan rates. (b) Specific capacities measured with $\text{ZnCo}_2\text{O}_4/\text{GA}$ cathode in comparison with Zn-Co MOF-derived ZnCo_2O_4 at various current densities. (c) CV curves measured with 3D N-AC/GA anode at different scan rates. (d) Gravimetric capacitance comparison between 3D N-AC/GA anode and MOF-derived AC measured at different current densities reported by Xiao et al. [61] (images used with permission from Elsevier).

Subsequently, Xiao et al. constructed a battery–supercapacitor hybrid device using 3D $\text{ZnCo}_2\text{O}_4/\text{GA}$ as the cathode and 3D N-AC/GA as the anode. The device exhibited a capacity of 187 F/g at 1 A/g and maintained 76.9% of its capacity under a current density of 10 A/g [61]. Moreover, it showed a ~100% coulombic efficiency over 10,000 cycles. The elemental composition of 3D $\text{ZnCo}_2\text{O}_4/\text{GA}$ primarily consisted of Zn, Co, O, and C, forming a structure with embedded ZnCo_2O_4 nanoparticles in a 3D graphene matrix. On the other hand, 3D N-AC/GA was mainly composed of C, N, and O, with a confirmed presence of pyridinic-N, pyrrolic-N, and quaternary-N groups. The superior capacitive performances of both materials and the hybrid device were mainly attributed to the 3D graphene framework, which enhanced the ion transfer efficiency and electronic conductivity.

Although Cui et al.'s bimetallic cobalt–zinc sulfide nanostructure integrated with rGO was intended to be a supercapacitor, the $\text{rGO}/\text{Zn}_{0.773}\text{Co}_{0.227}\text{S}$ samples surprisingly displayed well-defined redox peaks in their CV curves in Figure 17a, indicating a strong pseudocapacitance behavior [62]. The specific capacitance of the material reached a remarkable 1680 F/g at 1 A/g, shown in Figure 17b. However, it was not distinguished how much of this specific capacitance resulted from faradic activities. Over 5000 cycles at

10 A/g, the materials retained 78.8% of the specific capacitance, demonstrating good cycle stability. An asymmetric capacitor was prepared using this material in combination with activated carbon. The asymmetric capacitor exhibited a specific capacitance of 293.5 F/g at 1 A/g and retained 66.4% of the specific capacitance over 5000 cycles at 10 A/g. This study showcased the high pseudocapacitance behavior of the rGO/Zn_{0.773}Co_{0.227}S composite. However, further investigations are needed to understand the underlying mechanisms that lead to such exceptional characteristics in this material.

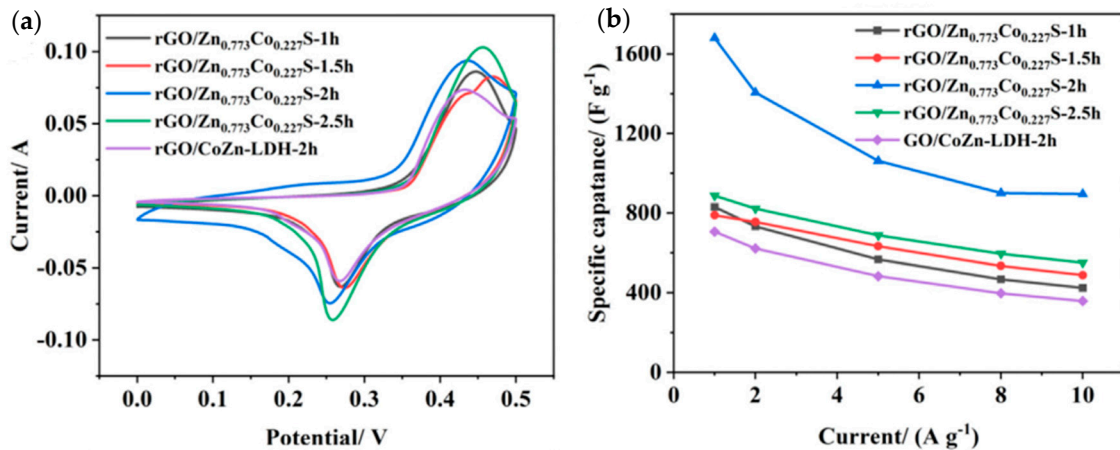


Figure 17. (a) CV curves of the rGO/Zn_{0.773}Co_{0.227}S samples with different synthesis times at 1 mV/s measured by Cui et al. [62]. (b) Specific capacitance plots of the rGO/Zn_{0.773}Co_{0.227}S-2h sample at various current densities (images used with permission from Elsevier).

In the CV and GCD measurements, Liu et al.'s integrated ZIF-8, CNT, and rGO composites demonstrated excellent supercapacitive behavior, with a specific capacitance of 423.8 F/g at a current density of 0.5 A/g [63]. The primary purpose of this composite material was water desalination using the capacitive deionization (CDI) approach. The composite's high electrical conductivity and abundant active sites contributed to its effective performance for water desalination.

Upon reviewing the N-G/ZIF-8-based/derived materials used to improve the electrochemical capacitance capability, an overview of the capacitive performances of the above-discussed materials is presented in Table 3.

Table 3. Overview of the capacitive performances of the N-G/ZIF-8-based/derived materials.

Material	Capacitive Performance (of the Best Sample)
Nanoporous carbon derived from ZIF-8 (Chaikittisilp et al.—2012 [57])	<ul style="list-style-type: none"> • Specific capacitance: 214 F/g at a 5 mV/s scan rate. • Did not show any confirmed capacitance loss after 250 cycles at a 50 mV/s scan rate.
ZIF-8 supported on 3D graphene (Li et al.—2014 [58])	<ul style="list-style-type: none"> • Specific capacitance: 238 F/g at a 1 A/g current density. • Capacitance retention: 86% from current density of 0.1 to 50 A/g. • Coulombic efficiency: ~93% (estimated from the plot) after 3000 charge–discharge cycles under a current density of 7 A/g.
ZIF-8 nanocrystal-derived N-doped carbon-decorated graphene sheets (Wang et al.—2018 [59])	<ul style="list-style-type: none"> • Specific capacitance: 225 F/g at a 0.5 A/g current density. • Capacitance retention: 80.4% retention from 0.5 to 20 A/g. • Coulombic efficiency: 96.8% after 10,000 charge–discharge cycles under a current density of 4 A/g.

Table 3. Cont.

Material	Capacitive Performance (of the Best Sample)
Sulfur-doped graphene oxide/ZIF-8 composite (Khakpour et al.—2022 [60])	<ul style="list-style-type: none"> • Specific capacitance: 298 F/g at a 0.5 A/g current density. • Capacitance retention: ~27% from current density of 0.5 to 8 A/g (specific capacitance reported at 80 F/g at a current density of 8 A/g). • Capacity retention: 102% after 1000 charge–discharge cycles (current density not specified).
3D ZnCo ₂ O ₄ /graphene aerogel (GA) (cathode); ZIF-8-derived N-doped active carbon/graphene aerogel (anode) (Xiao et al.—2022 [61])	<ul style="list-style-type: none"> • Three-dimensional ZnCo₂O₄/GA cathode: • Specific capacitance: 241.1 mAh/g at a 0.5 A/g current density. • Capacitance retention: 64.7% retention from a current density of 0.5 to 20 A/g. • Capacity retention: ~91% after 4000 charge–discharge cycles at a current density of 10 A/g. • ZIF-8-derived N-AC/GA anode: • Specific capacitance: 408.5 F/g (112.9 mAh/g) at a 0.5 A/g current density. • Capacitance retention: 56% retention from a current density of 0.5 to 20 A/g. • Capacity retention: ~86.6% after 4000 charge–discharge cycles at a current density of 10 A/g.
rGO/Zn _{0.773} Co _{0.227} S composite (Cui et al.—2022 [62])	<ul style="list-style-type: none"> • Specific capacitance: 1680 F/g at 1 A/g. • Capacitance retention: 53.3% from a current density of 1 A/g to 10 A/g. • Capacity retention: ~87.8% after 5000 charge–discharge cycles at a current density of 10 A/g.
ZIF-8, rGO, and CNT-derived N-doped porous carbon material; NPC/CNT-RG (Liu et al.—2023 [63])	<ul style="list-style-type: none"> • Specific capacitance: 412.5 F/g at a 1 A/g current density. • Capacitance retention: 76.2% from a current density of 0.5 A/g to 8 A/g.

Having similar characteristics as the electrode materials for electrochemical battery systems, the porosity of the materials for electrochemical capacitors is also a significant aspect to investigate. In Table 4, the pore diameters, pore volumes, and BET surface areas of the N-G/ZIF-8-based/derived materials are documented.

Table 4. Compiled data for the porosity parameters of the N-G/ZIF-8-based/derived materials as electrode materials of supercapacitors.

Material	Pore Diameter (nm)	Pore Volume (cm ³ /g)	BET Surface Area (m ² /g)
Nanoporous carbon derived from ZIF-8 (Chaikittisilp et al. [57])	1.02 to 1.17	0.57	1075
ZIF-8 supported on 3D graphene (Li et al. [58])	4	Not specified	352.8
ZIF-8 nanocrystal-derived N-doped carbon-decorated graphene sheets (Wang et al. [59])	Not specified	Not specified	816.4

Table 4. Cont.

Material	Pore Diameter (nm)	Pore Volume (cm ³ /g)	BET Surface Area (m ² /g)
Sulfur-doped graphene oxide/ZIF-8 composite (Khakpour et al. [60])	2.66	0.68	1030.4
Three-dimensional ZnCo ₂ O ₄ /graphene aerogel (GA) (cathode); ZIF-8-derived N-doped active carbon/graphene aerogel (anode) (Xiao et al. [61])	Cathode: ~8 Anode: ~3	0.20 0.12	90 156.82
rGO/Zn _{0.773} Co _{0.227} S composite (Cui et al. [62])	4 to 6	Not specified	32.58
ZIF-8, rGO, and CNT-derived N-doped porous carbon material; NPC/CNT-RG. (Liu et al. [63])	3.74 to ~26.54	Not specified	436.8

4. N-G/ZIF-8Based/Derived Materials as Electrocatalysts

Over the last two decades, researchers have been actively seeking alternatives to precious metal-based catalysts for promoting the crucial oxygen reduction reaction (ORR) in various electrochemical energy applications. Among the promising candidates are 2D graphene-type materials, which show potential due to their unique properties. However, despite the considerable progress, graphene-based catalysts have not yet achieved the same electrocatalytic performance level as their precious-metal counterparts, such as platinum group metals (PGMs). To address this challenge, a new approach has emerged—developing N-doped graphene-type materials derived from or integrated with ZIF-8. The rationale behind this concept lies in the structural advantages offered by ZIF-8; it possesses inherent micro- and mesopores, a large surface area, and a well-defined 3D crystal structure. When combined with N-Gs, these features create an optimized platform for enhancing the catalytic performance. In this section, a series of N-G/ZIF-8-based/derived materials developed as electrocatalysts is discussed. The first subsection focuses on the synthesis process and reported characteristics of the materials. In the second subsection, the electrocatalytic performances and fundamental reasons for such functionalities of the materials are thoroughly scrutinized.

4.1. Synthesis Trends and Characteristics of N-G/ZIF-8-Based/Derived Electrocatalysts

Aijaz et al. synthesized an N-decorated nanoporous carbon composite (denoted as NC) with a high surface area, using ZIF-8 as a template/precursor [77]. Furfuryl alcohol (FA) and ammonium hydroxide (NH₄OH) were utilized as secondary sources of carbon and nitrogen, respectively. The synthesis process involved a 12 h chemical mixing of the precursors, followed by FA polymerization at two different elevated temperatures and times (80 °C for 24 h and 150 °C for 7 h). Subsequently, the polymerized FA-NH₄OH-ZIF-8 composite underwent calcination at five different temperatures (ranging from 600 °C to 1000 °C) for 8 h, resulting in five different samples of the composite. The powder X-ray diffraction (PXRD) patterns and transmission electron microscopy (TEM) images of the samples revealed a combination of graphitic and zeolitic crystal structures, as depicted in Figure 18.

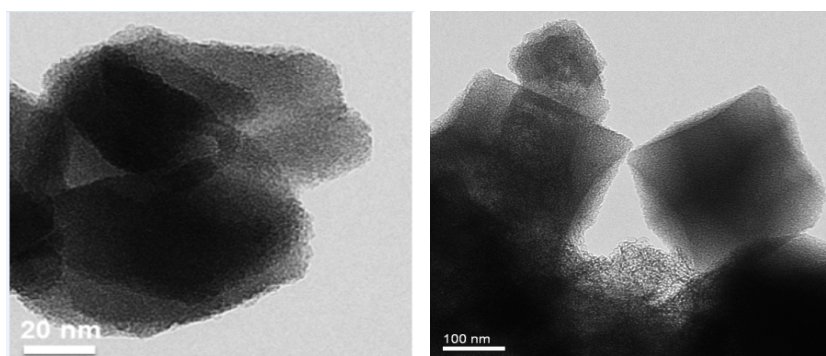


Figure 18. TEM images of N-decorated nanoporous carbon (NC) derived using ZIF-8 by Aijaz et al. [77] (images used with permission from the American Chemical Society).

It was suggested that by controlling the calcination temperature, surface area, porosity, and chemical composition (especially the nitrogen content) of the composite could be optimized, thus tuning its chemical and electrochemical properties. The composite samples were subjected to testing for their performances in CO₂ absorption capacity and electrocatalytic activity in the ORR. The data indicate that specific samples of this composite exhibit promising capabilities in both CO₂ uptake and ORR catalysis.

As presented by the authors, the remarkable CO₂ uptake capacity of this composite could be attributed to its high surface area and nitrogen content, which imparted a basic nature to the material. The analysis further revealed that the composite's surface with basic nitrogen sites interacted with CO₂ molecules during the absorption process. Moreover, the composite demonstrated a significantly higher selectivity for CO₂ absorption compared to nitrogen and methane (CH₄) gases. This high selectivity was attributed to possible local dipole–quadrupole interactions between the polarizable acidic CO₂ molecules and the basic nitrogen sites with a high charge density on the electron-rich graphene network.

Zhang et al. synthesized a metal-free nitrogen-doped graphitic porous carbon (denoted as NGPC) using ZIF-8 nanocrystals in a single-step high-temperature carbonization process conducted in a nitrogen gas-filled controlled environment at temperatures ranging from 700 to 1000 °C [78]. During this process, the zinc atoms were mostly delaminated from the composite. The microstructural analysis of the NGPC, carried out through techniques such as PXRD, Raman spectroscopy, and a nitrogen sorption measurement, verified the presence of a nanoporous structure and a high level of graphitization in the material. Remarkably, the NGPC retained the morphological features characteristic of ZIF-8, as evident from the scanning electron microscopy (SEM) and TEM images.

The material's XPS N 1s narrow spectra were analyzed, revealing the presence of various nitrogen functional groups in the material, including pyridinic-N, pyrrolic-N, graphitic-N, and pyridinic-N-oxide. The pyridinic-N group was found to be the dominant nitrogen component in all samples; but, with an increasing carbonization temperature, a gradual conversion of pyridinic-N to graphitic-N was observed. Their findings suggest a positive correlation between the proportion of pyridinic-N and graphitic-N and the improvement of the onset potential for ORR electrocatalysis in this material. These nitrogen functional groups likely played a role in facilitating electron transfer and O₂-absorption during ORR catalysis, with the graphitic-N group contributing more significantly than pyridinic-N.

Zhong et al. pointed out the challenges associated with the direct carbonization of ZIF-8 for N-doped porous carbon synthesis due to the potential damage to ZIF-8's crystal structure and resulting poor electronic conductivity [79]. Instead, they adopted an approach by anchoring ZIF-8 crystal units onto graphene oxide (GO) nanosheets prior to the carbonization step. To ensure homogeneous ZIF-8 growth on the GO, they chemically layered amide carbonyl groups of polyvinyl pyrrolidone (PVP) on GO sheets, as PVP was expected to better coordinate Zn ions for ZIF-8 nucleation on the GO's surface. The resulting

ZIF-8/GO sandwich-like material was then subjected to high-temperature calcination at three different temperatures (650, 800, and 950 °C) to create graphene-based nitrogen-doped porous carbon sheets (denoted as GNPCs). The authors mentioned that the successful synthesis of GNPCs required the application of both PVP and an excess of the 2-methylimidazole ligand (ZIF-8 precursor). During the high-temperature calcination process, the ZIF-8/GO sheets underwent shrinkage and attained a more graphitic morphology, as observed by the XRD and TEM analyses. The material exhibited a uniform distribution of nitrogen and carbon, as can be observed in the elemental mapping. The XPS N 1S spectra analysis revealed the presence of three nitrogen species: pyridinic-N, pyrrolic-N, and graphitic-N functional groups.

Thomas et al. successfully demonstrated a one-pot synthesis method to create an N-doped porous carbon composite by wrapping ZIF-8 with GO, followed by carbonization at 900 °C for potential ORR electrocatalysis [80]. They prepared three samples with varying ZIF-8 contents (30%, 50%, and 80% by weight)—labeled as GZ30C, GZ50C, and GZ80C, respectively. SEM and TEM imaging revealed a mixed morphology with hexagon-like structures formed by GO sheets encapsulating ZIF-8-like crystal units. It was presumed that the GO wrapping limited the loss of N content from the ZIF-8 during carbonization, and a higher ZIF-8 content led to reduced GO sheet agglomeration and improved material porosity. Refer to Figure 19 for the schematics of the GZ composite formation and TEM images.

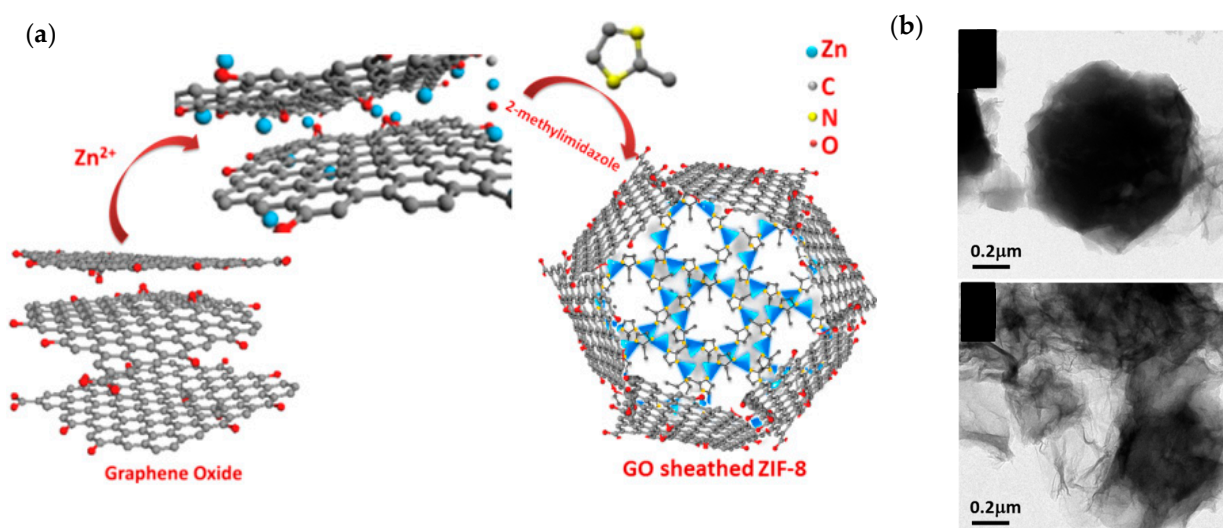


Figure 19. (a) Formation schematic and (b) TEM images of Thomas et al.'s GO-wrapped-ZIF-8 composite GZ80 (synthesized with 80 wt% of ZIF-8) [80] before (top) and after (bottom) carbonization (images used with permission from the American Chemical Society).

During the carbonization process, it was observed that the overall porosity (pore volume) of the material remained relatively unchanged. However, there was a significant transformation of the pore size, where a material initially dominated by micropores shifted to having 70% mesopores. This shift in pore structures was attributed to the delamination of Zn from the ZIF-8 framework and the destacking of GO during carbonization. The PXRD patterns of the synthesized materials exhibited two new peaks at diffraction angles of 25° and 42.2°, which were distinct from the characteristic peaks of both the GO and ZIF-8 precursors. These peaks were indicative of the presence of a form of graphitic carbon. The XPS N 1s spectra analysis revealed the existence of various nitrogen species, including pyridinic-N, pyrrolic-N, graphitic-N, and nitrate groups. The sample with the highest ZIF-8 content (GZ80C) exhibited relatively high ratios of graphitic-N (56%) and pyridinic-N (33%).

Liu et al. synthesized a sandwich-like composite of nitrogen-doped carbon (referred to as N-PC@G) by combining ZIF-8 and GO, and subsequently assessed its electrocatalytic capabilities for an oxygen reduction reaction (ORR) and oxygen evolution reaction (OER) [36]. ZIF-8 particles were formed on the GO surface through an in situ chemical synthesis process, employing varying amounts of GO (0.02, 0.05, and 1 g) to create different samples. These products were then subjected to pyrolysis at 900 °C for 5 h in a nitrogen atmosphere, effectively removing the Zn atoms through a subsequent acid wash. While the study of Wang et al. (in Section 3.1) also suggested the removal of Zn contentions through carbonizations, their XPS survey scan spectra indicated a probable peak for Zn atoms in the material at around 1021 eV, as seen in Figure 20a; nonetheless, the relative atomic ratio of this remaining Zn could be minute [59]. Here, Liu et al. suggested the removal of Zn with only the XRD spectra showing the absence of any peaks or perturbations from Zn impurities (Figure 20b). However, comparing these two studies, it can be presumed that Liu et al.'s process of Zn removal may be more effective as the Zn contents are more volatile at higher temperatures, as Liu et al. employed a carbonization temperature of 900 °C, which was higher than the other case (600–800 °C). In the TEM images, Liu et al.'s material exhibits a sandwich-like appearance, with ZIF-8-like nanocrystals covering both surfaces of distorted GO sheets. Figure 21 illustrates the schematic of their synthesis process and TEM images of PC@G-0.02 (produced with 0.02g GO). The best-performing sample, N-PC@G-0.02, contained a 4.42 at.% nitrogen content. In this nitrogen content, four nitrogen function groups, pyridinic-N (35.8%), pyrrolic-N (25.3%), graphitic-N (26.5%), and oxidized-N (12.4%), were found by XPS N 1s spectra analysis.

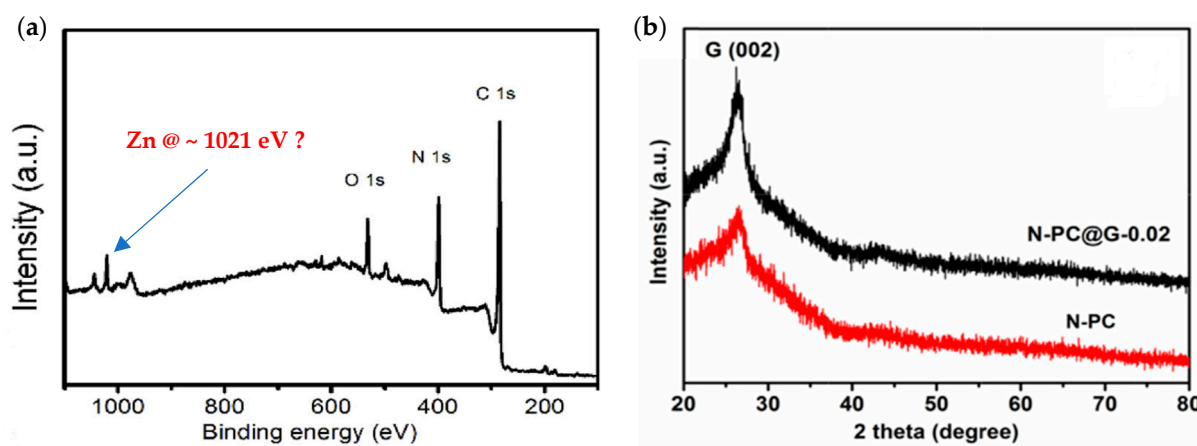


Figure 20. (a) XPS survey scan plot of prepared materials by Wang et al. [59]. (b) XRD spectra of synthesized materials by Liu et al. [36] (image used with permission from Elsevier).

Zhuang et al. successfully synthesized an electrocatalyst, denoted as N-G/MOF, by integrating nitrogen-doped graphene (N-G) with the metal-organic framework ZIF-8, for electrochemical ORR catalysis [39,68,127,128]. The N-G was first synthesized through a mechanochemical nanoscale high-energy wet (NHEW) ball milling process, using GO and melamine as carbon and nitrogen precursors, respectively [129]. Subsequently, the N-G was combined with ZIF-8 using the same ball milling process to create the N-G/MOF composite. Their studies demonstrated the viability of employing mechanochemical wet ball milling instead of the conventional high-temperature carbonization process for synthesizing N-G/ZIF-8-based/derived composites.

Cao et al. developed a nitrogen-doped hierarchically porous carbon composite derived from ZIF-8, using a double-solvent-mediated overgrowth process, referred to as CS-HPCNs [37]. In the synthesis, ZIF-8 nanocrystals were first chemically produced and then utilized as seeds for the subsequent step, where a ZIF-8 shell structure was formed around these seeds. This core-shell ZIF-8@ZIF-8 structure was then subjected to high-temperature treatment under an N₂ environment at different temperatures (900, 1000, and

1100 °C) and for various durations (5, 8, and 10 h). The resulting composite samples exhibited a graphitic morphology with a high degree of defects, as indicated by the I_D/I_G ratio from the Raman spectra. The XPS analysis confirmed the presence of nitrogen doping in the samples, and four nitrogen groups were identified: pyridinic-N, pyrrolic-N, graphitic-N, and oxidized-N. Figure 22 illustrates a schematic of the synthesis process, while an SEM image of the material is also provided.



Figure 21. (a) Schematic of synthesis process and (b) TEM images of N-PC@G-0.02 sample at different magnifications; synthesized by Liu et al. [36] (images used with permission from Elsevier).

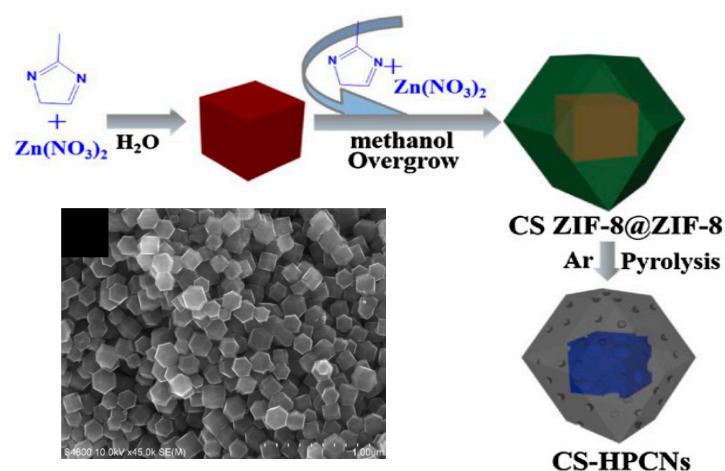


Figure 22. Synthesis process schematic and SEM image of CS-HPCN1000-5 sample produced by Cao et al. [37] (images used with permission from Elsevier).

Wei et al. introduced a synthesis approach to create a sandwich-like structure with ZIF-8 nanocrystals uniformly deposited and protected on GO sheets [38]. This deposition of ZIF-8 nanocrystals, which were about 20 nm in size, played a crucial role in preventing the agglomeration of GO sheets during the high-temperature treatment process at 800 °C. Through this synthesis, a composite material called N-doped nanoporous carbon/graphene nanosheets was obtained (referred to as Zn-ZIF/GO-800). The schematic of this process can be found in Figure 23. This composite demonstrated a remarkably high specific surface area and displayed an impressive electrocatalytic performance for the ORR in an alkaline medium. To further enhance the catalytic properties of this composite, cobalt was doped into the material. The cobalt-doped composite (referred to as Co-Zn-ZIF/GO-800) exhibited a superior ORR catalytic performance in an acidic medium, as indicated by the higher current density, enhanced stability, and increased tolerance to methanol.

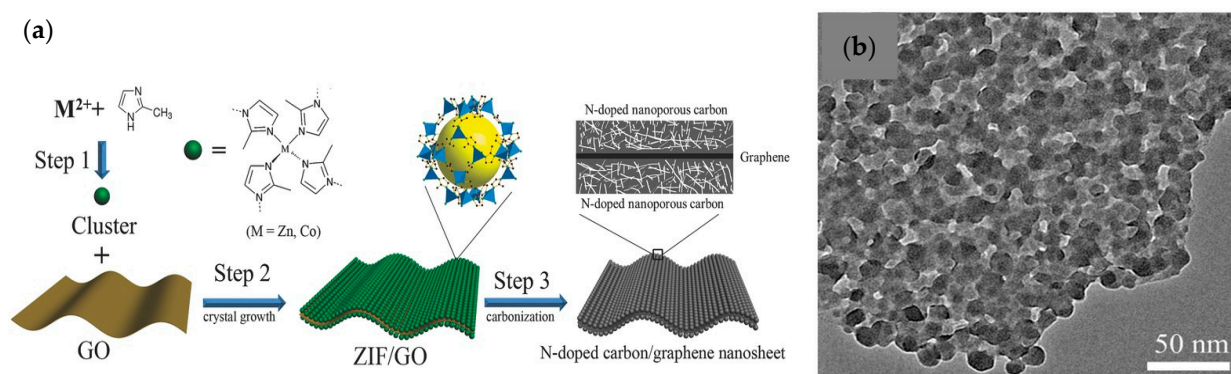


Figure 23. (a) Synthesis process schematic of N-doped nanoporous carbon/graphene nano-sandwiches (Zn-ZIF/GOs) produced by Wei et al. [38]. (b) TEM image of the Zn-ZIF/GO composite (images used with permission from John Wiley and Sons).

The Zn-ZIF/GO-800 composite exhibited several bonding configurations for nitrogen atoms, including pyridinic-N, pyrrolic-N, graphitic-N, and pyridinic-N⁺-O⁻. On the other hand, the Co-Zn-ZIF/GO-800 sample primarily consisted of pyridinic-N and graphitic-N groups. The presence of Co atoms or particles seemed to accelerate the formation of graphitic nitrogen, converting it from other nitrogen groups. The Co 2p spectra indicated the existence of Co-O and Co-N bonds, suggesting that nitrogen atoms possibly coordinated with Co atoms through CoN_x configurations on the carbon matrix.

Zhang et al. again highlight that ZIF-8-derived pyrolyzed catalysts with graphene-like carbon structures exhibit remarkable ORR electrocatalytic performances in alkaline environments, while their performances in acidic electrolytes are seldom reported [81]. The authors proposed that this disparity could be attributed to the pyrolysis process, where cracked or deformed ZIF-8 units tend to reassemble and encapsulate a significant number of active sites, resulting in fewer exposed active sites. To address this issue, they introduced carbon black (Ketjenblack EC600J or KJ600) along with a ZIF-8-derived Fe/N/carbon catalyst during the synthesis process.

Liu et al. developed a bifunctional catalyst capable of performing both the ORR and the OER by combining solvothermal and high-temperature pyrolysis techniques [82]. This catalyst was named yolk-shell Co-N-C@GNP, and it consisted of porous yolk-shell Co-N-C polyhedron nanocatalysts integrated with 3D macroporous graphene nanopockets. To achieve this, two zeolitic imidazolate frameworks, namely ZIF-8 and ZIF-67, were used as templates for creating the porous yolk-shell Co-N-C structure. ZIF-8 was employed as the yolk and ZIF-67 served as the shell component of the catalyst. The X-ray absorption spectroscopy (XAS) measurements confirmed the presence of Co-N₄ coordination moieties, which are known to create catalytically active sites. The elemental characterization results reveal the existence of various nitrogen functional groups in the material, including pyridinic-N, Co-N_x, graphitic-N, and oxidized-N.

4.2. Performance and Functionalities of N-G/ZIF-8-Based/Derived Electrocatalyst

In this section, the reported electrochemical performances of the N-G/ZIF-8-based/derived materials, discussed in the previous section, are scrutinized to achieve a clearer view of how these materials function as catalysts in different electrochemical environments. By incorporating ZIF-8 with N-Gs, the number of exposed catalytic active sites can be increased and the transport of reactants/products involved in ORR can be improved. This combination is believed to facilitate faster reaction kinetics and more efficient charge transfer processes. In this context, this section provides a critical review of the progress made in developing N-G/ZIF-8-based/derived electrocatalysts for ORR over the past decade. By meticulously analyzing the performances and functionalities, we could benchmark their capabilities and identify the key fundamental aspects that merit further investigation.

In terms of the electrocatalytic performance, the N-decorated nanoporous carbon (NC) composite samples, synthesized by Aijaz et al., were tested for ORR in an alkaline medium (0.1 M KOH) [77]. Notably, a specific sample calcinated at 900 °C exhibited an impressive ORR electrocatalytic performance, comparable to that of a benchmark 10 wt% Pt/C catalyst in terms of the ORR current density measured by cyclic voltammetry (CV). The high ORR catalytic activity of the composite was attributed to the presence of basic nitrogen sites on its surface, in combination with its high surface area and porosity, which facilitated an efficient mass transfer process for the ORR reactants.

In essence, this composite material showcased a blend of graphitic and zeolitic structural characteristics, featuring a high surface area, porosity, and surface decoration with basic nitrogen sites. These basic nitrogen sites played a vital role in facilitating interactions with CO₂ molecules during absorption and with ORR reactants during the electrocatalysis process, thereby resulting in the composite's high CO₂ uptake capacity and ORR catalytic activity. Interestingly, the nitrogen atoms in the composite formed different bonding orientations, such as pyrrolic-N, pyridinic-N, and graphitic/substitutional/quaternary-N (as presented in the Supporting Information file of Aijaz et al. [77]). Each of these nitrogen functional groups is known to contribute uniquely to the local electronic structures of graphene, particularly the graphitic-N sites that induce an n-type local electronic effect [18,130–132]. Hence, the graphitic-N functional groups could be the basic nitrogen sites postulated in this study that enhanced the ORR catalytic activities of this material. Nonetheless, the combination of graphitic and zeolitic features within this composite likely created other sites with unexplored electronic configurations that could be advantageous for ORR catalysis. Investigations should be conducted in the future to explore this possibility.

As per the report of Zhang et al., the catalytic performance of the metal-free nitrogen-doped graphitic porous carbon (NGPC) for ORR was assessed in a 0.1 M KOH electrolyte, and certain samples demonstrated ORR electrocatalytic activity comparable to that of a 20 wt% Pt/C catalyst [78]. The enhanced ORR catalytic limiting current density could be attributed to several factors, including the specific surface area, degree of graphitization, and abundance of active sites within the catalyst. These factors synergistically facilitated the improved mass transport of the ORR reactants/products and enhanced electrical conductivity. The utilization of ZIF-8 as a precursor/template for its structural advantages, along with the high-temperature graphitization process, contributed to the notable improvement in the ORR electrocatalytic activity of the NGPC material.

It is worth noting that the relationship between the nitrogen content and ORR catalytic activity, particularly the onset potential, did not appear to be directly proportional. This phenomenon was attributed to the additional valence electrons introduced by the doped nitrogen atoms, particularly in graphitic-N, which improved the material's overall conductivity. However, excessive nitrogen doping can lead to the localization of conducting electrons, potentially reducing the overall conductivity of the material.

The electrochemical characterization results also suggest that structural defects and oxygen-containing groups play a role in the ORR catalysis process. However, given the complexity of electrocatalytic ORR on such a heterogeneous carbon-based catalyst with a variety of functional groups, a clear and definitive understanding of the specific functionality of different sites for ORR catalysis remained challenging to achieve.

This study again revealed that utilizing ZIF-8 nanocrystals to create nitrogen-doped porous carbon nanomaterials led to improvements in ORR electrocatalysis. However, when analyzing the correlations between the electrocatalytic activity and the functionalities of different active sites in this material, similar trends to those observed in typical N-doped graphene materials in the literature were observed. The inherent electrocatalytic functionalities of this NGPC material could differ from typical 2D N-doped graphene due to structural and orientational differences and the yet unknown graphitization process of this material. Further investigations should be conducted in the future to understand the effects of the zeolite-like 3D structure and graphitization process on the localized electronic structures near the doped nitrogen sites.

Among the graphene-based nitrogen-doped porous carbon sheet (GNPCS) samples synthesized by Zhong et al., GNPCSs-800, obtained from calcination at 800 °C, demonstrated the best performance for ORR catalysis in a 0.1 M KOH electrolyte [79]. This sample contained higher proportions of pyridinic-N and graphitic-N, which were identified as key factors contributing to the enhanced ORR electrocatalysis. The study again emphasized that a higher nitrogen content alone did not guarantee a superior ORR catalytic performance in the material.

The study presented an intriguing method for synthesizing a composite material derived from ZIF-8 and GO, which showed potential for ORR electrocatalysis. Nonetheless, the comprehensive understanding of the fundamental functionalities of this N-doped porous carbon catalyst was limited, as it was briefly discussed in relation to the general functionality of pyridinic-N and graphitic-N for ORR catalysis.

The electrochemical characterization results obtained by CV analysis for the N-doped porous carbon composite produced by Thomas et al. reveal that their GZ80C sample exhibits the most improved onset potential for an oxygen reduction reaction (ORR) compared to the other two samples, GZ30C and GZ50C, although the latter ones had higher nitrogen contents [80]. The GZ80C sample demonstrated a competitive ORR onset potential (0.88 V vs. RHE) comparable to a standard 40 wt% Pt/C catalyst (1 V vs. RHE). The enhancement of electrocatalytic activity was attributed to a synergistic interplay between the nitrogen content, surface area, and pore characteristics. The higher number of active sites in GZ80C was deemed mainly responsible for the improvement in the ORR onset potential and limiting current density. The authors inferred that the asymmetric charge distribution resulting from the difference in electronegativity between N and C atoms facilitated better oxygen molecule adsorption, initiating the ORR process. They also suggested that an appropriate combination of graphitic-N and pyridinic-N functional groups could hold the key to achieving an improved onset potential and higher limiting current density for such ORR electrocatalysts. As shown in their XPS N 1s narrow scan in Figure 24, the relative contents of graphitic-N and pyridinic-N increases from the precursor to the synthesized GZ80C catalyst. However, the exact charge distribution within ZIF-8 and GO-derived N-doped porous carbon composites and the specific roles played by different nitrogen functional groups in this charge distribution remain unknown. This study suggests the possibility of an optimal quantitative ratio of nitrogen functional groups that can tailor the electronic structure (both overall and local) of the materials in a specific way, promoting maximum oxygen adsorption in electrochemical environments.

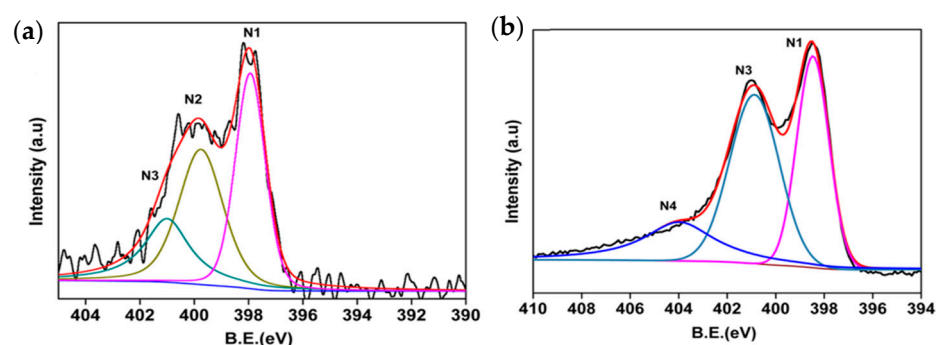


Figure 24. Reported by Thomas et al. [80]; XPS N 1s narrow scan spectra of (a) ZIF-8C and (b) GZ80C catalyst (N1 → pyridinic nitrogen, N2 → pyrrolic nitrogen, N3 → graphitic nitrogen, and N4 → nitrate species) (images used with permission from the American Chemical Society).

Liu et al.'s sandwich-like composites of nitrogen-doped carbon (N-PC@G) samples were tested for evaluating their electrocatalytic performances for ORR in an alkaline electrolyte (0.1 M KOH) [36]. The N-PC@G-0.02 sample displayed a more favorable onset potential and higher current densities compared to a commercial 20 wt% Pt/C catalyst, within the applied potential range of approximately 0.8 to 0.5 V vs. RHE, as seen in

Figure 25a. The electron transfer numbers (n), determined for this ORR electrocatalytic reaction, remained very close to the ideal n for ORR ($n = 4$), as presented in Figure 25b. The chronoamperometric responses of the material sample in comparison with a standard Pt/C catalyst was recorded as well, as shown in Figure 25c. These data clearly indicate the better catalytic activity (in terms of the relative current generation) retention of the N-PC@G-0.02 sample over a 20,000 s time period compared to the Pt/C catalyst. Additionally, the material exhibited competitive OER catalytic performances in comparison to a conventional RuO₂ catalyst for OER.

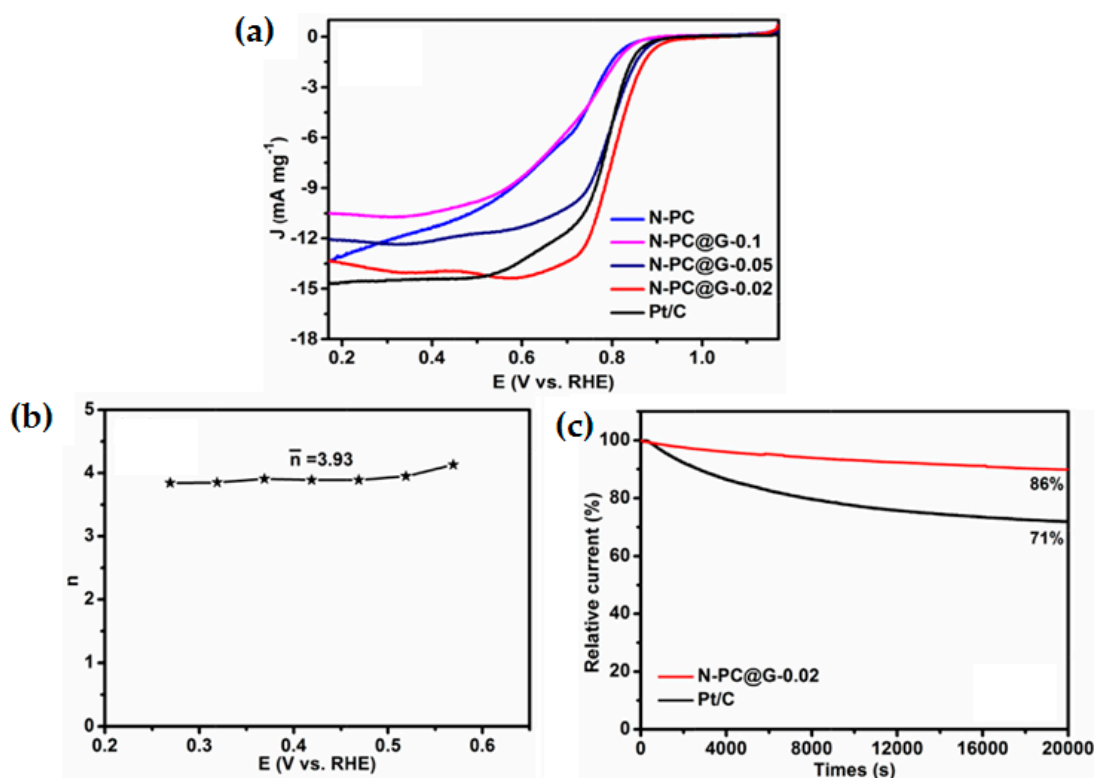


Figure 25. (a) ORR electrocatalytic performance measurements in terms of electron transfer number (n) at different applied potential (E) for the ZIF-8-derived N-PC@G samples synthesized by Liu et al. [36] in comparison with a 20 wt% Pt/C catalyst; LSV data were obtained from the O₂-saturated 0.1 M KOH solution at a scan rate of 10 mV/s and a rotating rate of 1600 rpm. (b) The electron transfer numbers calculated for the N-PC@G-0.02 sample within a specific potential range. (c) The N-PC@G-0.02 sample's chronoamperometric responses compared to the Pt/C catalysts at 0.62 V in the O₂-saturated 0.1 M KOH medium measured at 1600 rpm (images used with permission from Elsevier).

The authors suggested that the presence of a nitrogen content, particularly in the form of pyridinic-N and graphitic-N groups, as seen in Figure 26a, along with advantageous structural features, such as a high surface area, porosity (Figure 26b), and distorted surface morphology, contributed to the composite's electrocatalytic properties for both ORR and OER. However, it is essential to note that electrocatalytic ORR and OER reactions differ fundamentally in terms of the reactants, reaction mechanisms, energy thresholds for initiation, and other factors. While the structural features of the composite could benefit both catalytic reactions, it remained unclear if the active sites responsible for each reaction were the same, and how these probable active sites function. Further investigations are required to gain a better understanding of the identities and functionalities of the active sites in such dual-functioning electrocatalysts.

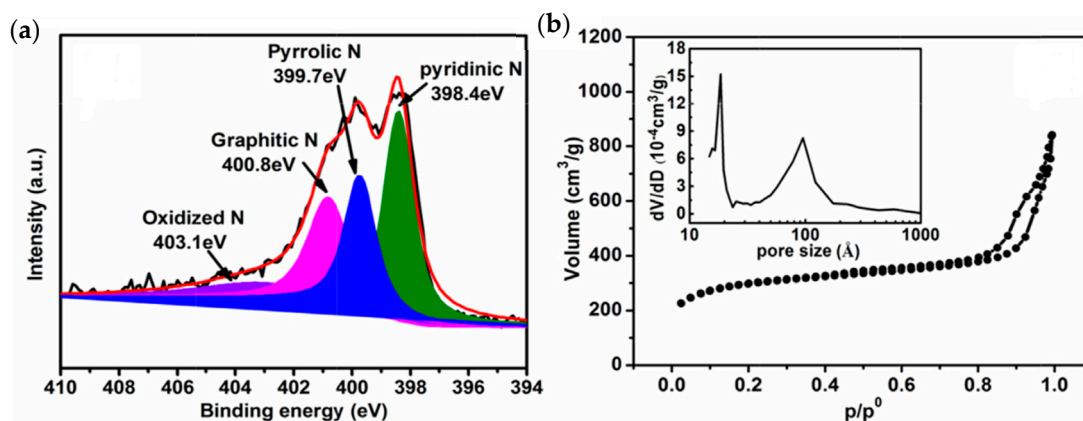


Figure 26. (a) XPS N 1s analysis of the N-PC@G-0.02 sample of Liu et al. [36]. (b) Measurements of pore volume and pore size (inset) of the N-PC@G-0.02 sample materials (images used with permission from Elsevier).

Among the different samples produced by Zhuang et al. with the variation of the ball milling time and speed, the N-G/MOF composite obtained after 16 h of milling with a 350 rpm speed showed the best ORR catalytic performance in a 0.1 M KOH electrolyte [39,68,127,128]. It exhibited a higher ORR current density compared to a 10 wt% Pt/C catalyst, as measured in an RRDE system under the same conditions. The XPS analysis revealed a notable 20.2% atomic percentage of doped nitrogen in this specific sample. This unusually high nitrogen content was attributed to the use of a solid nitrogen precursor: melamine. Further analysis showed that pyridinic-N was the dominant nitrogen functional group, accounting for 71% of the material's nitrogen content.

Based on the provided results presented by Cao et al. for the nitrogen-doped hierarchically porous carbon composite samples, the CS-HPCN1000-5 samples, obtained through the carbonization of ZIF-8@ZIF-8 at 1000 °C for 5 h, demonstrate a higher ORR limiting current density in an alkaline medium (0.1 M KOH) compared to a benchmark 20 wt% Pt/C catalyst, as shown in Figure 27a [37]. The long-term performance stability of the CS-HPCN1000-5 sample was determined by obtaining chronoamperometric responses in comparison to a standard 20 wt% Pt/C catalyst, as seen in Figure 27b. The CS-HPCN1000-5 sample retained around 87% of the relative current over a 12,000 s time period, which was considerably higher than the Pt/C for the sample's same measurement time in the same condition. However, all the samples exhibited slightly lower onset potentials than the Pt/C catalyst. The data suggest that the ORR catalytic current density of the samples show a positive correlation with the relative ratios of pyridinic-N and graphitic-N functional groups, rather than with the total nitrogen doping ratio. The highest current density was achieved by the sample with the highest ratio of graphitic-N and the lowest ratio of pyrrolic-N, as seen in Figure 28. Conversely, the pyrrolic-N content seemed to have a negative impact on the catalytic current density. The results also indicate that the sample with the highest pyridinic-N content achieves the best onset potential. The authors proposed that the pyridinic-N functional group enhanced the electron-donating capability of the carbon matrix. In addition to the nitrogen content, the larger pore volume and higher surface area were found to be beneficial for the ORR catalytic activities of the samples.

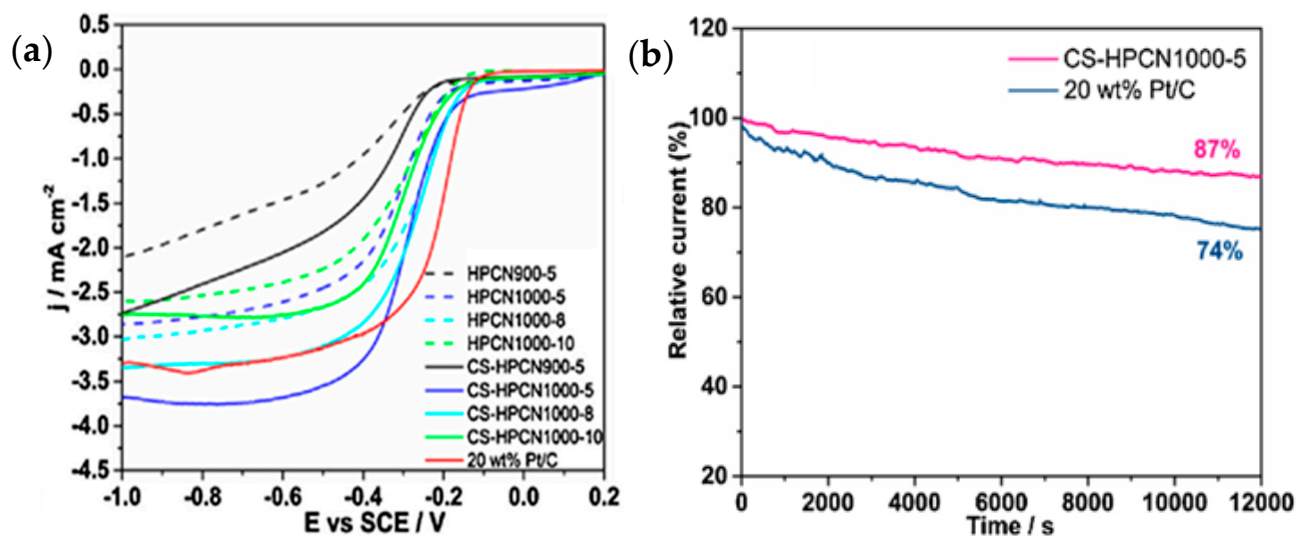


Figure 27. (a) ORR electrocatalytic performance measurements for nitrogen-doped hierarchically porous carbon composite samples synthesized by Cao et al. in comparison with a 20 wt% Pt/C catalyst [37]; LSV data are obtained from the O₂-saturated 0.1 M KOH solution at a scan rate of 10 mV/s and a rotating rate of 1600 rpm. (b) Chronoamperometric responses of the CS-HPCN1000-5 sample in comparison with 20 wt% Pt/C with a rotating speed of 1600 rpm at -0.3 V in O₂-saturated KOH medium (images used with permission from Elsevier).

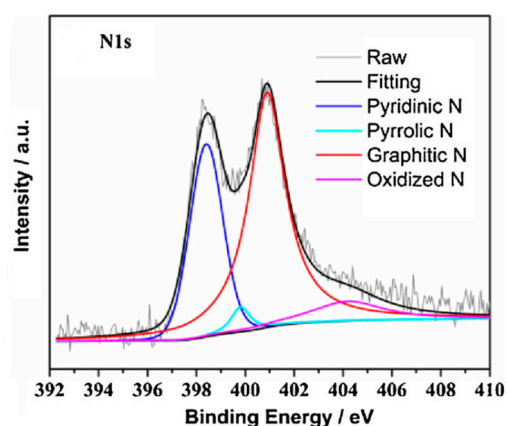


Figure 28. XPS N 1s spectra analysis of CS-HPCN1000-5 catalyst prepared by Cao et al. [37] (images used with permission from Elsevier).

According to the data presented by Wei et al. for the N-doped nanoporous carbon/graphene nanosheet samples, both Zn-ZIF/GO-800 and Co-Zn-ZIF/GO-800 demonstrate impressive ORR catalytic performances in an alkaline medium, comparable to a commercial 20 wt% Pt/C catalyst, as depicted in Figure 29a [38]. They also measured the chronoamperometric responses of the samples with a comparison of the standard Pt/C catalyst shown in Figure 29b to determine the materials' long-term performance stability. Both Zn-ZIF/GO-800 and Co-Zn-ZIF/GO-800 samples retained a higher related current at a 10,800 s (180 min) time period than the Pt/C in the same environment; the data demonstrate that the Co-Zn-ZIF/GO-800 sample has the best performance stability within this time period. The authors showed that the presence of active sites, like pyridinic-N, graphitic-N, Co-O, and Co-N, along with a high surface area and porosity, contributed to the improved catalytic activities. In an acidic medium, the Co-Zn-ZIF/GO-800 composite showed a lower, but comparable, ORR electrocatalytic performance to Pt/C. The Co-N moiety was suggested to play a vital role in the ORR catalysis in the acidic medium, although further details of this aspect were not found in the study.

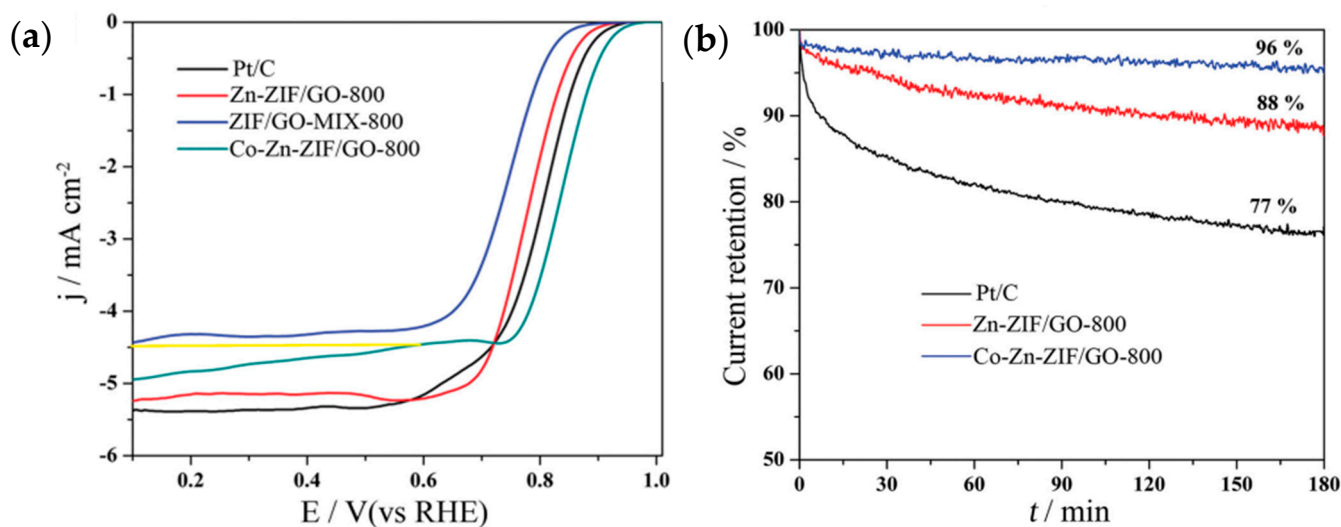


Figure 29. (a) ORR electrocatalytic performance measurements for Zn-ZIF/GO and Co-Zn-ZIF/GO synthesized by Wei et al. in comparison with a 20 wt% Pt/C catalyst; LSV data were obtained from an O₂-saturated 0.1 M KOH solution at a scan rate of 10 mV/s and a rotating rate of 1600 rpm. (b) Chronoamperometric response of Zn-ZIF/GO-800 in comparison with Co-Zn-ZIF/GO-800 and Pt/C at 0.78 V at a 1600 rpm rotational speed in the O₂-saturated 0.1 M KOH electrolyte [38] (images used with permission from John Wiley and Sons).

However, this research provided a significant advancement in graphene-ZIF-8-based composite electrocatalysts. The inclusion of metal co-doping in these composites proved to be beneficial for ORR catalysis in the acidic medium. Previous studies mainly focused on showcasing electrocatalytic performances in alkaline mediums for such materials. It remains uncertain whether these materials can perform well in acidic mediums without the co-doping of other metals. Future studies should be conducted to explore this aspect and seek ways to enhance the performances of such composites in acidic mediums without the need for metal co-doping.

According to Zhang et al.'s experimental findings, the inclusion of KJ600 facilitated a higher number of exposed active sites by preventing the reassembling of pyrolyzed ZIF-8 [81]. Additionally, it helped to mitigate the agglomeration of Fe particles, leading to a more dispersed distribution of Fe sites and an increased density of exposed active sites in the material. As depicted in Figure 30, the incorporation of KJ600 with Fe/N/Carbon significantly improves the electrocatalytic performance of the composite. Nonetheless, it should be noted that this composite also contained Fe particles as co-doped elements, which assisted the catalytic activity. In Figure 30b, the determined electron transfer number and hydrogen peroxide (H₂O₂) yield from the materials during ORR are presented. Compared to the Fe/N/carbon, the KJ-Fe/N/carbon sample produced a higher electron transfer number closer to 4 and a lower yield of H₂O₂ with the applied potential range. In the ORR process, the H₂O₂ biproduct produced through two electron transfer reactions is known to have a detrimental effect on the catalyst materials [133]. Hence, a lower H₂O₂ yield from the KJ-Fe/N/carbon sample concomitantly indicated better material stability and catalytic performance results.

As Liu et al. evaluated the electrocatalytic performance of their yolk-shell Co-N-C@GNP materials, the data indicated that the catalyst exhibited competitive oxygen reduction reaction (ORR) electrocatalytic activity in an alkaline medium, comparable to the performance of a 20 wt% Pt/C catalyst [82]. Furthermore, the catalyst demonstrated a reasonable electrocatalytic performance for an oxygen evolution reaction (OER) in the alkaline medium, although it was lower than that of the conventional OER catalyst RuO₂. When employed as the anode catalyst in a Zn-air battery (ZAB) and a quasi-solid-state

ZAB battery, the catalyst showed promising results with a high open circuit voltage (1.6 and 1.4 V, respectively), peak power density, and good cycling stability.

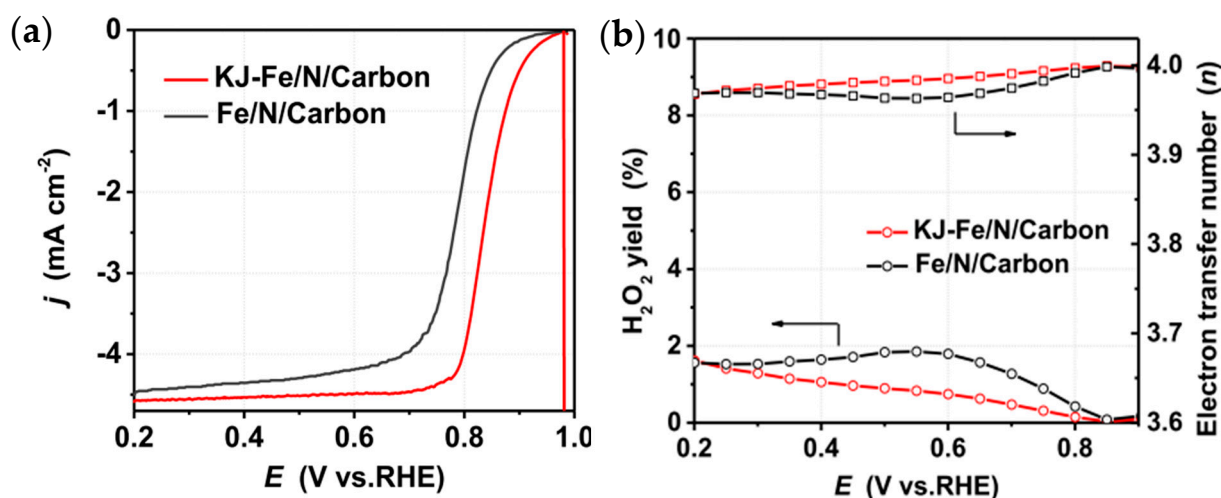


Figure 30. (a) ORR electrocatalytic performance comparison of KJ-Fe/N/carbon and Fe/N/carbon synthesized by Zhang et al. [81]; LSV data were obtained from an O₂-saturated 0.1 M KOH solution at a scan rate of 10 mV/s and a rotating rate of 900 rpm. (b) Measurements of the electron transfer number (*n*) and the corresponding H₂O₂ yield within an applied potential region range of 0.2–0.9 V for KJ-Fe/N/carbon and Fe/N/carbon samples (images used with permission from the American Chemical Society).

Based on the electrocatalytic performances, the authors explained that the hierarchical porous configuration of the yolk–shell Co-N-C@GNP catalyst facilitated the exposure and accessibility of Co-N₄ active sites, as well as improved mass transportation. The hollow yolk–shell structure effectively maintained the structural stability of ZIFs, preventing their agglomeration and leaching, while also protecting Co nanoparticles from rapid oxidation. The presence of graphene ‘nanopockets’ contributed to the dispersion of yolk–shell Co-N-C nanocrystals, enhancing the electrical conductivity and electron transfer rate. The nitrogen functional groups, specifically pyridinic-N and graphitic-N, within the materials were observed to play a crucial role in improving the ORR onset potentials and limiting the current density.

In situ Raman spectroscopy measurements were used to gain insights into the ORR and OER mechanisms of the catalyst. The data suggest that OH[−] ions are adsorbed on Co sites, forming Co²⁺–OH[−], and as the ORR process proceeds, the Co sites further oxidize to form Co³⁺–O and CoOO[−]. For the OER process, Co²⁺–OH and Co³⁺–O gradually reduce to form Co–Co bonds. This study emphasized the significance of Co-N₄ sites for ORR and OER electrocatalysis, while specific details about the involvement of other nitrogen functional groups in ORR or OER electrocatalysis were not extensively explored.

In addition to the materials reviewed above, other studies were found to integrate different non-metallic elements, such as sulfur (S) and phosphorus (P), in ZIF-8-derived N-doped graphene materials [134–139]. Son et al. synthesized a nitrogen and sulfur co-doped porous carbon (NSDPC) composite using ZIF-8 and thiourea as precursors (at different weight ratios) as an electrocatalyst for ORR [134]. The final product was obtained by carbonizing the ZIF-8 and thiourea mixture at 900 °C for 5 h at a heating rate of 5 °C/min. Their best sample, NSDPC-3 (with ZIF-8:thiourea = 3:1), produced a higher ORR current density of around 6 mA/cm² in a 0.1 M KOH electrolyte at ~0.2–0.35 V (vs. RHE) in the CV measurement, which was higher than a commercial Pt/C electrode. Rong et al. produced an N, P, and S tri-doped mesoporous carbon (denoted as NPSpC) from ZIF-8 to enhance ORR electrocatalysis in universal pH conditions [135]. The material was found to perform very similarly to a commercial Pt/C catalyst in a 0.1 M KOH electrolyte and reasonably

well in a 0.5 M H₂SO₄ electrolyte, in terms of the ORR current density, onset potential, and half-wave potential. In a similar trend, Jahromi et al. synthesized an N-doped rGO-based cobalt-ZIF-8 electrocatalyst for ORR [136]. In several other cases, ZIF-8-derived N-doped porous carbon materials were synthesized as support materials for the Pt/C catalyst to reduce the load of platinum [137–139].

After conducting a thorough review of the N-G/ZIF-8-based materials synthesized for ORR electrocatalysis in the past decade, we compiled the findings in Table 5 to offer a comprehensive overview of these materials. In addition to providing information about the materials' precursors and synthesis methods, we also included details of the reported ORR electrocatalytic performances, all measured using consistent units and scales.

Table 5. An overview of the N-G/ZIF-8-based/derived materials as electrocatalysts.

Materials	Precursors	Synthesis Steps	ORR Catalytic Performance (of the Best Sample)
N-decorated nanoporous carbon (NC) (Aijaz et al.—2014 [77])	ZIF-8; furfuryl alcohol (FA); and ammonium hydroxide (NH ₄ OH).	Chemical mixing of ZIF-8 and FA. FA polymerization. High-temperature calcinated (between 600–1000 °C) under a stream of nitrogen gas.	Measured in O ₂ -saturated 0.1 M KOH. Catalyst loading: 33.95 µg/cm ² (2.4 µg catalyst on 3 mm diameter electrode surface). ORR onset potential 0.83 V vs. RHE. Current density of 4.9 mA/cm ² at 0.1 V vs. RHE (at 2500 rpm; scan rate: 10 mV/s).
Nitrogen-doped graphitic porous carbon (NGPC) (Zhang et al.—2014 [78])	ZIF-8 nanocrystals.	Single-step high-temperature carbonization of ZIF-8 (between 600–1000 °C)—in a nitrogen-filled environment.	Measured in O ₂ -saturated 0.1 M KOH. Catalyst loading: 102 µg/cm ² . ORR onset potential: 0.883 V vs. RHE (−0.02 V vs. Ag/AgCl). Current density: 4.3 mA/cm ² at 0.3 V vs. RHE (−0.60 V vs. Ag/AgCl) (at 1600 rpm; scan rate: 5 mV/s).
Graphene-based nitrogen-doped porous carbon sheets (GNPCs) (Zhong et al.—2014 [79])	Polyvinyl pyrrolidone (PVP); graphene oxide (GO) sheets; zinc nitrate salt (Zn(NO ₃) ₂ ·6H ₂ O); 2-methylimidazole.	PVP layering on GO sheets; chemically. ZIF-8 growth on PVP-layered GO to form ZIF-8/GO. High-temperature calcination of ZIF-8/GO (in the range of 650–950 °C).	Measured in O ₂ -saturated 0.1 M KOH. Catalyst loading: 200 µg/cm ² . ORR onset potential: 0.957 V vs. RHE. Current density: 6.0 mA/cm ² at 0.45 V vs. RHE (at 1600 rpm; scan rate: 5 mV/s).
Graphene oxide-sheathed ZIF-8 microcrystals (GZs) (Thomas et al.—2016 [80])	Graphene oxide (GO); zinc nitrate salt (Zn(NO ₃) ₂ ·6H ₂ O); 2-methylimidazole.	Ultrasonication of GO and zinc salt solution; then, introduce 2-methylimidazole to form GO/ZIF-8. Carbonization of GO/ZIF-8 at 950 °C in a nitrogen atmosphere.	Measured in O ₂ -saturated 0.1 M KOH. Catalyst loading: ~170 µg/cm ² . ORR onset potential: 0.88 V vs. RHE. Current density: ~4.5 mA/cm ² at 0.4 V vs. RHE (at 1600 rpm; scan rate: 5 mV/s).
N-doped porous carbon@graphene (N-PC@G) (Liu et al.—2016 [36])	Graphene oxide (GO); 2-methylimidazole; zinc nitrate salt (Zn(NO ₃) ₂ ·6H ₂ O).	Ultrasonic dispersion of GO solution; then, introduce 2-methylimidazole solution; finally, zinc salt is introduced to form ZIF-8@GO. Pyrolysis of ZIF-8@GO at 900 °C in a nitrogen atmosphere.	Measured in O ₂ -saturated 0.1 M KOH. Catalyst loading: ~407 µg/cm ² . ORR onset potential: 1.01 V vs. RHE. Current density: ~4.4 mA/cm ² at 0.6 V vs. RHE (at 1600 rpm; scan rate: 10 mV/s).
Metal organic framework-modified nitrogen-doped graphene (N-G/MOF) (Zhuang et al.—2016 [39,68,127,128])	Graphene oxide (GO); melamine; ZIF-8.	Nitrogen-doped graphene (N-G) synthesized from GO and melamine by a nanoscale high-energy wet ball milling process. By the same process, N-G and ZIF-8 were integrated to produce N-G/MOF.	Measured in O ₂ -saturated 0.1 M KOH. Catalyst loading: 37.3 µg/cm ² . ORR onset potential: ~0.73 V vs. RHE. Limiting current density: 5.02 mA/cm ² (at 1600 rpm; scan rate: 10 mV/s).
Core-shell hierarchically porous carbon nanopolyhedras (CS-HPCNs) (Cao et al.—2019 [37])	Zinc nitrate salt (Zn(NO ₃) ₂ ·6H ₂ O); 2-methylimidazole.	Chemical synthesis of ZIF-8 core crystal, chemically grown ZIF-8 shell over the core forming ZIF-8@ZIF-8; high-temperature treatment of core-shell ZIF-8@ZIF-8 (in the range of 900–1100 °C)—in nitrogen flow environment.	Measured in O ₂ -saturated 0.1 M KOH. Catalyst loading: 100 µg/cm ² . ORR onset potential: 0.709 V vs. RHE. Current density: ~3.75 mA/cm ² at −0.09 V vs. RHE (at 1600 rpm; scan rate: 10 mV/s).

Table 5. Cont.

Materials	Precursors	Synthesis Steps	ORR Catalytic Performance (of the Best Sample)
N-doped nanoporous carbon/graphene nanosheets (Zn-ZIF/GO and Co-Zn-ZIF/GO) (Wei et al.—2015 [38])	Graphene oxide (GO); zinc nitrate salt ($\text{Zn}(\text{NO}_3)_2 \cdot 6\text{H}_2\text{O}$); 2-methylimidazole; cobalt nitrate salt ($\text{Co}(\text{NO}_3)_2 \cdot 6\text{H}_2\text{O}$)	Chemical synthesis of ZIF-8 nanocrystal; then, add the GO solution to produce Zn-ZIF/GO; add cobalt nitrate salt to the Zn-ZIF/GO solution to produce Co-Zn-ZIF/GO.	<u>Zn-ZIF/GO and Co-Zn-ZIF/GO in alkaline electrolyte:</u> measured in O_2 -saturated 0.1 M KOH. Catalyst loading: 200 $\mu\text{g}/\text{cm}^2$. ORR onset potential: 0.92 V and 0.96 V vs. RHE. Current density: 5.2 mA/cm^2 and $\sim 4.5 \text{ mA}/\text{cm}^2$ at 0.6 V vs. RHE (at 1600 rpm; scan rate: 10 mV/s). <u>Co-Zn-ZIF/GO in acidic electrolyte:</u> measured in O_2 -saturated 0.1 M HClO_4 . Catalyst loading: 300 $\mu\text{g}/\text{cm}^2$. ORR onset potential: 0.85 V vs. RHE. Current density: 4.2 mA/cm^2 at 0.4 V vs. RHE (at 1600 rpm; scan rate: 10 mV/s).
Ketjenblack added zeolitic imidazolate framework-derived Fe/N/carbon (KJ-Fe/N/carbon) (Zhang et al.—2022 [81])	Zinc nitrate salt ($\text{Zn}(\text{NO}_3)_2 \cdot 6\text{H}_2\text{O}$); 2-methylimidazole; iron(III) chloride hexahydrate ($\text{FeCl}_3 \cdot 6\text{H}_2\text{O}$); Ketjenblack EC600J (KJ600).	KJ600-Fe-ZIF-8 production by solvent technique; pyrolysis of KJ600-Fe-ZIF-8 at 950 °C in an Ar/ NH_3 environment.	Measured in O_2 -saturated 0.1 M H_2SO_4 . Catalyst loading: 600 $\mu\text{g}/\text{cm}^2$. ORR: $E_{1/2}$ 0.834 V vs. RHE. (onset potential: ~ 0.98 V vs. RHE). Limiting current density: $\sim 4.6 \text{ mA}/\text{cm}^2$ at (at 900 rpm; scan rate: 10 mV/s).
MOF-derived yolk-shell Co-N-C combined with 3D macroporous graphene nanopockets (yolk-shell Co-N-C@GNP) (Liu et al.—2023 [82])	Zinc nitrate salt ($\text{Zn}(\text{NO}_3)_2 \cdot 6\text{H}_2\text{O}$); 2-methylimidazole; GO; cobalt nitrate salt ($\text{Co}(\text{NO}_3)_2 \cdot 6\text{H}_2\text{O}$).	Mix ZIF-8 (produced from zinc salt and 2-methylimidazole) and graphene nanopockets (prepared from GO); then, add cobalt salt solution. Calcination of the product at 950 °C in an Ar atmosphere.	Measured in O_2 -saturated 0.1 M KOH. Catalyst loading: 450 $\mu\text{g}/\text{cm}^2$. ORR onset potential: 1.01 V vs. RHE. ($E_{1/2}$ 0.86 V vs. RHE). Limiting current density: 5.8 mA/cm^2 (at 1600 rpm; scan rate: 5 mV/s).
Nitrogen and sulfur co-doped porous carbon (NSDPC) (Son et al.—2019 [134])	ZIF-8 and Thiourea ($\text{CH}_4\text{N}_2\text{S}$).	Chemical synthesis of ZIF-8. Solution of ZIF-8 and thiourea at different weight ratios. Dry out the solution. Carbonization of the ZIF-8/thiourea mixture at 900 °C for 5 h in an N_2 -saturated environment.	Measured in O_2 -saturated 0.1 M KOH. Catalyst loading: $\sim 530 \mu\text{g}/\text{cm}^2$ ($\sim 235 \mu\text{g}$ NSDPC, $\sim 295 \mu\text{g}$ Ketjen black). Limiting current density: $\sim 5.9 \text{ mA}/\text{cm}^2$ (at 1600 rpm; scan rate: 5 mV/s).
N, P, and S tri-doped mesoporous carbon (NPSPC) (Rong et al.—2019 [135])	ZIF-8; sodium phytate ($\text{C}_6\text{H}_6\text{Na}_{12}\text{O}_{24}\text{P}_6$); dodecyl mercaptan ($\text{C}_{12}\text{H}_{26}\text{S}$).	Chemical synthesis of ZIF-8. ZIF-8 and sodium phytate solution prepared in ethanol at room temperature. Add dodecyl mercaptan dropwise for 30 min and stir for 24 h. Then, wash with ethanol and dry out overnight in a vacuum environment at 50 °C. Carbonize at 900 °C for 4 h in an N_2 environment.	<u>In alkaline electrolyte:</u> measured in O_2 -saturated 0.1 M KOH. Catalyst loading: $\sim 1125 \mu\text{g}/\text{cm}^2$ (with Nafion). Onset potential: 0.923 V vs. RHE. Half-wave potential: 0.821 V vs. RHE. Limiting current density: 4.89 mA/cm^2 . <u>In acidic electrolyte:</u> measured in O_2 -saturated 0.5 M H_2SO_4 . Catalyst loading: $\sim 1289.1 \mu\text{g}/\text{cm}^2$ (with Nafion). Onset potential: 0.899 V vs. RHE. Half-wave potential: 0.757 V vs. RHE. Limiting current density: 5.20 mA/cm^2 .

The electrocatalytic data presented in the table demonstrate that, with the meticulous selection of precursors and the implementation of an optimized synthesis technique, there is a potential to develop a variant of such material that can surpass precious-metal-based catalysts in various electrocatalytic parameters. Of particular significance for electrochemical fuel cells are the improvements in the onset potential, limiting current density, as well as long-term performance stability and durability. These findings indicate that N-G/ZIF-8-based materials hold promise as efficient and sustainable alternatives to PGM-based catalysts for enhancing the performance of ORR in diverse electrocatalytic applications, especially in the context of electrochemical fuel cells.

The electrocatalytic performance of the N-G/ZIF-8-based/derived materials largely depends on the active surface area and porosity. These parameters directly dictate how many electrochemically active sites are available for the catalytic process and how conveniently the reactants and products can be transported through the materials. Following such concerns, the reported pore diameters, pore volumes, and BET surface areas of the above-discussed materials are precisely documented in Table 6.

Table 6. Compiled data of the porosity parameters of the N-G/ZIF-8-based/derived materials as electrocatalysts.

Material	Pore Diameter (nm)	Pore Volume (cm ³ /g)	BET Surface Area (m ² /g)
N-decorated nanoporous carbon (NC) (Aijaz et al. [77])	1 to 3	1.58	2747
Nitrogen-doped graphitic porous carbon (NGPC) (Zhang et al. [78])	1.2 to 1.6	0.99	932
Graphene-based nitrogen-doped porous carbon sheets (GNPCs) (Zhong et al. [79])	Not specified	Not specified	911
Graphene oxide sheathed ZIF-8 microcrystals (GZs) (Thomas et al. [80])	0.2 to 0.5	0.7	502
N-doped porous carbon@graphene (N-PC@G) (Liu et al. [36])	1.8, 10	0.907	1094.3
Metal organic framework-modified nitrogen-doped graphene (N-G/MOF) (Zhuang et al. [39,68,127,128])	1.6	0.404	1103
Core-shell hierarchically porous carbon nanopolyhedras (CS-HPCNs) (Cao et al. [37])	0.5, 1, and 10 to 17	1.374	991
N-doped nanoporous carbon/graphene nanosheets (Zn-ZIF/GO and Co-Zn-ZIF/GO) (Wei et al. [38])	Not specified	Not specified	1170
Ketjenblack-added zeolitic imidazolate framework-derived Fe/N/carbon (KJ-Fe/N/carbon) (Zhang et al. [81])	2, 100	Not specified	125, 405
MOFs-derived yolk-shell Co-N-C combined with 3D macroporous graphene nanopockets (yolk-shell Co-N-C@GNP) (Liu et al. [82])	Not specified	~0.66	178.20
Nitrogen and sulfur-co-doped porous carbon (NSDPC) (Son et al. [134])	~10	0.17	114
N, P, and S tri-doped mesoporous carbon (NPSPC) (Rong et al. [135])	~2.6	1.957	1641

To enhance the electrocatalytic performance, increasing the BET surface of the catalyst materials is a key concern. The N-G/ZIF-8-based/derived materials developed as electrocatalysts were found to have a higher BET surface area on average compared to the ones prepared for electrodes for batteries and capacitors (Tables 2 and 4, respectively). A higher

surface area allowed these catalyst materials to host a larger number of electrochemically active sites, which enhanced the reaction kinetics.

5. Conclusions

Recently, there has been a growing interest in developing carbon-based nanomaterials for energy applications by synthesizing N-G/MOF(ZIF-8)-based/derived materials, which offer combined material and chemical structural advantages. In this review, various N-G/ZIF-8-based/derived materials were meticulously studied. The main focus of this study was to investigate the materials' synthesis processes, physical and chemical structural characteristics, and critically assess their performance and functionalities on a fundamental level. To explore the potential electrochemical energy applications of these materials, the review was divided into three main sections based on their specific uses: electrode materials for different types of batteries, electrochemical capacitors, and electrocatalysts.

The N-G/ZIF-8-based/derived materials showed good potential as battery electrodes, with the advantage of mitigating volume expansion issues in lithium-ion batteries (LiBs) and potassium-ion batteries (PIBs), addressing the shuttle effect on Li-S batteries, and improving the reaction kinetics through pore size modulation. Notably, N-G/ZIF-8-based/derived materials exhibited impressive performances as electrodes for capacitors as well. In most of the studies, the synthesis process involved a carbonization process of the precursors in the range of 600–1000 °C. Reportedly, a porous graphitic structure with defects was introduced in the carbonization step. In terms of the porosity, the materials had a combination of microporous and mesoporous structures, which were beneficial for electrochemical activities; the surface areas of the materials were also extended. The synergetic effects arising from the combination of N-G and ZIF-8 were responsible for the enhanced performances. It can be noted that, for materials developed as battery electrodes, along with enhancing the electrochemical reaction rates, considerable attention was focused on improving their structural integrity. The essential data on the performances and structural parameters of the materials were carefully compiled in different tables.

Numerous N-G/ZIF-8-based/derived materials developed as electrocatalysts, especially for ORR, were also meticulously examined in this review. The synthesis processes of these electrocatalysts were similar to the ones for electrode materials. The materials demonstrated promising electrocatalytic performances when compared to conventional Pt/C catalysts. The improved performance and operational stability of these catalysts were attributed to their highly porous morphology, large surface area, ZIF-8-like structural form, contributions from the N-G sheets, abundant accessible active sites, diverse functionalities of doped nitrogen sites, and enhanced electrical conductivity provided by the graphene network. The role of different chemical functional groups in electrocatalytic activities was also carefully discussed. Comparative charts were created with the materials' performances and structural electrocatalysts.

Throughout the discussions, several key research gaps were identified, paving the way for future developments and advancements in N-G/ZIF-8-based/derived materials for energy applications. The comprehensive insights gained from this review highlight the vast potential of these materials in advancing electrocatalysts, battery electrodes, and electrochemical capacitor electrodes.

Author Contributions: N.T. prepared and wrote the manuscript; Y.W. assisted in editing the manuscript; B.B.N. reviewed and provided suggestions for editing the manuscript; and E.S.L. supervised this research activity, ensured the theoretical soundness of this study, constructed, edited, and reviewed the manuscript, and provided suggestions for editing. All authors have read and agreed to the published version of the manuscript.

Funding: This research was funded by the National Science Foundation (NSF), award number 1838369, and the New Jersey Institute of Technology (NJIT).

Acknowledgments: The authors acknowledge the research support from the Advanced Energy System and Microdevices (AESM) Laboratory at the New Jersey Institute of Technology (NJIT). This

research also received assistance from the Center for Functional Nanomaterials (CFN), which is a U.S. Department of Energy Office of Science User Facility, at Brookhaven National Laboratory under Contract No. DE-SC0012704.

Conflicts of Interest: The authors declare no conflicts of interest.

References

1. Friedman, J.S.; Girdhar, A.; Gelfand, R.M.; Memik, G.; Mohseni, H.; Taflove, A.; Wessels, B.W.; Leburton, J.-P.; Sahakian, A. V Cascaded Spintronic Logic with Low-Dimensional Carbon. *Nat. Commun.* **2017**, *8*, 15635. [[CrossRef](#)]
2. Senthil, T.; Divakaran, N.; Kale, M.B.; Mubarak, S.; Dhamodharan, D.; Wu, L.; Bensingh, R.J.; Kader, M.A.; Dutta, K. Chapter 2—Low-Dimensional Carbon-Based Nanomaterials for Energy Conversion and Storage Applications. In *Nanostructured, Functional, and Flexible Materials for Energy Conversion and Storage Systems*; Pandikumar, A., Rameshkumar, P., Eds.; Elsevier: Amsterdam, The Netherlands, 2020; pp. 15–68. ISBN 978-0-12-819552-9.
3. Castro, K.P.R.; Colombo, R.N.P.; Iost, R.M.; da Silva, B.G.R.; Crespilho, F.N. Low-Dimensionality Carbon-Based Biosensors: The New Era of Emerging Technologies in Bioanalytical Chemistry. *Anal. Bioanal. Chem.* **2023**, *415*, 3879–3895. [[CrossRef](#)] [[PubMed](#)]
4. Li, R.; Zhang, M.; Fu, X.; Gao, J.; Huang, C.; Li, Y. Research of Low-Dimensional Carbon-Based Magnetic Materials. *ACS Appl. Electron. Mater.* **2022**, *4*, 3263–3277. [[CrossRef](#)]
5. Das, C.M.; Kang, L.; Ouyang, Q.; Yong, K.-T. Advanced Low-Dimensional Carbon Materials for Flexible Devices. *InfoMat* **2020**, *2*, 698–714. [[CrossRef](#)]
6. Wang, Q.H.; Bellisario, D.O.; Drahushuk, L.W.; Jain, R.M.; Kruss, S.; Landry, M.P.; Mahajan, S.G.; Shimizu, S.F.E.; Ulissi, Z.W.; Strano, M.S. Low Dimensional Carbon Materials for Applications in Mass and Energy Transport. *Chem. Mater.* **2014**, *26*, 172–183. [[CrossRef](#)]
7. Zhang, S.; Liu, H.; Yu, J.; Li, B.; Ding, B. Multi-Functional Flexible 2D Carbon Nanostructured Networks. *Nat. Commun.* **2020**, *11*, 5134. [[CrossRef](#)]
8. Meunier, V.; Souza Filho, A.G.; Barros, E.B.; Dresselhaus, M.S. Physical Properties of Low-Dimensional sp^2 -Based Carbon Nanostructures. *Rev. Mod. Phys.* **2016**, *88*, 25005. [[CrossRef](#)]
9. Eaton, A.L.; Fielder, M.; Nair, A.K. Mechanical and Thermal Properties of Carbon-Based Low-Dimensional Materials. *MRS Bull.* **2022**, *47*, 1001–1010. [[CrossRef](#)]
10. Bouzid, A.-H.; Das, S.K. High Temperature Aged Leakage Relaxation Screening Tests on Confined Flexible Graphite Gaskets. In Proceedings of the ASME 2021 Pressure Vessels and Piping Conference, Virtual, 13–15 July 2021.
11. Ali, A.; Liang, F.; Zhu, J.; Shen, P.K. The Role of Graphene in Rechargeable Lithium Batteries: Synthesis, Functionalisation, and Perspectives. *Nano Mater. Sci.* **2022**; *in press*. [[CrossRef](#)]
12. Chen, X.; Tian, Y. Review of Graphene in Cathode Materials for Lithium-Ion Batteries. *Energy Fuels* **2021**, *35*, 3572–3580. [[CrossRef](#)]
13. Stoller, M.D.; Park, S.; Zhu, Y.; An, J.; Ruoff, R.S. Graphene-Based Ultracapacitors. *Nano Lett.* **2008**, *8*, 3498–3502. [[CrossRef](#)]
14. El-Kady, M.F.; Kaner, R.B. Scalable Fabrication of High-Power Graphene Micro-Supercapacitors for Flexible and on-Chip Energy Storage. *Nat. Commun.* **2013**, *4*, 1475. [[CrossRef](#)] [[PubMed](#)]
15. Velasco, A.; Ryu, Y.K.; Boscá, A.; Ladrón-de-Guevara, A.; Hunt, E.; Zuo, J.; Pedrós, J.; Calle, F.; Martínez, J. Recent Trends in Graphene Supercapacitors: From Large Area to Microsupercapacitors. *Sustain. Energy Fuels* **2021**, *5*, 1235–1254. [[CrossRef](#)]
16. Liu, C.; Yu, Z.; Neff, D.; Zhamu, A.; Jang, B.Z. Graphene-Based Supercapacitor with an Ultrahigh Energy Density. *Nano Lett.* **2010**, *10*, 4863–4868. [[CrossRef](#)] [[PubMed](#)]
17. Singh, H.; Zhuang, S.; Ingis, B.; Nunna, B.B.; Lee, E.S. Carbon-Based Catalysts for Oxygen Reduction Reaction: A Review on Degradation Mechanisms. *Carbon* **2019**, *151*, 160–174. [[CrossRef](#)]
18. Talukder, N.; Wang, Y.; Nunna, B.B.; Lee, E.S. Nitrogen-Doped Graphene Nanomaterials for Electrochemical Catalysis/Reactions: A Review on Chemical Structures and Stability. *Carbon* **2021**, *185*, 198–214. [[CrossRef](#)]
19. Deokar, G.; Jin, J.; Schwingenschlögl, U.; Costa, P.M.F.J. Chemical Vapor Deposition-Grown Nitrogen-Doped Graphene’s Synthesis, Characterization and Applications. *npj 2D Mater. Appl.* **2022**, *6*, 14. [[CrossRef](#)]
20. Shao, Y.; Zhang, S.; Engelhard, M.H.; Li, G.; Shao, G.; Wang, Y.; Liu, J.; Aksay, I.A.; Lin, Y. Nitrogen-Doped Graphene and Its Electrochemical Applications. *J. Mater. Chem.* **2010**, *20*, 7491–7496. [[CrossRef](#)]
21. Li, B.; Zhang, S.; Cui, C.; Qian, W.; Jin, Y. Comprehensive Review on Nitrogen-Doped Graphene: Structure Characterization, Growth Strategy, and Capacitive Energy Storage. *Energy Fuels* **2023**, *37*, 902–918. [[CrossRef](#)]
22. Xu, H.; Ma, L.; Jin, Z. Nitrogen-Doped Graphene: Synthesis, Characterizations and Energy Applications. *J. Energy Chem.* **2018**, *27*, 146–160. [[CrossRef](#)]
23. Ullah, S.; Shi, Q.; Zhou, J.; Yang, X.; Ta, H.Q.; Hasan, M.; Ahmad, N.M.; Fu, L.; Bachmatiuk, A.; Rummeli, M.H. Advances and Trends in Chemically Doped Graphene. *Adv. Mater. Interfaces* **2020**, *7*, 2000999. [[CrossRef](#)]
24. Zhuang, S.; Nunna, B.B.; Mandal, D.; Lee, E.S. A Review of Nitrogen-Doped Graphene Catalysts for Proton Exchange Membrane Fuel Cells—Synthesis, Characterization, and Improvement. *Nano-Struct. Nano-Objects* **2018**, *15*, 140–152. [[CrossRef](#)]
25. Jayaramulu, K.; Mukherjee, S.; Morales, D.M.; Dubal, D.P.; Nanjundan, A.K.; Schneemann, A.; Masa, J.; Kment, S.; Schuhmann, W.; Otyepka, M.; et al. Graphene-Based Metal–Organic Framework Hybrids for Applications in Catalysis, Environmental, and Energy Technologies. *Chem. Rev.* **2022**, *122*, 17241–17338. [[CrossRef](#)]

26. Qu, H.; Huang, L.; Han, Z.; Wang, Y.; Zhang, Z.; Wang, Y.; Chang, Q.; Wei, N.; Kipper, M.J.; Tang, J. A Review of Graphene-Oxide/Metal–Organic Framework Composites Materials: Characteristics, Preparation and Applications. *J. Porous Mater.* **2021**, *28*, 1837–1865. [[CrossRef](#)]
27. Wang, J.; Wang, Y.; Zhang, Y.; Uliana, A.; Zhu, J.; Liu, J.; der Bruggen, B. Zeolitic Imidazolate Framework/Graphene Oxide Hybrid Nanosheets Functionalized Thin Film Nanocomposite Membrane for Enhanced Antimicrobial Performance. *ACS Appl. Mater. Interfaces* **2016**, *8*, 25508–25519. [[CrossRef](#)]
28. Wang, K.; Hui, K.N.; San Hui, K.; Peng, S.; Xu, Y. Recent Progress in Metal–Organic Framework/Graphene-Derived Materials for Energy Storage and Conversion: Design, Preparation, and Application. *Chem. Sci.* **2021**, *12*, 5737–5766. [[CrossRef](#)] [[PubMed](#)]
29. Zhang, X.; Zhang, S.; Tang, Y.; Huang, X.; Pang, H. Recent Advances and Challenges of Metal–Organic Framework/Graphene-Based Composites. *Compos. B Eng.* **2022**, *230*, 109532. [[CrossRef](#)]
30. Zheng, Y.; Zheng, S.; Xue, H.; Pang, H. Metal-Organic Frameworks/Graphene-Based Materials: Preparations and Applications. *Adv. Funct. Mater.* **2018**, *28*, 1804950. [[CrossRef](#)]
31. Liu, Z.; Sun, D.; Wang, C.; You, B.; Li, B.; Han, J.; Jiang, S.; Zhang, C.; He, S. Zeolitic Imidazolate Framework-67 and Its Derivatives for Photocatalytic Applications. *Coord. Chem. Rev.* **2024**, *502*, 215612. [[CrossRef](#)]
32. Talukder, N.; Wang, Y.; Nunna, B.B.; Tong, X.; Lee, E.S. An Investigation on the Structural Stability of ZIF-8 in Water versus Water-Derived Oxidative Species in Aqueous Environment. *Microporous Mesoporous Mater.* **2024**, *366*, 112934. [[CrossRef](#)]
33. Karagiari, O.; Lalonde, M.B.; Bury, W.; Sarjeant, A.A.; Farha, O.K.; Hupp, J.T. Opening ZIF-8: A Catalytically Active Zeolitic Imidazolate Framework of Sodalite Topology with Unsubstituted Linkers. *J. Am. Chem. Soc.* **2012**, *134*, 18790–18796. [[CrossRef](#)]
34. Xue, W.; Zhou, Q.; Li, F.; Ondon, B.S. Zeolitic Imidazolate Framework-8 (ZIF-8) as Robust Catalyst for Oxygen Reduction Reaction in Microbial Fuel Cells. *J. Power Sources* **2019**, *423*, 9–17. [[CrossRef](#)]
35. Tian, K.; Wang, J.; Cao, L.; Yang, W.; Guo, W.; Liu, S.; Li, W.; Wang, F.; Li, X.; Xu, Z.; et al. Single-Site Pyrrolic-Nitrogen-Doped Sp²-Hybridized Carbon Materials and Their Pseudocapacitance. *Nat. Commun.* **2020**, *11*, 3884. [[CrossRef](#)] [[PubMed](#)]
36. Liu, S.; Zhang, H.; Zhao, Q.; Zhang, X.; Liu, R.; Ge, X.; Wang, G.; Zhao, H.; Cai, W. Metal-Organic Framework Derived Nitrogen-Doped Porous Carbon@graphene Sandwich-like Structured Composites as Bifunctional Electrocatalysts for Oxygen Reduction and Evolution Reactions. *Carbon* **2016**, *106*, 74–83. [[CrossRef](#)]
37. Cao, P.; Liu, Y.; Quan, X.; Zhao, J.; Chen, S.; Yu, H. Nitrogen-Doped Hierarchically Porous Carbon Nanopolyhedras Derived from Core-Shell ZIF-8@ZIF-8 Single Crystals for Enhanced Oxygen Reduction Reaction. *Catal. Today* **2019**, *327*, 366–373. [[CrossRef](#)]
38. Wei, J.; Hu, Y.; Liang, Y.; Kong, B.; Zhang, J.; Song, J.; Bao, Q.; Simon, G.P.; Jiang, S.P.; Wang, H. Nitrogen-Doped Nanoporous Carbon/Graphene Nano-Sandwiches: Synthesis and Application for Efficient Oxygen Reduction. *Adv. Funct. Mater.* **2015**, *25*, 5768–5777. [[CrossRef](#)]
39. Zhuang, S.; Nunna, B.B.; Lee, E.S. Metal Organic Framework-Modified Nitrogen-Doped Graphene Oxygen Reduction Reaction Catalyst Synthesized by Nanoscale High-Energy Wet Ball-Milling Structural and Electrochemical Characterization. *MRS Commun.* **2018**, *8*, 40–48. [[CrossRef](#)]
40. Deguenon, L.; Yamegueu, D.; Moussa kadri, S.; Gomna, A. Overcoming the Challenges of Integrating Variable Renewable Energy to the Grid: A Comprehensive Review of Electrochemical Battery Storage Systems. *J. Power Sources* **2023**, *580*, 233343. [[CrossRef](#)]
41. Ahn, H.; Kim, D.; Lee, M.; Nam, K.W. Challenges and Possibilities for Aqueous Battery Systems. *Commun. Mater.* **2023**, *4*, 37. [[CrossRef](#)]
42. Tanim, T.R.; Dufek, E.J.; Sazhin, S. V Challenges and Needs for System-Level Electrochemical Lithium-Ion Battery Management and Diagnostics. *MRS Bull.* **2021**, *46*, 420–428. [[CrossRef](#)]
43. He, J.; Manthiram, A. A Review on the Status and Challenges of Electrocatalysts in Lithium-Sulfur Batteries. *Energy Storage Mater.* **2019**, *20*, 55–70. [[CrossRef](#)]
44. Zhang, W.; Lu, J.; Guo, Z. Challenges and Future Perspectives on Sodium and Potassium Ion Batteries for Grid-Scale Energy Storage. *Mater. Today* **2021**, *50*, 400–417. [[CrossRef](#)]
45. Liu, S.; Kang, L.; Jun, S.C. Challenges and Strategies toward Cathode Materials for Rechargeable Potassium-Ion Batteries. *Adv. Mater.* **2021**, *33*, 2004689. [[CrossRef](#)]
46. Deshmukh, A.; Thripuranthaka, M.; Chaturvedi, V.; Das, A.K.; Shelke, V.; Shelke, M.V. A Review on Recent Advancements in Solid State Lithium–Sulfur Batteries: Fundamentals, Challenges, and Perspectives. *Prog. Energy* **2022**, *4*, 42001. [[CrossRef](#)]
47. Manthiram, A.; Fu, Y.; Su, Y.-S. Challenges and Prospects of Lithium–Sulfur Batteries. *Acc. Chem. Res.* **2013**, *46*, 1125–1134. [[CrossRef](#)]
48. Martín-Jimeno, F.J.; Suárez-García, F.; Paredes, J.I.; Enterría, M.; Pereira, M.F.R.; Martins, J.I.; Figueiredo, J.L.; Martínez-Alonso, A.; Tascón, J.M.D. A “Nanopore Lithography” Strategy for Synthesizing Hierarchically Micro/Mesoporous Carbons from ZIF-8/Graphene Oxide Hybrids for Electrochemical Energy Storage. *ACS Appl. Mater. Interfaces* **2017**, *9*, 44740–44755. [[CrossRef](#)] [[PubMed](#)]
49. Ding, B.; Fan, Z.; Lin, Q.; Wang, J.; Chang, Z.; Li, T.; Henzie, J.; Kim, J.; Dou, H.; Zhang, X.; et al. Confined Pyrolysis of ZIF-8 Polyhedrons Wrapped with Graphene Oxide Nanosheets to Prepare 3D Porous Carbon Heterostructures. *Small Methods* **2019**, *3*, 1900277. [[CrossRef](#)]
50. Wang, J.; Gao, L.; Zhao, J.; Zheng, J.; Wang, J.; Huang, J. A Facile In-situ Synthesis of ZIF-8 Nanoparticles Anchored on Reduced Graphene Oxide as a Sulfur Host for Li-S Batteries. *Mater. Res. Bull.* **2021**, *133*, 111061. [[CrossRef](#)]

51. Zhang, R.; Luo, Q.; Gong, J.; Chen, Z.; Wu, Z.; Li, S.; Zheng, Q.; Wu, X.; Lam, K.; Lin, D. Multilevel Spatial Confinement of Transition Metal Selenides Porous Microcubes for Efficient and Stable Potassium Storage. *J. Colloid Interface Sci.* **2023**, *644*, 10–18. [[CrossRef](#)] [[PubMed](#)]
52. Guo, X.; Zhu, C.; Xu, G.; Cheng, F. Synergetic-Modified Porous Co_2SiO_4 Conductive Network with ZIF-8 Derived Carbon and Reduced Graphene Oxide for High-Rate Lithium-Ion Battery Anode. *J. Electroanal. Chem.* **2023**, *941*, 117530. [[CrossRef](#)]
53. Winter, M.; Brodd, R.J. What Are Batteries, Fuel Cells, and Supercapacitors? *Chem. Rev.* **2004**, *104*, 4245–4270. [[CrossRef](#)]
54. Zhao, J.; Burke, A.F. Electrochemical Capacitors: Performance Metrics and Evaluation by Testing and Analysis. *Adv. Energy Mater.* **2021**, *11*, 2002192. [[CrossRef](#)]
55. He, X.; Zhang, X. A Comprehensive Review of Supercapacitors: Properties, Electrodes, Electrolytes and Thermal Management Systems Based on Phase Change Materials. *J. Energy Storage* **2022**, *56*, 106023. [[CrossRef](#)]
56. Wang, Y.; Song, Y.; Xia, Y. Electrochemical Capacitors: Mechanism, Materials, Systems, Characterization and Applications. *Chem. Soc. Rev.* **2016**, *45*, 5925–5950. [[CrossRef](#)] [[PubMed](#)]
57. Chaikittisilp, W.; Hu, M.; Wang, H.; Huang, H.-S.; Fujita, T.; Wu, K.C.-W.; Chen, L.-C.; Yamauchi, Y.; Ariga, K. Nanoporous Carbons through Direct Carbonization of a Zeolitic Imidazolate Framework for Supercapacitor Electrodes. *Chem. Commun.* **2012**, *48*, 7259–7261. [[CrossRef](#)] [[PubMed](#)]
58. Li, C.; Hu, C.; Zhao, Y.; Song, L.; Zhang, J.; Huang, R.; Qu, L. Decoration of Graphene Network with Metal–Organic Frameworks for Enhanced Electrochemical Capacitive Behavior. *Carbon* **2014**, *78*, 231–242. [[CrossRef](#)]
59. Wang, L.; Wang, C.; Wang, H.; Jiao, X.; Ouyang, Y.; Xia, X.; Lei, W.; Hao, Q. ZIF-8 Nanocrystals Derived N-Doped Carbon Decorated Graphene Sheets for Symmetric Supercapacitors. *Electrochim. Acta* **2018**, *289*, 494–502. [[CrossRef](#)]
60. Khakpour, F.; Ghafouri Taleghani, H.; Soleimani Lashkenari, M. Metal–Organic Framework/Sulfur-Doped Graphene Oxide Nanocomposite for High Efficiency Electrochemical Double-Layer Capacitors. *Appl. Organomet. Chem.* **2023**, *37*, e6969. [[CrossRef](#)]
61. Xiao, P.; Cao, L.; Wang, H.; Yan, G.; Chen, Q. Rational Design of Three-Dimensional Metal-Organic Framework-Derived Active Material/Graphene Aerogel Composite Electrodes for Alkaline Battery-Supercapacitor Hybrid Device. *Surf. Interfaces* **2022**, *33*, 102266. [[CrossRef](#)]
62. Cui, Y.; Zhao, C.; Zhao, L.; Zhang, X.; Wang, J. Preparation of Porous Layered Cobalt-Zinc Sulfide Nanostructures Based on Graphene Oxide Supported ZIF-8 Template for High-Performance Supercapacitors. *J. Solid. State Chem.* **2022**, *316*, 123581. [[CrossRef](#)]
63. Liu, S.; Wang, Q.; Li, B.; Zhou, Y.; Gong, T.; Li, J. Preparation of Nitrogen-Doped Hierarchical Porous Carbon Electrodes for High Performance Capacitive Deionization. *Ionics* **2023**, *29*, 2935–2945. [[CrossRef](#)]
64. Sun, Y.; Polani, S.; Luo, F.; Ott, S.; Strasser, P.; Dionigi, F. Advancements in Cathode Catalyst and Cathode Layer Design for Proton Exchange Membrane Fuel Cells. *Nat. Commun.* **2021**, *12*, 5984. [[CrossRef](#)]
65. Shao, Y.; Dodelet, J.-P.; Wu, G.; Zelenay, P. PGM-Free Cathode Catalysts for PEM Fuel Cells: A Mini-Review on Stability Challenges. *Adv. Mater.* **2019**, *31*, 1807615. [[CrossRef](#)]
66. Zhou, Y.; Guo, S. Recent Advances in Cathode Catalyst Architecture for Lithium–Oxygen Batteries. *eScience* **2023**, *3*, 100123. [[CrossRef](#)]
67. Li, M.; Zhang, L.; Xu, Q.; Niu, J.; Xia, Z. N-doped Graphene as Catalysts for Oxygen Reduction and Oxygen Evolution Reactions: Theoretical Considerations. *J. Catal.* **2014**, *314*, 66–72. [[CrossRef](#)]
68. Zhuang, S.; Lei, L.; Nunna, B.; Lee, E.S. New Nitrogen-Doped Graphene/MOF-Modified Catalyst for Fuel Cell Systems. *ECS Trans.* **2016**, *72*, 149. [[CrossRef](#)]
69. Wang, H.; Maiyalagan, T.; Wang, X. Review on Recent Progress in Nitrogen-Doped Graphene: Synthesis, Characterization, and Its Potential Applications. *ACS Catal.* **2012**, *2*, 781–794. [[CrossRef](#)]
70. Zhuang, S.; Nunna, B.B.; Lei, L.; Lee, E.S. Synthesis of Nitrogen-Doped Graphene Catalyst by Wet Ball Milling for Electrochemical Systems. In Proceedings of the 251st ACS National Meeting & Exposition, San Diego, CA, USA, 13–17 March 2016.
71. Lemes, G.; Sebastián, D.; Pastor, E.; Lázaro, M.J. N-doped Graphene Catalysts with High Nitrogen Concentration for the Oxygen Reduction Reaction. *J. Power Sources* **2019**, *438*, 227036. [[CrossRef](#)]
72. Xue, Y.; Chen, H.; Qu, J.; Dai, L. Nitrogen-Doped Graphene by Ball-Milling Graphite with Melamine for Energy Conversion and Storage. *2D Mater.* **2015**, *2*, 44001. [[CrossRef](#)]
73. Qu, L.; Liu, Y.; Baek, J.-B.; Dai, L. Nitrogen-Doped Graphene as Efficient Metal-Free Electrocatalyst for Oxygen Reduction in Fuel Cells. *ACS Nano* **2010**, *4*, 1321–1326. [[CrossRef](#)]
74. Parvez, K.; Yang, S.; Hernandez, Y.; Winter, A.; Turchanin, A.; Feng, X.; Müllen, K. Nitrogen-Doped Graphene and Its Iron-Based Composite as Efficient Electrocatalysts for Oxygen Reduction Reaction. *ACS Nano* **2012**, *6*, 9541–9550. [[CrossRef](#)] [[PubMed](#)]
75. Wu, J.; Ma, L.; Yadav, R.M.; Yang, Y.; Zhang, X.; Vajtai, R.; Lou, J.; Ajayan, P.M. Nitrogen-Doped Graphene with Pyridinic Dominance as a Highly Active and Stable Electrocatalyst for Oxygen Reduction. *ACS Appl. Mater. Interfaces* **2015**, *7*, 14763–14769. [[CrossRef](#)] [[PubMed](#)]
76. Ma, R.; Lin, G.; Zhou, Y.; Liu, Q.; Zhang, T.; Shan, G.; Yang, M.; Wang, J. A Review of Oxygen Reduction Mechanisms for Metal-Free Carbon-Based Electrocatalysts. *npj Comput. Mater.* **2019**, *5*, 78. [[CrossRef](#)]
77. Aijaz, A.; Fujiwara, N.; Xu, Q. From Metal–Organic Framework to Nitrogen-Decorated Nanoporous Carbons: High CO_2 Uptake and Efficient Catalytic Oxygen Reduction. *J. Am. Chem. Soc.* **2014**, *136*, 6790–6793. [[CrossRef](#)] [[PubMed](#)]

78. Zhang, L.; Su, Z.; Jiang, F.; Yang, L.; Qian, J.; Zhou, Y.; Li, W.; Hong, M. Highly Graphitized Nitrogen-Doped Porous Carbon Nanopolyhedra Derived from ZIF-8 Nanocrystals as Efficient Electrocatalysts for Oxygen Reduction Reactions. *Nanoscale* **2014**, *6*, 6590–6602. [[CrossRef](#)] [[PubMed](#)]
79. Zhong, H.; Wang, J.; Zhang, Y.; Xu, W.; Xing, W.; Xu, D.; Zhang, Y.; Zhang, X. ZIF-8 Derived Graphene-Based Nitrogen-Doped Porous Carbon Sheets as Highly Efficient and Durable Oxygen Reduction Electrocatalysts. *Angew. Chem. Int. Ed.* **2014**, *53*, 14235–14239. [[CrossRef](#)]
80. Thomas, M.; Illathvalappil, R.; Kurungot, S.; Nair, B.N.; Mohamed, A.A.P.; Anilkumar, G.M.; Yamaguchi, T.; Hareesh, U.S. Graphene Oxide Sheathed ZIF-8 Microcrystals: Engineered Precursors of Nitrogen-Doped Porous Carbon for Efficient Oxygen Reduction Reaction (ORR) Electrocatalysis. *ACS Appl. Mater. Interfaces* **2016**, *8*, 29373–29382. [[CrossRef](#)]
81. Zhang, P.-Y.; Yang, X.-H.; Jiang, Q.-R.; Cui, P.-X.; Zhou, Z.-Y.; Sun, S.-H.; Wang, Y.-C.; Sun, S.-G. General Carbon-Supporting Strategy to Boost the Oxygen Reduction Activity of Zeolitic-Imidazolate-Framework-Derived Fe/N/Carbon Catalysts in Proton Exchange Membrane Fuel Cells. *ACS Appl. Mater. Interfaces* **2022**, *14*, 30724–30734. [[CrossRef](#)]
82. Liu, Y.; Li, Z.; Wang, S.; Xuan, J.; Xiong, D.; Zhou, L.; Zhou, J.; Wang, J.; Yang, Y.; Du, Y. Hierarchical Porous Yolk-Shell Co-N-C Nanocatalysts Encaged Ingraphene Nanopockets for High-Performance Zn-Air Battery. *Nano Res.* **2023**, *16*, 8893–8901. [[CrossRef](#)]
83. Yu, G.; Xia, J.; Zhang, F.; Wang, Z. Hierarchical and Hybrid RGO/ZIF-8 Nanocomposite as Electrochemical Sensor for Ultrasensitive Determination of Dopamine. *J. Electroanal. Chem.* **2017**, *801*, 496–502. [[CrossRef](#)]
84. Yang, S.; Yang, M.; Yao, X.; Fa, H.; Wang, Y.; Hou, C. A Zeolitic Imidazolate Framework/Carbon Nanofiber Nanocomposite Based Electrochemical Sensor for Simultaneous Detection of Co-Existing Dihydroxybenzene Isomers. *Sens. Actuators B Chem.* **2020**, *320*, 128294. [[CrossRef](#)]
85. Li, K.; Kang, J.; Zhan, T.; Cao, W.; Liu, X.; Gao, H.; Si, C.; She, X. Electrochemical Sensing Platform for Naphthol Isomers Based on Situ Growth of ZIF-8 on Reduced Graphene Oxide by a Reaction-Diffusion Technique. *J. Colloid Interface Sci.* **2021**, *581*, 576–585. [[CrossRef](#)]
86. Rezvani Jalal, N.; Madrakian, T.; Afkhami, A.; Ahmadi, M. Ni/Co Bimetallic Metal–Organic Frameworks on Nitrogen-Doped Graphene Oxide Nanoribbons for Electrochemical Sensing of Doxorubicin. *ACS Appl. Nano Mater.* **2022**, *5*, 11045–11058. [[CrossRef](#)]
87. Wang, S.; Chen, F.; Li, Z.; Tao, H.; Qu, L.; Li, J.; Zhu, M.; Zha, Q. A Graphene Oxide/Zn-Metal Organic Framework Electrochemical Sensor for Acetaminophen Detection. *Surf. Interfaces* **2023**, *39*, 102910. [[CrossRef](#)]
88. Sun, S.; Wang, B.; Qing, M.; Tian, D.; Jiang, L.; Zhu, L. Electrochemical Dopamine Detection Using Electrochemically Reduced Graphene Oxide/Silver/Metal Organic Framework Composites. *ChemistrySelect* **2023**, *8*, e202204720. [[CrossRef](#)]
89. Liu, Q.; Xing, Y.; Pang, X.; Zhan, K.; Sun, Y.; Wang, N.; Hu, X. Electrochemical Immunosensor Based on MOF for Rapid Detection of 6-Benzyladenine in Bean Sprouts. *J. Food Compos. Anal.* **2023**, *115*, 105003. [[CrossRef](#)]
90. Xie, J.; Yang, H.; Wang, X.; Gao, F. ZIF-8/Electro-Reduced Graphene Oxide Nanocomposite for Highly Electrocatalytic Oxidation of Hydrazine in Industrial Wastewater. *Microchem. J.* **2021**, *168*, 106521. [[CrossRef](#)]
91. Mehmandoust, M.; Erk, E.E.; Soylak, M.; Erk, N.; Karimi, F. Metal–Organic Framework Based Electrochemical Immunosensor for Label-Free Detection of Glial Fibrillary Acidic Protein as a Biomarker. *Ind. Eng. Chem. Res.* **2023**, *62*, 4532–4539. [[CrossRef](#)]
92. Abdul Aziz, S.F.N.; Rahim, A.S.M.A.; Normi, Y.M.; Alang Ahmad, S.A.; Salleh, A.B. Rational Design of Mini Protein Mimicking Uricase: Encapsulation in ZIF-8 for Uric Acid Detection. *Proteins Struct. Funct. Bioinform.* **2023**, *91*, 967–979. [[CrossRef](#)]
93. Lei, H.; Zhang, Q.; Xiang, X.; Jiang, L.; Wang, S.; Duan, L.; Wang, S. Metal-Organic Framework Hybrid Materials of ZIF-8/RGO for Immobilization of D-Amino Acid Dehydrogenase. *Nano Res.* **2023**, *17*, 290–296. [[CrossRef](#)]
94. Kim, D.W.; Eum, K.; Kim, H.; Kim, D.; de Mello, M.D.; Park, K.; Tsapatsis, M. Continuous ZIF-8/Reduced Graphene Oxide Nanocoating for Ultrafast Oil/Water Separation. *Chem. Eng. J.* **2019**, *372*, 509–515. [[CrossRef](#)]
95. Shen, L.; Wang, X.; Zhang, Z.; Jin, X.; Jiang, M.; Zhang, J. Design and Fabrication of the Evolved Zeolitic Imidazolate Framework-Modified Polylactic Acid Nonwoven Fabric for Efficient Oil/Water Separation. *ACS Appl. Mater. Interfaces* **2021**, *13*, 14653–14661. [[CrossRef](#)] [[PubMed](#)]
96. Kamali, Z.; Khashehchi, M.; Zarafshan, P.; Pipelzadeh, E. Enhanced Desalination Performance of Capacitive Deionization Using ZIF-8/Graphene Nanocomposite Electrode. *Appl. Water Sci.* **2020**, *10*, 239. [[CrossRef](#)]
97. Ahmad, S.Z.N.; Salleh, W.N.W.; Yusop, M.Z.M.; Hamdan, R.; Aziz, F.; Awang, N.A.; Ismail, A.F. Synthesis of Zeolitic Imidazolate Framework-8 Modified Graphene Oxide Composite and Its Application for Lead Removal. *J. Chem. Technol. Biotechnol.* **2023**, *98*, 2668–2676. [[CrossRef](#)]
98. Kim, D.; Kim, D.W.; Hong, W.G.; Coskun, A. Graphene/ZIF-8 Composites with Tunable Hierarchical Porosity and Electrical Conductivity. *J. Mater. Chem. A* **2016**, *4*, 7710–7717. [[CrossRef](#)]
99. Nordin, N.A.H.M.; Ismail, A.F.; Misdan, N.; Nazri, N.A.M. Modified ZIF-8 Mixed Matrix Membrane for CO₂/CH₄ Separation. *AIP Conf. Proc.* **2017**, *1891*, 020091. [[CrossRef](#)]
100. Li, W.; Zhang, Y.; Su, P.; Xu, Z.; Zhang, G.; Shen, C.; Meng, Q. Metal–Organic Framework Channelled Graphene Composite Membranes for H₂/CO₂ Separation. *J. Mater. Chem. A* **2016**, *4*, 18747–18752. [[CrossRef](#)]
101. Jiang, M.; Li, H.; Zhou, L.; Xing, R.; Zhang, J. Hierarchically Porous Graphene/ZIF-8 Hybrid Aerogel: Preparation, CO₂ Uptake Capacity, and Mechanical Property. *ACS Appl. Mater. Interfaces* **2018**, *10*, 827–834. [[CrossRef](#)]
102. Wu, X.; Zhang, H.; Yin, Z.; Yang, Y.; Wang, Z. ZIF-8/GO Sandwich Composite Membranes through a Precursor Conversion Strategy for H₂/CO₂ Separation. *J. Memb. Sci.* **2022**, *647*, 120291. [[CrossRef](#)]

103. Arifin, N.F.T.; Yusof, N.; Nordin, N.A.H.M.; Jaafar, J.; Ismail, A.F.; Salleh, W.N.W.; Aziz, F. An Improved Hybrid Nanocomposites of Rice Husk Derived Graphene (GRHA)/Zeolitic Imidazolate Framework-8 for Hydrogen Adsorption. *Int. J. Hydrogen Energy* **2021**, *46*, 24864–24876. [[CrossRef](#)]
104. Lv, C.; Kang, W.; Liu, S.; Yang, P.; Nishina, Y.; Ge, S.; Bianco, A.; Ma, B. Growth of ZIF-8 Nanoparticles In Situ on Graphene Oxide Nanosheets: A Multifunctional Nanoplatform for Combined Ion-Interference and Photothermal Therapy. *ACS Nano* **2022**, *16*, 11428–11443. [[CrossRef](#)] [[PubMed](#)]
105. Sanaei-Rad, S.; Ghasemzadeh, M.A.; Razavian, S.M.H. Synthesis of a Novel Ternary ZIF-8/GO/MgFe₂O₄ Nanocomposite and Its Application in Drug Delivery. *Sci. Rep.* **2021**, *11*, 18734. [[CrossRef](#)] [[PubMed](#)]
106. Deng, W.; Liu, W.; Zhu, H.; Chen, L.; Liao, H.; Chen, H. Click-Chemistry and Ionic Cross-Linking Induced Double Cross-Linking Ionogel Electrolyte for Flexible Lithium-Ion Batteries. *J. Energy Storage* **2023**, *72*, 108509. [[CrossRef](#)]
107. Zheng, F.; Yang, Y.; Chen, Q. High Lithium Anodic Performance of Highly Nitrogen-Doped Porous Carbon Prepared from a Metal-Organic Framework. *Nat. Commun.* **2014**, *5*, 5261. [[CrossRef](#)] [[PubMed](#)]
108. Tai, Z.; Shi, M.; Chong, S.; Chen, Y.; Shu, C.; Dai, X.; Tan, Q.; Liu, Y. N-Doped ZIF-8-Derived Carbon (NC-ZIF) as an Anodic Material for Lithium-Ion Batteries. *J. Alloys Compd.* **2019**, *800*, 1–7. [[CrossRef](#)]
109. Chen, Y.-M.; Liang, W.; Li, S.; Zou, F.; Bhaway, S.M.; Qiang, Z.; Gao, M.; Vogt, B.D.; Zhu, Y. A Nitrogen Doped Carbonized Metal-Organic Framework for High Stability Room Temperature Sodium-Sulfur Batteries. *J. Mater. Chem. A* **2016**, *4*, 12471–12478. [[CrossRef](#)]
110. Liu, X.; Zhang, S.; Xing, Y.; Wang, S.; Yang, P.; Li, H. MOF-Derived, N-Doped Porous Carbon Coated Graphene Sheets as High-Performance Anodes for Lithium-Ion Batteries. *New J. Chem.* **2016**, *40*, 9679–9683. [[CrossRef](#)]
111. Deng, W.-N.; Li, Y.-H.; Xu, D.-F.; Zhou, W.; Xiang, K.-X.; Chen, H. Three-Dimensional Hierarchically Porous Nitrogen-Doped Carbon from Water Hyacinth as Selenium Host for High-Performance Lithium-Selenium Batteries. *Rare Met.* **2022**, *41*, 3432–3445. [[CrossRef](#)]
112. Shiraiishi, S. Chapter 27—Electric Double Layer Capacitors. In *Carbon Alloys*; Yasuda, E., Inagaki, M., Kaneko, K., Endo, M., Oya, A., Tanabe, Y., Eds.; Elsevier Science: Oxford, UK, 2003; pp. 447–457. ISBN 978-0-08-044163-4.
113. Tao, Y.; Kanoh, H.; Groen, J.C.; Kaneko, K. Characterization of Alkaline Post-Treated ZSM-5 Zeolites by Low Temperature Nitrogen Adsorption. In *Characterization of Porous Solids VII*; Llewellyn, P.L., Rodriguez-Reinoso, F., Rouquerol, J., Seaton, N., Eds.; Studies in Surface Science and Catalysis; Elsevier: Amsterdam, The Netherlands, 2007; Volume 160, pp. 279–286.
114. Vallyon, J.; Ötvös, Z.; Onyestyák, G.; Rees, L.V.C. The Sorption Dynamics of Propane, i-Butane and Neopentane in Carbon Nanotubes. In *Characterization of Porous Solids VII*; Llewellyn, P.L., Rodriguez-Reinoso, F., Rouquerol, J., Seaton, N., Eds.; Studies in Surface Science and Catalysis; Elsevier: Amsterdam, The Netherlands, 2007; Volume 160, pp. 439–446.
115. Devi, M.; Rawat, S.; Sharma, S. A Comprehensive Review of the Pyrolysis Process: From Carbon Nanomaterial Synthesis to Waste Treatment. *Oxf. Open Mater. Sci.* **2021**, *1*, itab014. [[CrossRef](#)]
116. Velmurugan, V. Review of Research and Development on Pyrolysis Process. *Mater. Today Proc.* **2022**, *49*, 3679–3686. [[CrossRef](#)]
117. Jiang, H.; Shao, J.; Zhu, Y.; Yu, J.; Cheng, W.; Yang, H.; Zhang, X.; Chen, H. Production Mechanism of High-Quality Carbon Black from High-Temperature Pyrolysis of Waste Tire. *J. Hazard. Mater.* **2023**, *443*, 130350. [[CrossRef](#)]
118. Jäckel, N.; Simon, P.; Gogotsi, Y.; Presser, V. Increase in Capacitance by Subnanometer Pores in Carbon. *ACS Energy Lett.* **2016**, *1*, 1262–1265. [[CrossRef](#)]
119. Sylla, N.F.; Ndiaye, N.M.; Ngom, B.D.; Momodu, D.; Madito, M.J.; Mutuma, B.K.; Manyala, N. Effect of Porosity Enhancing Agents on the Electrochemical Performance of High-Energy Ultracapacitor Electrodes Derived from Peanut Shell Waste. *Sci. Rep.* **2019**, *9*, 13673. [[CrossRef](#)]
120. Liu, T.; Zhang, F.; Song, Y.; Li, Y. Revitalizing Carbon Supercapacitor Electrodes with Hierarchical Porous Structures. *J. Mater. Chem. A* **2017**, *5*, 17705–17733. [[CrossRef](#)]
121. Park, K.S.; Ni, Z.; Côté, A.P.; Choi, J.Y.; Huang, R.; Uribe-Romo, F.J.; Chae, H.K.; O’Keeffe, M.; Yaghi, O.M. Exceptional Chemical and Thermal Stability of Zeolitic Imidazolate Frameworks. *Proc. Natl. Acad. Sci. USA* **2006**, *103*, 10186–10191. [[CrossRef](#)] [[PubMed](#)]
122. Xiao, F.; Yang, S.; Zhang, Z.; Liu, H.; Xiao, J.; Wan, L.; Luo, J.; Wang, S.; Liu, Y. Scalable Synthesis of Freestanding Sandwich-Structured Graphene/Polyaniline/Graphene Nanocomposite Paper for Flexible All-Solid-State Supercapacitor. *Sci. Rep.* **2015**, *5*, 9359. [[CrossRef](#)] [[PubMed](#)]
123. Li, Y.; Zhang, Y.; Zhang, H.; Xing, T.; Chen, G. A Facile Approach to Prepare a Flexible Sandwich-Structured Supercapacitor with RGO-Coated Cotton Fabric as Electrodes. *RSC Adv.* **2019**, *9*, 4180–4189. [[CrossRef](#)] [[PubMed](#)]
124. Li, D.; Gong, Y.; Wang, M.; Pan, C. Preparation of Sandwich-like NiCo₂O₄/RGO/NiO Heterostructure on Nickel Foam for High-Performance Supercapacitor Electrodes. *Nanomicro Lett.* **2016**, *9*, 16. [[CrossRef](#)] [[PubMed](#)]
125. Guo, Z.; Zhang, Y.; Zhou, J.; Sun, D.; Li, H. Facile Self-Assembly of Sandwich-like MXene Layered Multiscale Structure Nanocomposite. *2D Mater.* **2022**, *10*, 15014. [[CrossRef](#)]
126. Li, Z.; Chen, G.; Deng, J.; Li, D.; Yan, T.; An, Z.; Shi, L.; Zhang, D. Creating Sandwich-like Ti₃C₂/TiO₂/RGO as Anode Materials with High Energy and Power Density for Li-Ion Hybrid Capacitors. *ACS Sustain. Chem. Eng.* **2019**, *7*, 15394–15403. [[CrossRef](#)]
127. Zhuang, S.; Singh, H.; Nunna, B.B.; Mandal, D.; Boscoboinik, J.A.; Lee, E.S. Nitrogen-Doped Graphene-Based Catalyst with Metal-Reduced Organic Framework: Chemical Analysis and Structure Control. *Carbon* **2018**, *139*, 933–944. [[CrossRef](#)]

128. Singh, H.; Zhuang, S.; Nunna, B.B.; Lee, E.S. Thermal Stability and Potential Cycling Durability of Nitrogen-Doped Graphene Modified by Metal-Organic Framework for Oxygen Reduction Reactions. *Catalysts* **2018**, *8*, 607. [[CrossRef](#)]
129. Zhuang, S.; Lee, E.S.; Lei, L.; Nunna, B.B.; Kuang, L.; Zhang, W. Synthesis of Nitrogen-Doped Graphene Catalyst by High-Energy Wet Ball Milling for Electrochemical Systems. *Int. J. Energy Res.* **2016**, *40*, 2136–2149. [[CrossRef](#)]
130. Korusenko, P.M.; Bolotov, V.V.; Nesov, S.N.; Povoroznyuk, S.N.; Khailov, I.P. Changes of the Electronic Structure of the Atoms of Nitrogen in Nitrogen-Doped Multiwalled Carbon Nanotubes under the Influence of Pulsed Ion Radiation. *Nucl. Instrum. Methods Phys. Res. B* **2015**, *358*, 131–135. [[CrossRef](#)]
131. Lherbier, A.; Blase, X.; Niquet, Y.-M.; Triozon, F.; Roche, S. Charge Transport in Chemically Doped 2D Graphene. *Phys. Rev. Lett.* **2008**, *101*, 36808. [[CrossRef](#)]
132. Usachov, D.; Vilkov, O.; Gruneis, A.; Haberer, D.; Fedorov, A.; Adamchuk, V.K.; Preobrajenski, A.B.; Dudin, P.; Barinov, A.; Oehzelt, M.; et al. Nitrogen-Doped Graphene: Efficient Growth, Structure, and Electronic Properties. *Nano Lett.* **2011**, *11*, 5401–5407. [[CrossRef](#)]
133. Talukder, N.; Wang, Y.; Nunna, B.B.; Tong, X.; Boscoboinik, J.A.; Lee, E.S. Investigation on Electrocatalytic Performance and Material Degradation of an N-Doped Graphene-MOF Nanocatalyst in Emulated Electrochemical Environments. *Ind. Chem. Mater.* **2023**, *1*, 360–375. [[CrossRef](#)]
134. Son, S.; Lim, D.; Nam, D.; Kim, J.; Shim, S.E.; Baeck, S.-H. N, S-Doped Nanocarbon Derived from ZIF-8 as a Highly Efficient and Durable Electro-Catalyst for Oxygen Reduction Reaction. *J. Solid. State Chem.* **2019**, *274*, 237–242. [[CrossRef](#)]
135. Rong, H.; Zhan, T.; Sun, Y.; Wen, Y.; Liu, X.; Teng, H. ZIF-8 Derived Nitrogen, Phosphorus and Sulfur Tri-Doped Mesoporous Carbon for Boosting Electrocatalysis to Oxygen Reduction in Universal PH Range. *Electrochim. Acta* **2019**, *318*, 783–793. [[CrossRef](#)]
136. Shirzadi Jahromi, H.; Saxena, S.; Sridhar, S.; Ghantasala, M.K.; Guda, R.; Rozhkova, E.; Suthar, K. Synthesis and Characterization of Nitrogen Doped Reduced Graphene Oxide Based Cobalt-ZIF-8 Catalysts for Oxygen Reduction Reaction. *ECS Trans.* **2021**, *104*, 59. [[CrossRef](#)]
137. Xue, S.; Yu, Y.; Wei, S.; Xu, B.; Lei, J.; Ban, R.; Wu, Q.; Zheng, M.; Li, J.; Kang, J. Nitrogen-Doped Porous Carbon Derived from ZIF-8 as a Support of Electrocatalyst for Enhanced Oxygen Reduction Reaction in Acidic Solution. *J. Taiwan Inst. Chem. Eng.* **2018**, *91*, 539–547. [[CrossRef](#)]
138. Sui, X.-L.; Zhang, L.-M.; Zhao, L.; Gu, D.-M.; Huang, G.-S.; Wang, Z.-B. Nitrogen-Doped Graphene Aerogel with an Open Structure Assisted by in-Situ Hydrothermal Restructuring of ZIF-8 as Excellent Pt Catalyst Support for Methanol Electro-Oxidation. *Int. J. Hydrogen Energy* **2018**, *43*, 21899–21907. [[CrossRef](#)]
139. Xu, X.; Dong, X.; Li, D.; Qi, M.; Huang, H. ZIF-8-Derived Three-Dimensional Nitrogen-Doped Porous Carbon as a Pt Catalyst Support for Electrocatalytic Oxidation of Glucose in a Glucose Fuel Cell. *ACS Appl. Energy Mater.* **2023**, *6*, 2886–2896. [[CrossRef](#)]

Disclaimer/Publisher’s Note: The statements, opinions and data contained in all publications are solely those of the individual author(s) and contributor(s) and not of MDPI and/or the editor(s). MDPI and/or the editor(s) disclaim responsibility for any injury to people or property resulting from any ideas, methods, instructions or products referred to in the content.